AN ABSTRACT OF THE THESIS OF

Paul D. Armatis for the degree of Master of Science in Mechanical Engineering presented on November 28, 2017

Title: Numerical and Experimental Evaluation of Membrane Based Energy Recovery Ventilator Performance with an Internal Support Structure

Abstract Approved:

Brian M. Fronk

Large amounts of energy are wasted when conditioned air in buildings is exhausted to meet ventilation requirements. There are several technologies to recover some of this energy, including the recent development of membrane based energy recovery ventilators (ERVs). ERVs exchange sensible heat and moisture between incoming fresh and outgoing exhaust air, reducing the amount of energy required to maintain the building environment at the set condition. Membrane based ERV market penetration has been limited by high manufacturing costs and relatively low volumetric efficiency. In this thesis, the potential to decrease the cost and improve performance of membrane based ERVs using minichannel flow paths enabled by additive manufacturing techniques will be explored.

First, one-dimensional and two-dimensional resistance network models of the heat and mass transfer and pressure drop in a "quasi-counterflow" membrane ERV are developed. Verification of the heat transfer model is completed by comparing results to the counterflow NTU-ε correlations. The models are then compared to results from the literature for a similar architecture. The models are used to parametrically evaluate the performance of membrane based ERVs with pin-fin and strip-fin internal minichannel type support structures fabricated using additive manufacturing techniques. At the same time, experiments are conducted to iteratively evaluate the capability limits of the manufacturing method with respect to repeatability, resolution, and fabrication time. Based on the thermal hydraulic models and the fabrication experiments, a test scale exchanger was designed and fabricated with additive manufacturing techniques that demonstrate the potential to achieve

specified performance and size requirements while being commercially viable. The insights from this study can be used to guide the fabrication of full scale commercial membrane based ERVs.

Numerical and Experimental Evaluation of Membrane Based Energy Recovery Ventilator Performance with an Internal Support Structure

by

Paul D. Armatis

A THESIS

submitted to

Oregon State University

in partial fulfillment of

the requirements for the

degree of

Master of Science

Presented November 28, 2017

Commencement June 2018

Master of Science thesis of Paul D. Armatis presented on November 28, 2017

APPROVED:

Major Professor, representing Mechanical Engineering

Head of the School of Mechanical, Industrial, and Manufacturing Engineering

Dean of the Graduate School

I understand that my thesis will become part of the permanent collection of Oregon State University libraries. My signature below authorizes release of my thesis to any reader upon request.

Paul D. Armatis, Author

ACKNOWLEDGEMENTS

I want to thank my advisor Dr. Brian Fronk for his guidance and patience which allowed me to learn how to conduct meaningful research. I will carry these lessons moving forward. His close attention and encouragement is greatly appreciated. I also want to thank the members of the research lab present during my time working on this project including Ahmad Bukshaisha, Connor Dokken, Matthew Hyder, Tabeel Jacob, Saad Jajja, Michael Polander, Michael VanderPutten, and Kyle Zada. Having a group of fellow students willing to lend an ear, provide encouragement, and be a friend was invaluable. I am very thankful for the support of a family and church always making time for me. Finally, I cannot show enough appreciation to my wife and her understanding during difficult times working on research. I hope in the years to come I show her the same grace she has shown me.

TABLE OF CONTENTS

Page

TABLE OF CONTENTS (Continued)

Page

TABLE OF CONTENTS (Continued)

TABLE OF CONTENTS (Continued)

LIST OF FIGURES

LIST OF FIGURES (Continued)

LIST OF FIGURES (Continued)

LIST OF TABLES

LIST OF TABLES (Continued)

NOMENCLATURE

A	m^2	area
AR	-	aspect ratio
C	$mol\ m^{-3}$	concentration
c_p	$J\ kg^{-1}K^{-1}$	specific heat
d	m	pin diameter
D	$m^2\ s^{-1}$	diffusivity
D_H	m	hydraulic diameter
f	-	friction factor
F	-	cross flow correction factor
h	$W\ m^{-2}\ K^{-1}$	heat transfer coefficient
h_{ch}	m	channel height
H	m	height
i	$J\ kg^{-}1$	specific enthalpy
j	-	Colburn j factor
k	$W\ m^{-1}\ K^{-1}$	thermal conductivity
K	$m\ s^{-1}$	combined mass transfer coefficient
l	m	segment length
L_p	m	pin length
m	kg	mass
MW	$kg\ mol^{-1}$	molecular weight
n	-	number of moles
N	-	quantity
Nu	-	Nusselt number
P	Pa	pressure
$\mathscr{P}$	m	perimeter
Pr	-	Prandtl number
Q	J	heat transferred
R	$K\ W^{-1}$, $s\ m^{-1}$	resistance
$\bar{R}$	$J\ mol^{-1}\ K^{-1}$	universal gas constant

Re	-	Reynolds number
S_p	m	streamwise center-to-center pin spacing
St	-	Stanton number
T	K	Temperature
T_p	m	transverse center-to-center pin spacing
U	W m^{-2} K^{-1}	combined heat transfer coefficient
V	m s^{-1}	velocity
W	m	width

Greek Symbols

α	m^2 s^{-1}	thermal diffusivity
β	m s^{-1}	convective mass transfer coefficient
Δ	-	difference, change
δ	m	membrane thickness
ε	%	effectiveness
θ	kg kg^{-1}	water uptake
ρ	kg m^{-3}	density
φ	%	relative humidity
ψ	-	coefficient of mass diffusive resistance (CMDR)
ω	kg kg^{-1}	humidity ratio

Subscripts

a	dry air
c	cross section
ch	channel
d	duct
e	exhaust air stream
fg	vaporization
H	high
HT	heat transfer

i	inlet
l	latent
L	low
LM	log-mean
m	membrane
MT	mass transfer
o	outlet
p	pin
s	sensible, supply, surface
st	strip-fin
sat	saturation
t	transverse direction
v	water vapor
w	wall, membrane surface

Chapter 1: Introduction

1.1 Background

Heating, ventilation, and air conditioning (HVAC) accounted for 44% of the consumed energy in U.S. commercial buildings in 2012, a total of approximately 3,080 trillion British Thermal Units (BTU) (EIA, 2016). HVAC technology is continually improving, however, required minimum ventilation needed to maintain safe and comfortable occupied spaces (ASHRAE, 2016) sets an upper limit on energy saved by conventional HVAC equipment upgrades. Ventilation requires the mechanical conditioning of outdoor make-up air and the exhausting of conditioned room air, making ventilation a high energy consumption process. Efforts to recover some of the energy from the exhaust stream have been commercially developed in heat recovery ventilation (HRV) or energy recovery ventilation (ERV) devices over the past several decades (ASHRAE, 2008; Mardiana-Idayu & Riffat, 2012). Devices capable of transferring both sensible and latent energy through heat and moisture transfer are of particular interest. Examples include pumped desiccant systems, rotary "enthalpy" desiccant wheels, and more recently, membrane-based exchangers (Kistler & Cussler, 2002; Woods, 2014; Yang, Yuan, Gao, & Guo, 2015).

1.1.1 Membrane-Based Energy Recovery Ventilators

Generally, membrane-based ERVs are fabricated by stacking parallel membrane layers as shown in Figure 1.2a. Indoor exhaust and outdoor supply air are split between alternating channels. As the air flows through the channels, heat and moisture is exchanged between the streams. In the cooling season, hot, humid outdoor air is cooled and dehumidified by the cool, dry indoor air. A schematic of this is shown in Figure 1.1. In the heating season, the outdoor air is heated and humidified by the indoor air. The bulk flow of air is typically in either a cross or counter-flow orientation (Figure 1.2b).

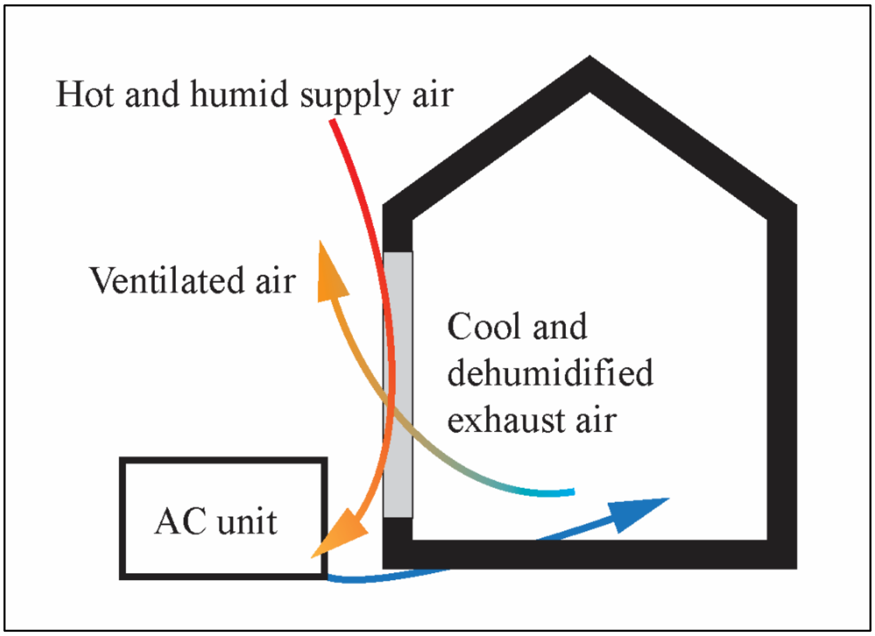

Figure 1.1: Cooling season flow schematic

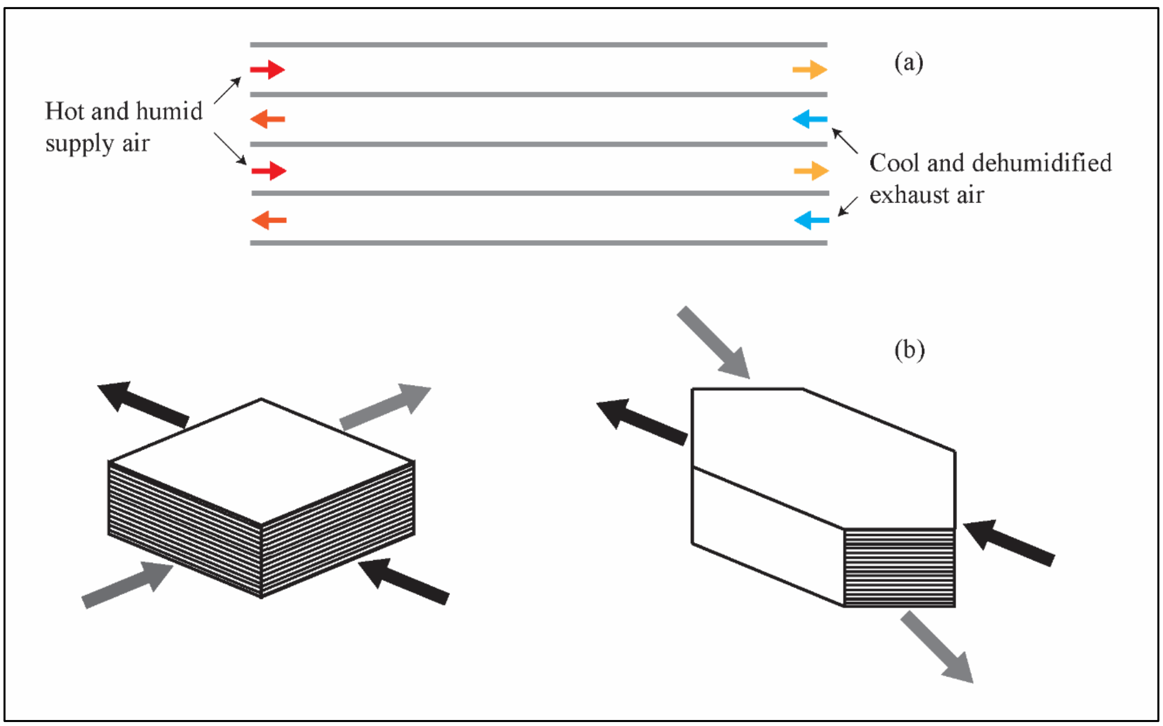

Figure 1.2: (a) Stacked membrane-based ERV diagram and (b) cross (left) and quasi-counterflow (right) schematics

Reducing equipment cost and size remain a key challenge for continued commercialization and adoption of these devices. Minimizing the heat and mass transfer resistances in the device enables processing of a fixed amount of air with a smaller and more affordable ERV. A schematic of the heat and mass transfer resistances in membrane based ERVs is shown in Figure 1.3, which includes convective resistances in the air streams and conduction/diffusion resistances in the membrane.

Water vapor permeability and selectivity in commercially available membranes has increased due to membrane material, design, and manufacturing improvements. This reduces the mass transfer resistance, $R_{m,MT}$, and prevents the transfer of undesirable species from the exhaust air to the incoming fresh air (Huizing, Mérida, & Ko, 2014). With these improvements, convective mass transfer resistance in the supply and exhaust air stream can become the limiting resistance. Experimental and analytical investigations indicate the air-side mass transfer resistance can range from 10% to upwards of 75% of the total mass transport resistance (Huizing *et al.*, 2014; Min & Su, 2010b; Woods, 2014). Methods to increase convective heat transfer include corrugated channels (Li Zhi Zhang, 2005), spacers (Koester, Klasen, Lölsberg, & Wessling, 2016; Woods & Kozubal, 2013), and reducing hydraulic diameter of the air channels (Min & Su, 2010a). These methods typically increase convective heat and mass transfer at the cost of increased pressure drop (Woods & Kozubal, 2013). The practical maximum allowable pressure drop in a building ERV is approximately 300 Pa (Woods & Kozubal, 2013). Thus, models must be developed to accurately assess the trade-offs between enhanced heat and mass transfer and pressure drop to optimize membrane ERV design.

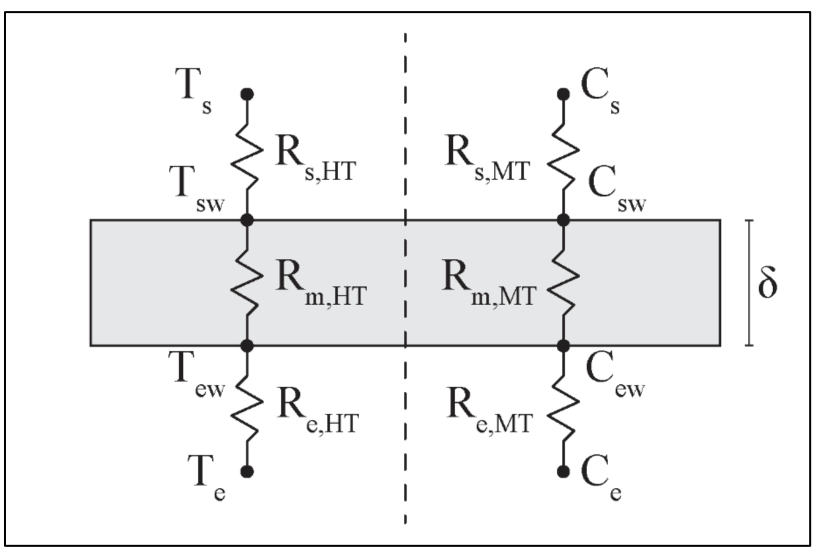

Figure 1.3: Heat and mass transfer resistance schematic

1.1.2 Membrane Considerations

Membrane ERVs operate at steady state and axial conduction in both the air and the membrane are generally assumed negligible for modeling purposes (Niu & Zhang, 2001; Yang *et al.*, 2015; Y. Zhang, Jiang, Zhang, Deng, & Jin, 2000). These assumptions make the air-side heat transfer and sensible effectiveness relatively simple to characterize with duct flow laminar convection correlations (Shah & London, 1978b). Conductive heat transfer through the membrane can then be determined with knowledge of the thermal conductivity and thickness of the material.

The latent energy to be recovered through water vapor transfer accounts for a considerable portion of the overall energy available (L. Z. Zhang, Zhu, Deng, & Hua, 2005; L. Z. Zhang, 2006). Thus, accurate modeling of the mass transfer is critical.

Convective mass transfer resistance can be evaluated using established analogies with convective heat transfer such as the Chilton-Colburn analogy (Chilton & Colburn, 1934). However, the mass transfer resistance through the membrane generally does not parallel the simplicity of the heat transfer resistance of the membrane. Some models include the assumption of a constant diffusion coefficient of the membrane (L. Z. Zhang & Jiang, 1999; Li Zhi Zhang, 2010). In many models, the mass transfer resistance is a function of the membrane surface humidity, temperature, or both (Al-Waked, Nasif, Morrison, & Behnia, 2015; M. S. Nasif, Al-Waked, Behnia, & Morrison, 2012; Niu & Zhang, 2001) while some models also incorporate pressure and membrane pore dimensions (Yang *et al.*, 2015). These models are diverse and complex since the membranes are typically composites made of a wide range of materials. Generally, there is a sorption layer and a supporting substrate (Huizing *et al.*, 2014). Membrane characteristics important for ERVs are discussed in greater detail in Chapter 2 of this thesis.

One way to decrease the mass transfer resistance of the membrane is to reduce the thickness of the membrane (Metz, Van De Ven, Potreck, Mulder, & Wessling, 2005). However, this can cause problems with structural integrity of the ERV device. Adding a secondary support structure for fabrication and rigidity can further complicate modeling since convective heat transfer correlations of certain complex geometries may not exist. However, this does provide an opportunity to increase boundary layer disruption and mixing within the ERV which can enhance convective transport, although at the cost of higher pressure drop.

1.2 Scope of Current Research

Increased adoption of membrane-based ERVs using current membrane technology requires an economical manufacturing process providing the required structural support for the membrane. The goal of this study is to evaluate the feasibility of using new manufacturing techniques and a thinner, more efficient membrane to enable highly effective energy recovery ventilation from a heat and mass transfer perspective. To address this goal, a two dimensional coupled heat and mass transfer resistance network model and a fluid flow model are developed to conduct parametric studies on an ERV fabricated using advanced manufacturing techniques. The model is compared with existing data, used to size an ERV, and evaluates tradeoffs of different support structure patterns enabled by an advanced manufacturing technique.

1.3 Thesis Organization

The organization of the thesis is as follows:

- Chapter 2 reviews the literature regarding previous modeling and experimental work done with ERVs as well as membrane characterization.
- Chapter 3 describes the methodology behind the developed model.
- Chapter 4 discusses how the model is used for sizing under certain constraints such as the manufacturing method
- Chapter 5 present and discusses the results of the parametric studies conducted with the developed model. A comparison of the model with experimental data and uncertainties of both the model and experimental setup are discussed as well.
- Chapter 6 provides final conclusions and recommended future work.

Chapter 2: Literature Review

Recent work on modeling membrane based ERV devices have focused on investigation of different flow configurations, membrane types and internal architectures, with comprehensive reviews provided by Woods (2014) and Yang *et al.* (2015). In an earlier work, L. Z. Zhang and Jiang (1999) developed a finite difference model of cross flow ERVs using paper core and porous hydrophilic membranes with bare rectangular channels. They concluded that high sensible and latent effectiveness were possible (> 80%), and a counterflow orientation would be preferable to cross flow. Zhang *et al*. then conducted experiments (L. Z. Zhang & Niu, 2002; Li Zhi Zhang, Liang, & Pei, 2008) and developed correlations for performance (L. Z. Zhang & Niu, 2002) of different paper and porous membranes in a cross flow orientation. They found that the membrane diffusive resistance dominated compared to the air-side convective resistance for the range of conditions investigated. Min & Su (2010a, 2010b, 2011) formulated a mathematical model of crossflow membrane based ERV with bare rectangular channels and reported the effects of membrane properties, inlet conditions and membrane spacing and thickness. Lee *et al.* (2012) modeled a crossflow paper membrane ERV using an ε-NTU approach for the heat and mass transfer over the entire membrane core. This approach required the assumption of a constant UA throughout the core. Their model predicted experimental data within 4% for sensible heat transfer and 10% for latent heat transfer. Typical assumptions in these prior models include (1) 1D process (2) uniform flow (3) negligible mass change in separate flow streams and (4) negligible heat and mass transfer along flow direction (Yang *et al.*, 2015).

More recently, Zhang (2010) conducted computational fluid dynamics (CFD) simulations of a “quasi-counter” flow exchanger (schematic shown in Figure 1.2) consisting of multiple bare rectangular channels. The quasi-counterflow orientation is identical to the overall form factor considered in the present study. The quasi-counter flow architecture has the advantage of improved heat and mass transfer in the counterflow body region, and easier routing of air streams in the approximately crossflow header region. In his study, Li Zhi Zhang (2010) used the finite volume method to solve the coupled momentum, energy and mass transport partial differential equations using FLUENT with the coupled mass transfer solved by the heat and mass transfer analogy. He found improved sensible and latent effectiveness between the cross flow and quasi-counterflow designs of about 5%.

2.1 Membrane Modeling

In a more recent study by Al-Waked *et al.* (2015), the authors recognize some previous work (M. Nasif, Al-Waked, Morrison, & Behnia, 2010; M. S. Nasif et al., 2012; Yaïci, Ghorab, & Entchev, 2013; Li Zhi Zhang, 2010) in which a constant membrane mass transfer resistance is assumed in the modeling effort. They also mention the effort made by (Niu & Zhang, 2001) to represent the variation in the membrane mass transfer resistance with a dimensionless coefficient of moisture diffusive resistance (CMDR). This coefficient incorporates a material dependent sorption curve as a function of relative humidity at the membrane surface shown as Eq. (2.1)

$$\theta = \frac{w_{\max}}{1 - C + C / \phi} \tag{2.1}$$

The values of w_{max} and C are dependent on the membrane sorption properties from experimental data. The water uptake, θ, can then be used to find the mass flux of water vapor through the membrane in Eq.(2.2).

$$m_v'' = \rho_m D_m \frac{\theta_{sw} - \theta_{ew}}{\delta} \tag{2.2}$$

The mass flux can also be represented by definition of mass transfer resistance as in Eq.(2.3).

$$m_v'' = \rho_a \frac{\omega_{sw} - \omega_{ew}}{R_{m,MT}} \tag{2.3}$$

In setting these mass flux equations equal and solving for $R_{m,MT}$ Eq.(2.4) is obtained.

$$R_{m,MT} = \frac{\rho_a}{\rho_m} \frac{\delta}{D_m} \frac{\omega_{sw} - \omega_{ew}}{\theta_{sw} - \theta_{ew}} \tag{2.4}$$

Now $R_{m,MT}$ can be expressed as a function of relative humidity φ and temperature T if two substitutions are made. First, using the Clapeyron equation to write the humidity ratio ω in terms of φ and T by assuming a standard atmospheric pressure of 101,325 Pa provides Eq.(2.5)

$$\frac{\phi}{\omega}=\frac{e^{5294/T}}{10^{6}}-1.61\phi \tag{2.5}$$

Niu and Zhang (2001) assume for simplicity the right term can be neglected since it will generally have an effect smaller than 5%. Solving for ω, the equation substituted into Eq.(2.4) is

$$\omega=\frac{10^{6}\phi}{e^{5294/T}} \tag{2.6}$$

Second, the relationship between the water uptake and the humidity ratio is defined such that

$$\theta_{sw}-\theta_{ew}=\left(\frac{\partial\theta}{\partial\phi}\right)_{s}\left(\phi_{sw}-\phi_{ew}\right) \tag{2.7}$$

Where

$$\left(\frac{\partial\theta}{\partial\phi}\right)_{s}=\frac{w_{\max}C}{\left(1-C+C/\phi_{sw}\right)^{2}\phi_{sw}} \tag{2.8}$$

After substituting and simplifying, we obtain the desired expression for local membrane mass transfer resistance as a function of relative humidity and temperature.

$$R_{m,MT}=\frac{\rho_{a}}{\rho_{m}}\frac{\delta}{D_{m}}\psi \tag{2.9}$$

Where

$$\psi=\frac{10^{6}\left(1-C+\left(C/\phi_{sw}\right)\right)^{2}\phi_{sw}^{2}}{e^{\left(5294/T_{sw}\right)}w_{\max}C} \tag{2.10}$$

The coefficient ψ is referred to as the coefficient of mass diffusive resistance (CMDR). The CMDR accounts for the local humidity and temperature and the effect these local properties have on the membrane mass transfer.

2.2 Summary and Need for Further Research

Much modeling and experimental effort has been made to predict the performance of ERVs in the literature. Research has been done to capture the complex and variable nature of the membrane mass transfer in an effort to better predict the latent effectiveness. Typical modeling of internal support structures are computationally expensive and do not incorporate more complex flow configurations such as the quasi-counter flow configuration Zhang (2010) which are very practical from an economic perspective. Other economic factors including the manufacturing process and installation considerations are frequently unassociated with ERV design and performance.

In this work, an ERV with an internal support structure will be sized using a computationally inexpensive resistance network modeling technique. This will be done while taking the fabrication and installation challenges associated with incorporating a new highly permeable membrane into consideration.

Chapter 3: Model Development

3.1 Approach

The objective of the present study is to evaluate the performance and tradeoffs in the design of a new, low aspect ratio (width/height) quasi counter-flow ERV (Figure 3.1) architecture. The ERV performance requirements are high latent (> 83%) and sensible (> 90%) effectiveness at AHRI rating conditions shown in Table 3.1 (AHRI, 2013) for an air flow rate of 510 $m^3\ hr^{-1}$ (300 $ft^3\ min^{-1}$) with pressure drop less than 300 Pa.

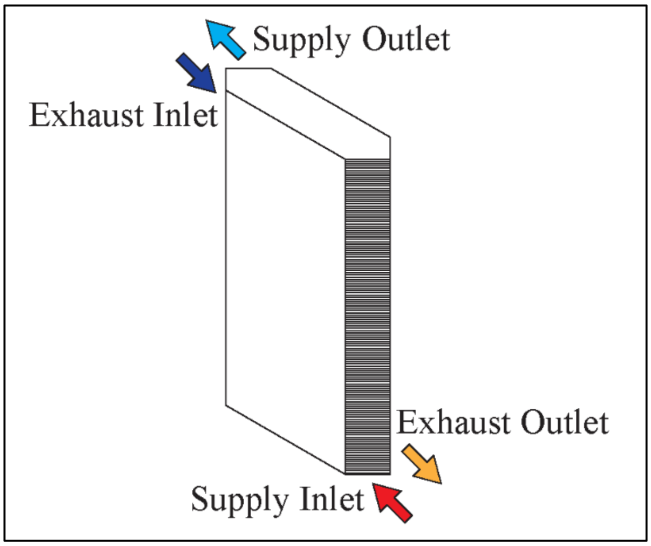

Figure 3.1: Low aspect ratio quasi-counter flow ERV schematic

The low aspect ratio yields a form factor that can be more easily integrated into the actual building envelope for new construction or retrofit purposes. The initial target for this concept is commercial buildings in North America, which typically have wall assembly thicknesses on the order of 8 to 10 inches. Rather than using bare parallel channels (Figure 3.2) as has been extensively investigated, the present study considers parallel mini/micro channels containing either an array of strip fins (Figure 3.3) or micropin fins (Figure 3.4).

Table 3.1: AHRI ERV rating conditions

Air Stream		Heating	Cooling
Supply	Dry-bulb, °F	35	95
	Wet-bulb, °F	33	78
Exhaust	Dry-bulb, °F	70	75
	Wet-bulb, °F	58	63

For the purpose of this study, the features are considered non-conducting structural supports that are integrated into the membrane through advanced manufacturing techniques, discussed in Chapter 4.

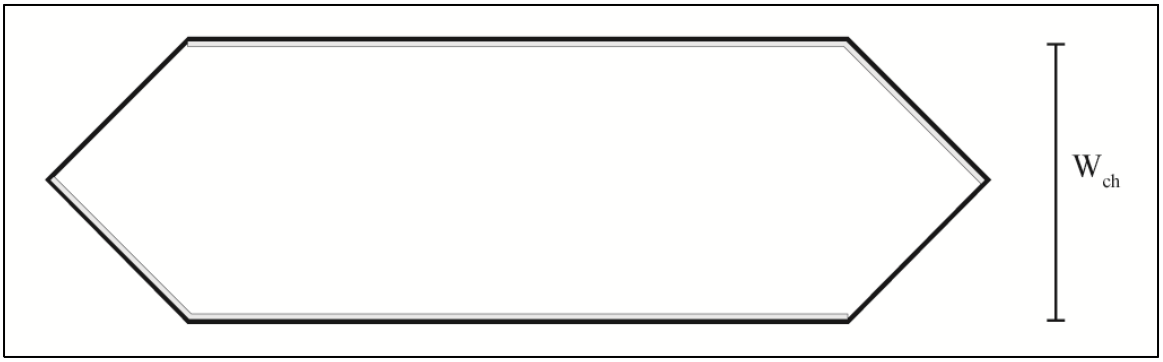

Figure 3.2: Bare channel ERV membrane layer

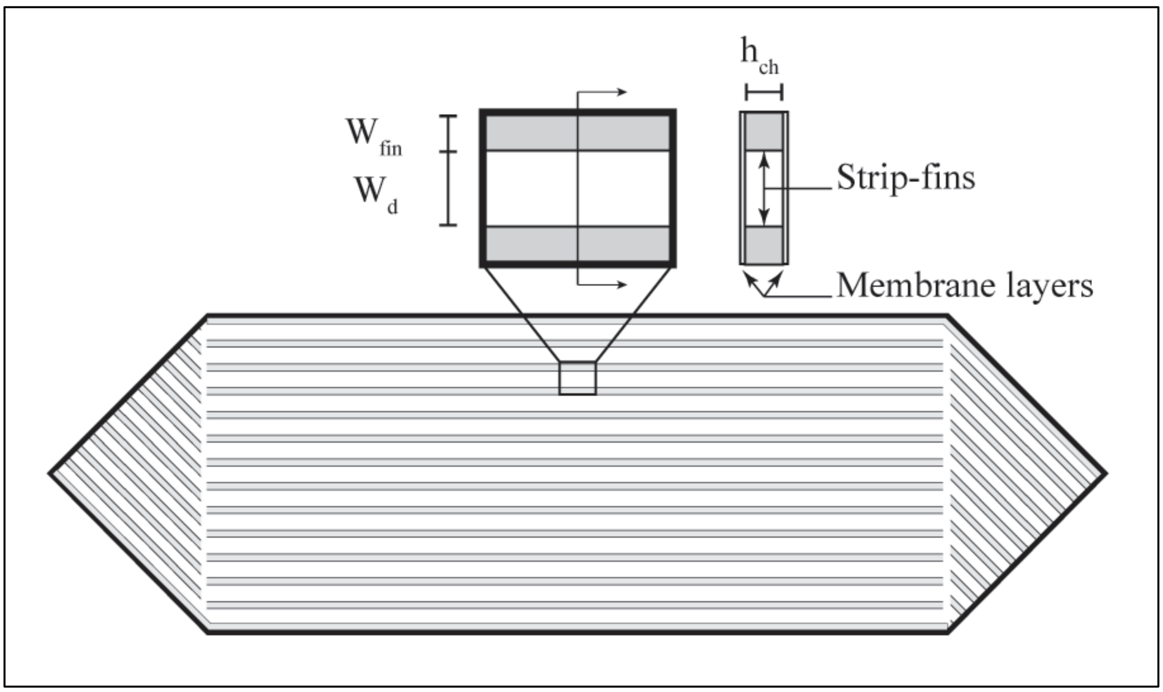

Figure 3.3: Strip-fin internal geometry

To design and evaluate the ERV, a heat and mass transfer resistance network model is developed (Figure 3.5). The resistance model enables rapid parametric investigation and optimization of ERV performance at low computational cost. In this chapter, a one-dimensional (1D) model is introduced first, followed by the development of a two-dimensional (2D) model capable of accounting for spatially varying membrane mass transfer resistance. Both approaches are evaluated by comparing the predictive capability with the experimentally validated computational fluid dynamics (CFD) results from Zhang

(2010) for counter, quasi-counter, and parallel flow ERV geometries and results from Al-Waked, Nasif, Morrison, & Behnia (2015) for the cross flow configuration with variable membrane properties.

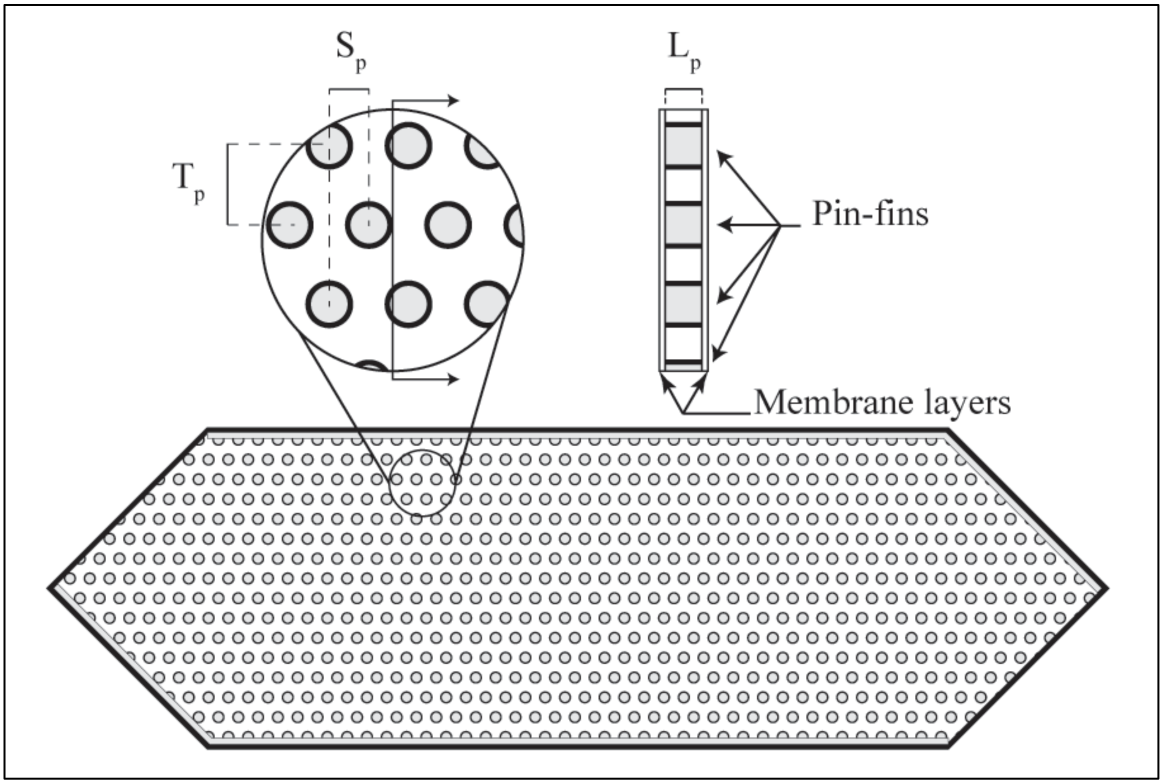

Figure 3.4: Pin-fin internal geometries

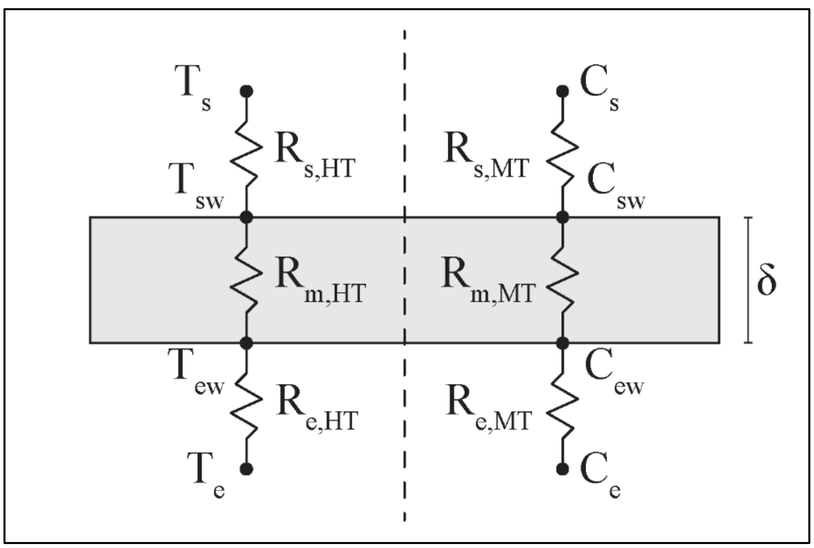

Figure 3.5: Heat and mass transfer resistance network models in an ERV

3.1.1 One-Dimensional Model

First, a 1D segmented heat and mass transfer resistance model was developed to predict the heat and mass transfer across a single membrane layer (schematics of segmented approach shown in Figure 3.6 and Figure 3.7). Each segment was modeled as an individual heat and mass exchanger in series. In each segment, expressions were formulated to calculate the local heat transfer, mass transfer and pressure drop and then solved iteratively using the Engineering Equation Solver (Klein, 2015) platform. Different predictive correlations and models were used for bare parallel plates, micro pin-fin, and rectangular strip fins, as discussed below. The overall heat and mass transfer were then calculated through a log-mean difference approach. Then, the outlet properties of each segment were used as the inlet properties for the subsequent segment. Finally, assuming symmetry for each set of parallel channels, the single channel pair model was extrapolated to calculate the performance for a multi-channel membrane based ERV. Figure 3.6 demonstrates the performance modeling of a strip-fin ERV using a single duct within a microchannel while in Figure 3.7, the entire channel is modeled for bare channel and pin-fin ERVs.

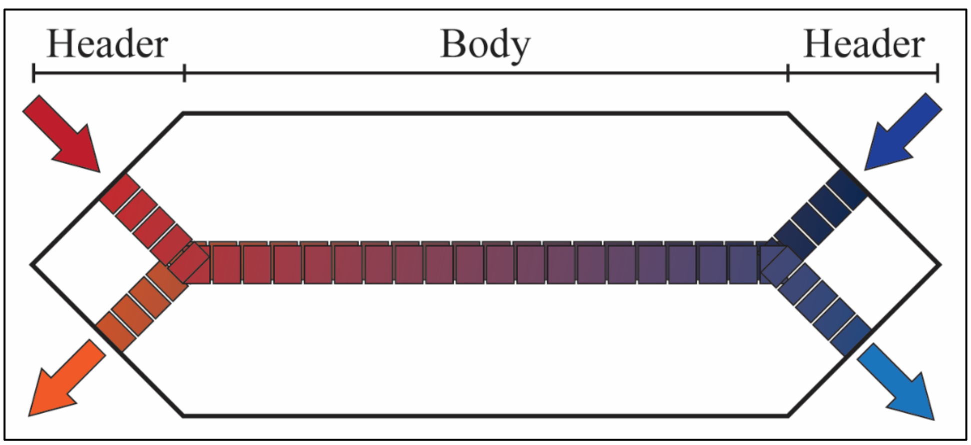

Figure 3.6: 1D segmented model in strip-fin ERV

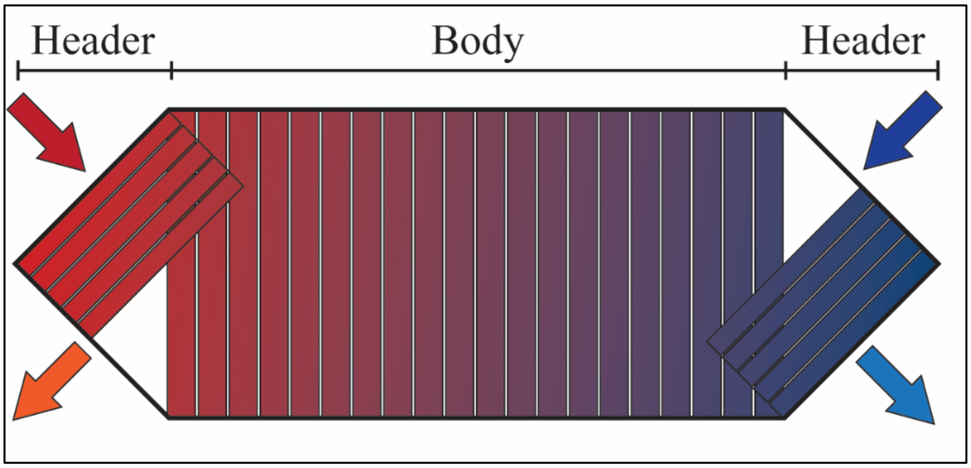

Figure 3.7: 1D segmented model in bare channel and pin-fin ERVs

3.1.1.1 Heat Transfer Model

In the body of the ERV (see Figure 3.6 for reference), each segment was modeled as a pure counter-flow heat exchanger (FHT = 1) using the log-mean temperature difference method shown in Eq.(3.1). The heat transfer in the inlet and outlet headers was found by approximating the headers as segmented cross-flow heat exchangers, where the correction factor FHT was calculated using relationships from (Nellis & Klein, 2009) for each segment in the header region.

$$\dot{Q} = F_{HT} \cdot U \cdot A \cdot \Delta T_{LM} \tag{3.1}$$

Here, the *UA* was defined as the inverse of the outdoor air convective ($R_{s,HT}$), membrane conductive ($R_{m,HT}$), and indoor air convective ($R_{e,HT}$), thermal resistances in series. The outlet temperatures used in the log-mean temperature difference calculation are determined iteratively. For the bare parallel plates, the variable *A* is the entire membrane area, while for the micropin and rectangular strip fin architecture, the variable *A* is defined as the open membrane area in a segment (Eq.(3.2)). As the strip fins are made of poorly conducting material, their contribution to heat transfer area is neglected. To facilitate evaluation with available correlations, the pin-fins are assumed to conduct heat only. The factor of two in Eq.(3.3) accounts for the top and bottom layers of the channel segment.

$$UA = \left(\frac{1}{h_s A} + \frac{\delta}{k_m A} + \frac{1}{h_e A} \right)^{-1} \tag{3.2}$$

$$A = 2l \cdot W_{ch} \qquad \text{bare channels}$$
$$A = 2\left(l \cdot W_{ch} - N_p \cdot (\pi/4) \cdot d^2\right) \qquad \text{micropin channels} \tag{3.3}$$
$$A = 2l \cdot W_d \qquad \text{strip fin channels}$$

The convective heat transfer coefficients for the indoor and outdoor air in the bare parallel channels were calculated using a correlation for developing laminar flow, assuming constant temperature boundary for high aspect ratio rectangular ducts (Eq. 3.159 in Kakaç, Shah, & Aung (1987)). The correlation is pre-defined in the *Engineering Equation Solver* (Klein, 2015) software as a function of Reynolds number, Prandtl number, axial position with the exchanger and the channel aspect ratio. The Nusselt number for the strip fins were calculated using tabulated solutions from Shah & London (1978) (pg. 204, Table 43) for laminar flow in rectangular ducts with a constant temperature boundary at the top and bottom and adiabatic sidewalls.

The hydraulic diameter for the bare parallel channels was calculated via Eq.(3.4) while the hydraulic diameter for the strip fin architecture was calculated via Eq.(3.5). Detailed dimensions of the strip fin architecture are shown in Figure 3.3.

$$D_{\mathrm{H,bare}} = \frac{4A_c}{\mathcal{P}} = \frac{4W_{ch}h_{ch}}{2\left(W_{ch} + h_{ch}\right)} \tag{3.4}$$

$$D_{\mathrm{H,strip}} = \frac{4A_c}{\mathcal{P}} = \frac{4W_d h_{ch}}{2\left(W_d + h_{ch}\right)} \tag{3.5}$$

For the micropin array, the convective heat transfer coefficient was determined using a correlation for Colburn *j* factor developed by Short, Raad, & Price (2002) for laminar flow through staggered pin arrays (Eq.(3.6)).

$$j = 0.760\left(S_p / d\right)^{0.16}\left(T_p / d\right)^{0.20}\left(L_p / d\right)^{(-0.11)}\mathrm{Re}_{\mathrm{d}}^{(-0.67)} \quad \text{for } \mathrm{Re}_{\mathrm{d}} < 10^3 \tag{3.6}$$

Here, S_p is the streamwise center-to-center pin spacing, d is the pin diameter, T_p is the transverse center-to-center pin spacing, and L_p is the pin height, as shown in Figure 3.4. The pin Reynolds number ($\mathrm{Re_d}$) is defined using the pin diameter as the characteristic length and the max velocity, defined as:

$$V_{\mathrm{max}} = \dot{V} / A_{\mathrm{min}} \tag{3.7}$$

Where

$$A_{\min} = W_{ch} \cdot L_p - N_t \cdot d \cdot L_p \tag{3.8}$$

The *j*-factor is related to the Stanton number by:

$$j = \mathrm{St} \cdot \mathrm{Pr}^{2/3} \tag{3.9}$$

The Stanton number was then be used to find the Nusselt number and the convective heat transfer coefficient with the following equation:

$$\mathrm{St} = \frac{\mathrm{Nu}}{\mathrm{Re}\,\mathrm{Pr}} = \frac{h}{\rho \cdot V_{\max} \cdot c_p} \tag{3.10}$$

For the micropin fins, both the Nusselt number and Reynolds number were defined using the hydraulic diameter (Eq.(3.11)) as the characteristic length in Eq.(3.10). A_{tot} (Eq.(3.12)) is defined as the total wetted surface area inside a channel, and is different from the heat and mass transfer area, *A*, defined in Eq.(3.3).

$$D_{\mathrm{H,pin}} = 4A_{\min} \cdot l \,/\, A_{\mathrm{tot}} \tag{3.11}$$

$$A_{\mathrm{tot}} = 2\left(l \cdot W_{ch}\right) + N_p \cdot \pi\left(d \cdot L_p - d^2 / 2\right) \tag{3.12}$$

3.1.1.2 Mass Transfer Model

The mass transfer resistances considered in each segment were shown previously in Figure 1.3. As it is with heat transfer, an overall mass transfer coefficient was obtained considering both convective resistances and the effective diffusivity (D_m) of the membrane:

$$KA = \left(\frac{1}{\beta_s A} + \frac{\delta}{D_m A} + \frac{1}{\beta_e A} \right)^{-1} \tag{3.13}$$

The rate of mass transfer through the membrane was calculated as:

$$\begin{aligned} \dot{n}_{\mathrm{v}} &= F_{\mathrm{MT}} \cdot K \cdot A \cdot \Delta C_{\mathrm{LM}} \\ \dot{m}_{\mathrm{v}} &= \dot{n}_{\mathrm{v}} \cdot MW_{\mathrm{H_2O}} \end{aligned} \tag{3.14}$$

Where,

$$\Delta C_{\mathrm{LM}} = \frac{\left(C_{si} - C_{eo}\right) - \left(C_{so} - C_{ei}\right)}{\ln\left(\dfrac{C_{si} - C_{eo}}{C_{so} - C_{ei}}\right)} \tag{3.15}$$

The molar concentrations used in the log-mean concentration difference are calculated from the average segment temperatures and relative humidity values assuming an ideal gas mixture:

$$P_v = \phi \cdot P_{sat} \tag{3.16}$$

$$C = P_v / \left(T \cdot \overline{R}\right) \tag{3.17}$$

The membrane mass transfer resistance ($R_{m,MT} = \delta/D_m A$) was calculated using different values of representative effective diffusivity (D_m) as described below. The convective mass transfer coefficients in the outdoor and indoor air streams were obtained using the Chilton-Colburn (1934) analogy.

3.1.1.3 Pressure Drop Model

The friction factor for the bare channels and strip fin architectures were calculated using a duct flow correlation (Shah & London, 1978a) for laminar flow. For the micropin-fins, the Fanning friction factor was determined using a correlation for laminar flow through pin-fins developed by B. E. Short, Raad, & Price, (2002):

$$f = 35.1\left(S_p / d\right)^{(-1.3)} \left(T_p / d\right)^{(-0.78)} \left(L_p / d\right)^{(-0.55)} \mathrm{Re}_d^{(-0.65)} \qquad \text{for } \mathrm{Re}_d < 10^3 \tag{3.18}$$

Where,

$$1.9 < L_p / d < 9.6 \qquad 1.8 < S_p / d < 3.2 \qquad 2.0 < T_p / d < 6.4$$

3.1.1.4 Energy and Mass Balance

Energy and mass balances in each segment are required for closure of the iterative model. Figure 3.8 shows a diagram of the flow paths of mass and energy in two counter flow channels in the exchanger. Since the membrane only allows water vapor to pass from one channel to another, the mass flow rate of dry air ($\dot{m}_{f,a}$, $\dot{m}_{e,a}$) does not change in either of the channels. Also, any water vapor leaving one channel must enter one of the channels on either side of it. Eq.(3.19) shows the mass balance for each channel.

$$\begin{aligned} \dot{m}_v &= \dot{m}_{sa}\left(\omega_{si} - \omega_{so}\right) \\ \dot{m}_v &= \dot{m}_{ea}\left(\omega_{eo} - \omega_{ei}\right) \end{aligned} \tag{3.19}$$

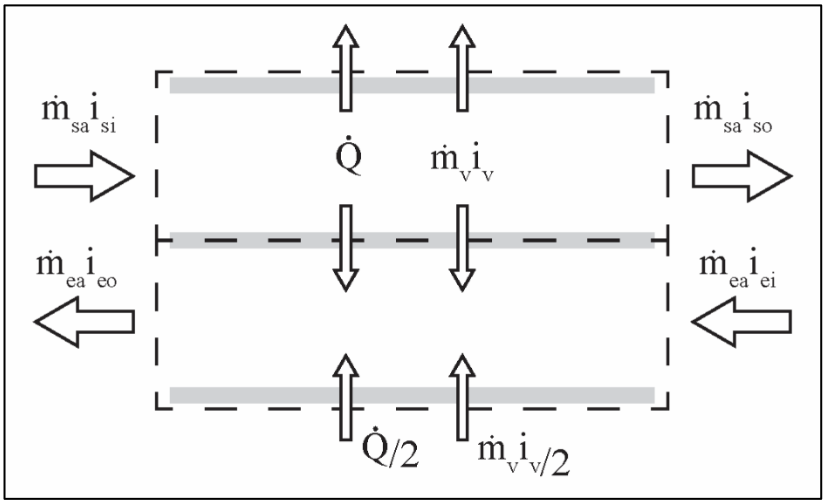

Figure 3.8: Energy and mass balance schematic

A first law analysis of the outdoor and indoor air streams yields the following conservation of energy equations:

$$\begin{aligned} \dot{m}_{sa}\left(i_{si}-i_{so}\right)-\dot{m}_v i_v-\dot{Q}=0 \\ \dot{m}_{ea}\left(i_{ei}-i_{eo}\right)+\dot{m}_v i_v+\dot{Q}=0 \end{aligned} \tag{3.20}$$

Here, the sensible heat transfer ($\dot{Q}$) calculated from Eq.(3.1), the mass flow rate of vapor from Eq.(3.14) and the segment inlet and outlet specific enthalpy are calculated at the local dry bulb temperature, pressure, and humidity ratio. The specific enthalpy of the vapor at the membrane (i_v) is calculated at the average membrane temperature assuming a saturated vapor. The mass and energy balances provide closure to the system of equations and enable an iterative solution.

3.1.1.5 ERV Effectiveness

Finally, the overall performance of the heat and mass exchanger was characterized according to the sensible (Eq.(3.21)) and latent effectiveness (Eq.(3.22)) as defined by AHRI Standard 1060 (AHRI, 2013) for performance rating of air-to-air exchangers for ERV equipment.

$$\begin{aligned} \varepsilon_s=\frac{\dot{m}_{s,a}c_{p,so}\left(T_{si}-T_{so}\right)}{C_{\mathrm{min,s}}\left(T_{si}-T_{ei}\right)} \\ C_{\mathrm{min,s}}=\min\left(\dot{m}_{s,a}c_{p,so},\dot{m}_{e,a}c_{p,ei}\right) \end{aligned} \tag{3.21}$$

$$\varepsilon_l = \frac{\dot{m}_{s,a} h_{fg,so}\left(\omega_{si} - \omega_{so}\right)}{C_{\min,l}\left(\omega_{si} - \omega_{ei}\right)}$$
$$C_{\min,l} = \min\left(\dot{m}_{s,a} h_{fg,so}, \dot{m}_{e,a} h_{fg,ei}\right) \tag{3.22}$$

3.1.1.6 Membrane Deflection

Since both the top and bottom membranes of each channel will deflect, the percent allowable deflection based on deflection of a plate simply supported at two ends with a uniformly distributed load (Boresi & Schmidt, 2003).

$$\%\Delta h_{ch,allow} = \frac{2 w_{\max,def}}{h_{ch}} \tag{3.23}$$

Where

$$w_{\max,def} = C_{def}\left(1-\nu^2\right)\left(\frac{p W_d^4}{E\delta}\right)$$
$$C_{def} = \frac{0.032}{1+0.4\alpha} \tag{3.24}$$

The value of α is the ratio of width W_d to the length of which pressure p is applicable. This value is assumed to be 1 since the pressure p can be assumed constant for a short distance along the channel.

3.1.2 Two-Dimensional Model

The 1D model assumptions are most reliable in parallel or counter flow exchangers with constant membrane properties since the temperature and humidity gradients are expected to be similar along the entire width of the channels (perpendicular to the flow direction). This is not the case for cross or quasi-counter flow exchangers. The temperature or humidity difference may be quite different between two cells along the width of a cross flow exchanger or the headers of a quasi-counter flow exchanger. Additionally, membrane properties are commonly dependent on the local temperature and relative humidity (Al-Waked *et al.*, 2015; Niu & Zhang, 2001). Complexity introduced by cross flow distribution of flow as well as variable membrane properties requires the development of a two dimensional (2D) model (Figure 3.9). The performance of a pin-fin support structure was not investigated using the 2D model since as will be shown in Chapter 4, the 1D analysis indicated an unacceptable pressure drop with this architecture.

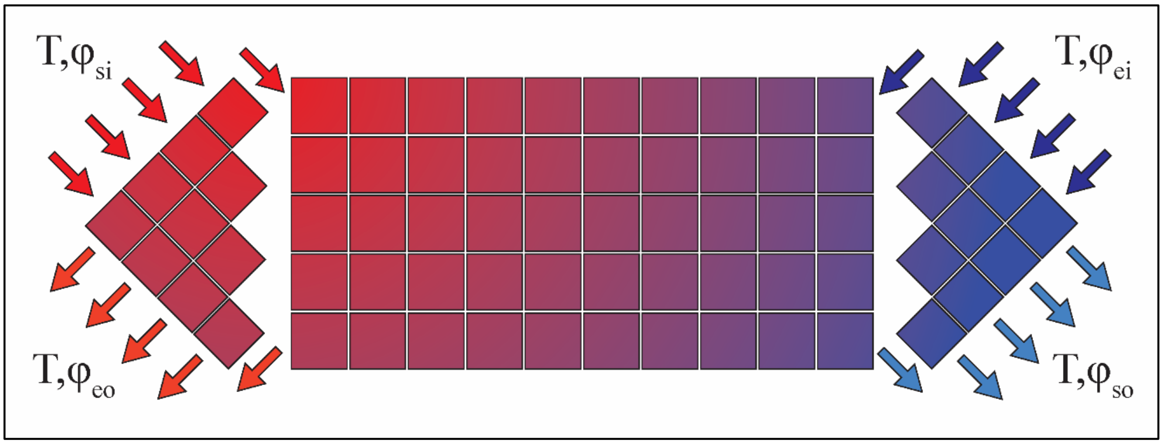

Figure 3.9: 2D segmented model of an ERV

3.1.2.1 Heat Transfer Model

In the transition from 1D to 2D, many segments were added, increasing computational time. In an effort to reduce computational time, the Nusselt number calculation was decoupled from the varying temperature and humidity through the exchanger length and width. Instead, the Nusselt number was calculated for all segment locations using the fresh air and exhaust air inlet property values. This assumption is justified since beyond the dry bulb temperature, humidity, and pressure ranges seen in this study, 23°C to 37°C, 35% to 95%, and 101,325 to 101,675 Pa respectively, the Nusselt number has a maximum change of less than 3%.

3.1.2.2 Mass Transfer Model

The 2D mass transfer prediction includes variation in membrane mass transfer resistance as a function of local temperature and relative humidity throughout the entire channel. The comparison of the 2D model with literature data discussed in Section 3.2.2 includes a membrane resistance function incorporating a sorption function (Eq.(3.25)) obtained from Simonson & Besant (1999),

$$\theta = \frac{w_{\max}}{1 - C + C/\phi_{sw}} \tag{3.25}$$

$$\phi_{sw} = \left(C_{si} - \frac{\dot{m}_v}{MW_{H_2O}\beta_s A_s} \right) \frac{T_{sw}\bar{R}}{p_{sat}\left(T_{sw}\right)} \tag{3.26}$$

$$T_{sw} = T_{si} - \frac{\dot{Q}}{A_s h_s} \tag{3.27}$$

w_{max} is the maximum sorption uptake, C is the sorption curve constant, and T_{fw} and φ_{fw} are the temperature and relative humidity at the membrane surface in the fresh air stream. This sorption curve function was used by Niu & Zhang (2001) and later Al-Waked *et al.* (2015) to find the mass transfer resistance as:

$$R_{m,MT} = \frac{\rho_a}{\rho_m}\frac{\delta}{D_m}\psi \tag{3.28}$$

$$\psi = \frac{10^6\left(1-C+\left(C/\phi_{sw}\right)\right)^2 \phi_{sw}^2}{e^{(5294/T_{sw})} w_{\max} C} \tag{3.29}$$

The density of dry air is ρ_a, and ρ_m is the density of the membrane. Coefficient ψ is the coefficient of mass diffusive resistance (CMDR).

3.1.2.3 Membrane Deflection

The simply supported flat plat model described in Section 3.1.1.6 was valuable for getting a membrane deflection value but is not directly applicable to very thin membrane materials. In light of this, a model developed by Xiang, Chen, & Vlassak (2005) and later Larson, Simonson, Besant, & Gibson (2007) was implemented specifically designed to model deflection of thin films under pressure (Eq.(3.30)).

$$p = c_1 \frac{E\delta}{(1-\nu)(W_d/2)^4} w_{\max,def}^3 + c_2 \frac{\sigma_0 \delta}{(W_d/2)^2} w_{\max,def} \tag{3.30}$$

Where the membrane pre-stress, σ_0, is set equal to zero, cancelling the right term. This model also assumes a square membrane.

3.2 Comparisons with Literature Data

3.2.1 One-Dimensional Model

The 1D modeling approach outlined above was compared to the CFD results of Zhang (2010). In his study, Zhang (2010) considered a pure counterflow membrane ERV, pure cross flow, pure cocurrent flow, and a “quasi-counterflow”, each with bare parallel channels. The quasi-counterflow was similar to the architecture in the present study, where a portion of the flow is cross-flow like (in the headers), with counterflow in the body of the exchanger. Zhang (2010) compared his numerical model to experimental results from the quasi-counterflow and reported maximum deviations of 5.6% and 8.3% between predicated and experimental results for latent and sensible effectiveness, respectively.

Using the same inlet conditions, ERV geometry and membrane properties (Table 1), the predicted latent and sensible effectiveness from the present model were compared with the results of Zhang (2010) for quasi-counter, counter, and cocurrent flow orientation for air flow rates from 38.9 to 194.7 $m^3\ hr^{-1}$ (23 to 114.6 $ft^3\ min^{-1}$). A comparison of all points is shown in Figure 3.10a and Figure 3.10b for the sensible and latent effectiveness respectively. For an accurate comparison, sensible and latent effectiveness were calculated using the definitions from Zhang (2010) (Eq.(3.31) and Eq.(3.32)), instead of Eq.(3.21) and Eq.(3.22) from (AHRI, 2013).

$$\varepsilon_s = \frac{T_{si} - T_{so}}{T_{si} - T_{ei}} \tag{3.31}$$

$$\varepsilon_l = \frac{\omega_{si} - \omega_{so}}{\omega_{si} - \omega_{ei}} \tag{3.32}$$

Compared to the Zhang (2010) CFD model, the proposed 1D network model exhibited an absolute average deviation (AAD, Eq.(3.33)) for the counter and cocurrent model of 1.59% and 5.35% for sensible and latent effectiveness, respectively. For the quasi-counterflow model, the AAD was 3.26% and 10.04% for sensible and latent effectiveness, respectively.

$$AAD = \frac{\displaystyle\sum_{n=1}^{\#\text{ data points}} \left(\frac{\left| \varepsilon_{\text{model}} - \varepsilon_{\text{Literature}} \right|}{\varepsilon_{\text{Literature}}} \cdot 100 \right)}{\#\text{ data points}} \tag{3.33}$$

The AAD is the average of the absolute percent difference between the model and literature effectiveness values over a range of inlet conditions, usually various flow rates. Since the data is expected to vary with flow rate and is compared to other data, AAD is preferred over standard deviation or variance. Standard deviation and variance compare data to the mean. In these comparisons, the mean effectiveness is not a relevant value of comparison.

Table 3.2: Geometry, inlet conditions and membrane properties from Zhang (2010)

Variable	Value	Unit	Variable	Value	Unit
N	57	[-]	h_{ch}	4	mm
W_{ch},L_{body}	185	mm	θ	90	degrees
δ	102	μm	k_m	0.13	W m^{-1} K^{-1}
k_a	0.0263	W m^{-1} K^{-1}	D_m	8×10^{-6}	m^2 s^{-1}
A_{tot}	5.85	m^2	D_a	2.82×10^{-5}	m^2 s^{-2}
T_{si}	35	°C	φ_{si}	59	%
T_{ei}	27	°C	φ_{ei}*	54	%

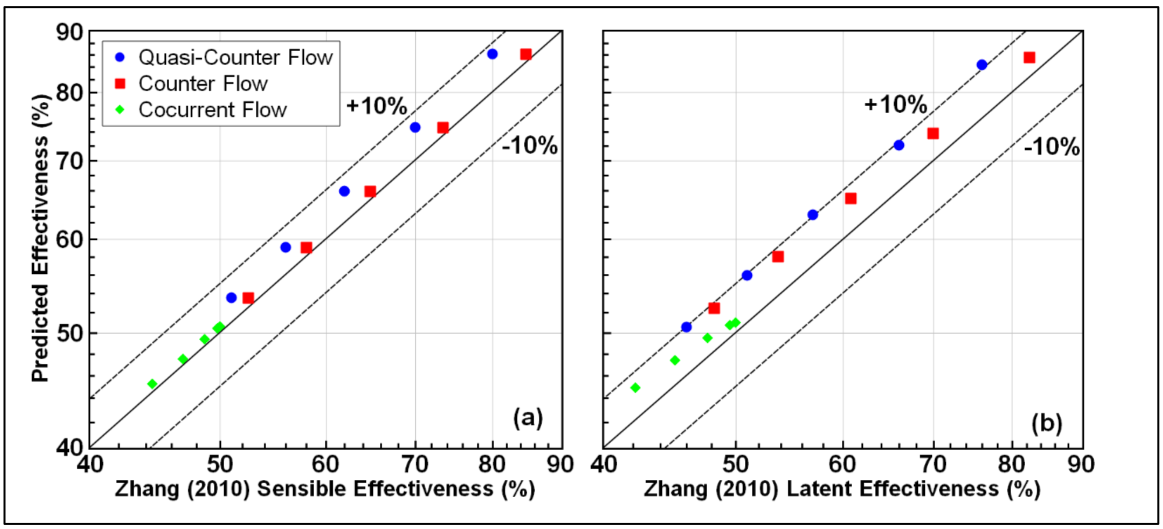

Figure 3.10: 1D model compared (a) sensible and (b) latent effectiveness with various flow configurations

As can be seen from Figure 3.10, the 1D quasi-counterflow model tends to over predict the latent effectiveness compared to the CFD model, particularly at low airflow rates. At the highest effectiveness value (lowest flow rate), the deviation is 11%, which suggests even greater deviation in the overall mass transfer coefficient for an equivalent area. As the agreement between the 1D model and Zhang's (2010) results are reasonable for all the other geometries (AAD = 5.35%, where Zhang (2010) reports agreement of his model within 5.6% with experimental data), one likely explanation is that the 1D model does not account for flow maldistribution within the channel and how this effects flow development and concentration distribution. Zhang (2010) notes that for all his simulated cases, the flow is developing for a large percentage of the total flow area. In the present model, we use standard solutions for developing laminar flow in straight, rectangular ducts. So while this assumption provides reasonable results for counter or cocurrent flow (where the effects of maldistribution are expected to be less important), the deviation is greater for the quasi-counter flow geometry, particularly at very low flow rates where maldistribution is significant. The other potential explanation is that while the present study uses the Chilton & Colburn (1934) analogy to predict mass transfer from heat transfer predictions, the heat and mass transfer analogy used by Zhang (2010) is not reported. The uncertainty in the model due to uncertainty in the input parameter for the quasi-counterflow geometry is further explored in Section 5.2.

3.2.2 Two-Dimensional Model

3.2.2.1 Constant Membrane Properties

The membrane mass transfer resistance in Zhang's (2010) model is constant. Thus, it was desired the 2D model be compared to Zhang's (2010) model as well as a model with variable membrane resistance as it better represents actual expected conditions. First, the constant membrane results from Zhang (2010) were compared with the 2D model for quasi-counter flow and cross flow orientations as shown in Figure 3.11. The AAD for the 2D quasi-counter flow orientation of the sensible and latent effectiveness are 4.66% and 9.75% respectively. The cross flow sensible and latent AAD values are 1.83% and 4.95% respectively.

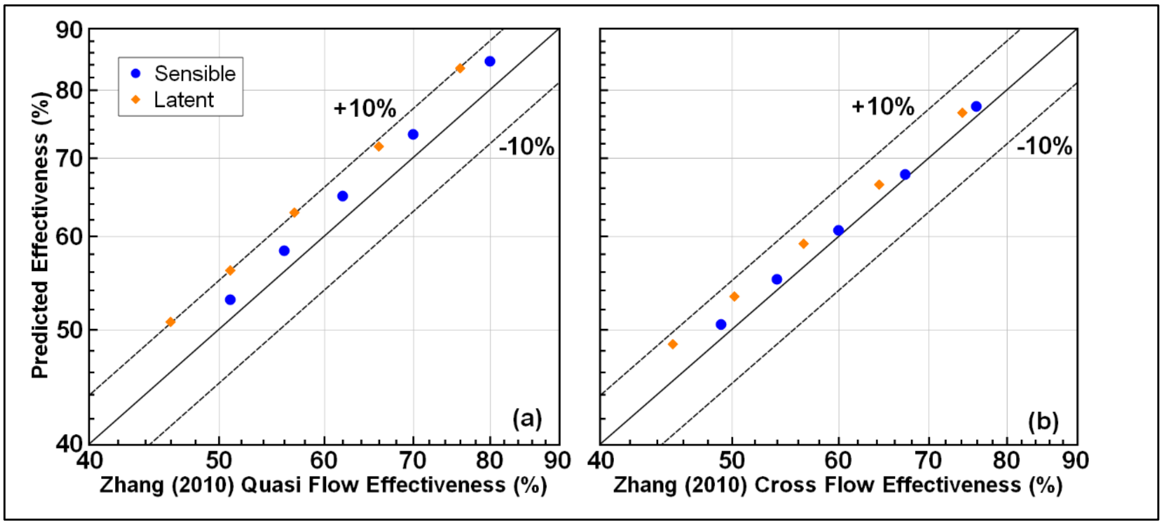

Figure 3.11: 2D model compared (a) sensible and (b) latent effectiveness with quasi-counter and cross flow conditions

Notice the sensible effectiveness predicted by the 1D model in Section 3.2.1 is better (AAD = 3.26%) than the predicted values from the 2D model (AAD = 4.66%). The latent effectiveness was better predicted by the 2D model with an AAD = 9.75% while the 1D model had an AAD = 10.04%. This behavior may be indicative of the heat transfer having a stronger sensitivity of the air property assumptions made in the 2D model. The convective heat transfer greatly dominates the often negligible membrane resistance as compared to the mass transfer where the membrane is often the larger resistance compared to the convection. This makes property assumptions more important for predicted the sensible effectiveness. It is also possible, as will be discussed in Section 3.5.3, the inlet flow direction assumption errors were magnified in the 2D model. An incorrect assumption regarding the inlet flow direction into the quasi-counter ERV would provide a different temperature distribution in the 2D model which would be less accurate than the 1D model which assumes a more evenly distributed temperature profile.

3.2.2.2 Variable Membrane Properties

An ERV model developed by Al-Waked *et al.* (2015) uses a variable membrane mass transfer model which is a function of temperature and relative humidity described in Section 3.1.2.2 by Eq.(3.28). The exchanger used in the work done by Al-Waked *et al.* (2015) was for modeling a cross flow configuration. The properties of a cellulose acetate (CA) membrane and a modified cellulose acetate (MCA) membrane investigated by Al-Waked *et al.* (2015) are shown in Table 3.1, with the modeled inlet conditions and exchanger dimensions are given in Table 3.4.

Table 3.3: Membrane properties from Al-Waked *et al.* (2015)

Variable	CA Value	MCA Value	Unit
D_m	1.05×10^{-11}	1.12×10^{-11}	$m^2\ s^{-1}$
w_{max}	0.43	2.5	-
C	11.4	8.64	-
ρ_m	760	773	$kg\ m^{-3}$

Table 3.4: Geometry and inlet conditions from Al-Waked *et al.* (2015)

Variable	Value	Unit	Variable	Value	Unit
N	115	-	T_{si}	35	°C
δ	5	μm	T_{ei}	27	°C
W_{ch}	185	mm	φ_{si}	59	%
k_m	0.41	$W\ m^{-1}\ K^{-1}$	φ_{ei}	54	%

The sensible and latent effectiveness values predicted by the 2D model for both the CA and MCA membranes are compared to the values provided by Al-Waked *et al*. (2015) in Figure 3.12. The AAD for the sensible and latent effectiveness predicted for the CA membrane are 0.11% and 0.91% respectively. For the MCA membrane, the AAD for the sensible and latent effectiveness values are 0.16% and 1.26% respectively. The ability of the 2D model to predict values in the literature to this degree provides great confidence in the capability of the resistance network model to predict the effectiveness of other ERVs with different membrane properties, internal geometries, and boundary conditions.

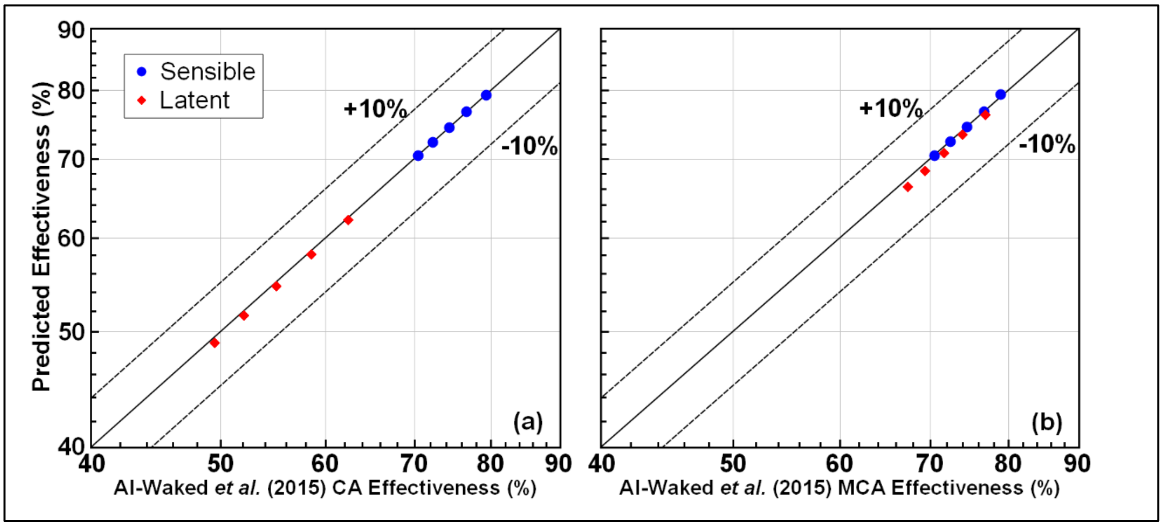

Figure 3.12: 2D model compared sensible and latent effectiveness for (a) CA and (b) MCA type membranes

Al-Waked *et al.*, (2015) also provides a contour map of the membrane mass transfer resistance, $R_{m,MT}$, results for the MCA membrane as shown in Figure 3.13. In an effort to further evaluate the predictive capabilities of the 2D model, the contour map was reproduced using the predicted resistance values (Figure 3.14).

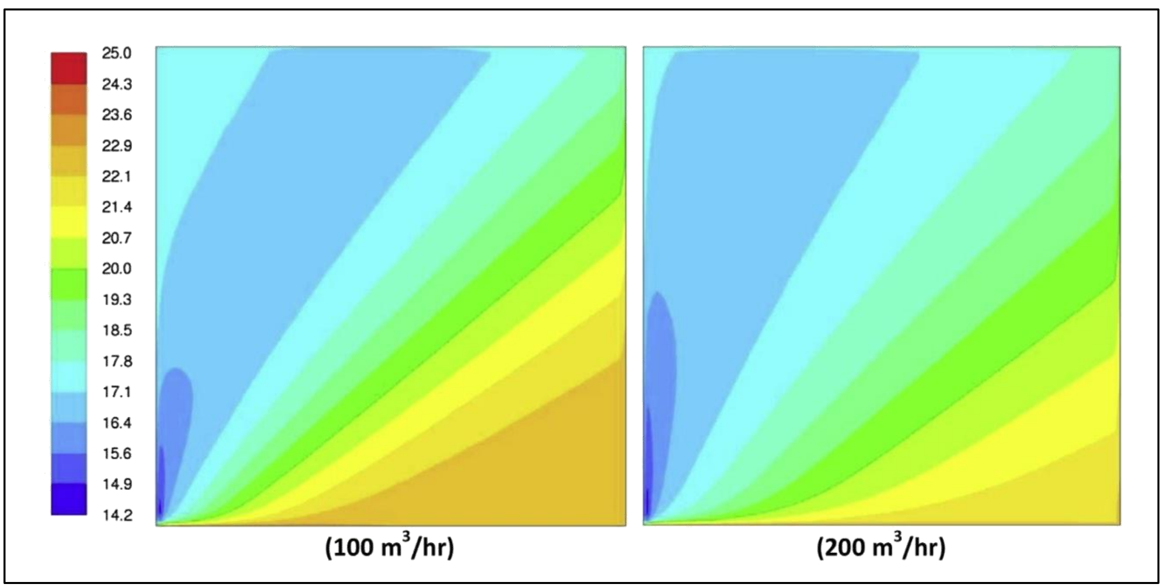

Figure 3.13: Membrane resistance ($R_{m,MT}$) across MCA membrane layer at two flowrates from Al-Waked *et al.* (2015)

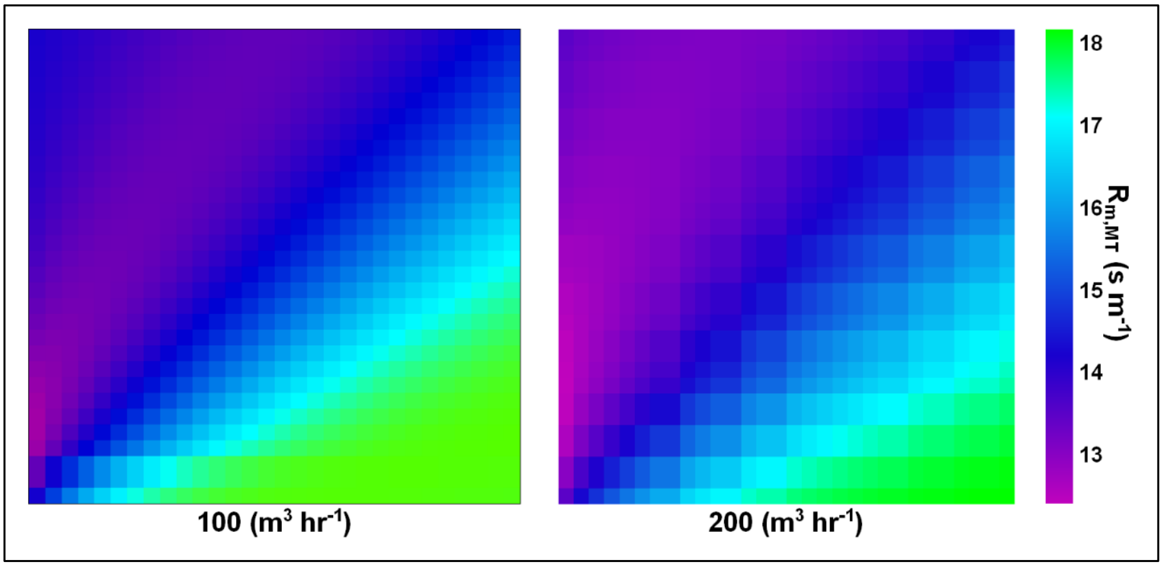

Figure 3.14: 2D model predicted membrane resistance ($R_{m,MT}$) across MCA membrane layer at two flowrates

The upper bound of the membrane mass transfer resistance reported by Al-Waked *et al.* (2015) is suspect since the resistance calculated at the supply state values is 18.09 s m^{-1} while Al-Waked *et al.* (2015) claims 25 s m^{-1} and resistance values above 20 s m^{-1} are shown in Figure 3.13 at the supply inlet (bottom edge). However, while the 2D model predicts smaller resistance values than reported by Al-Waked *et al.* (2015), qualitatively, the contour maps look very similar. Both models show the reduced resistance variation across the membrane layer with increased flow rate. Since the predicted effectiveness values were within 1.5% of the literature values as shown in Figure 3.12 the apparent difference in membrane mass transfer resistance is of little concern.

3.3 Model Discretization and Grid Convergence

It is important to understand the impact model discretization has on the predicted effectiveness and pressure drop values. A grid convergence study was performed using the quasi-counter flow design developed with the 2D model in Section 4.2.6. The percent change in predicted sensible and latent effectiveness and pressure drop with an increasing number of segments is shown in Figure 3.15.

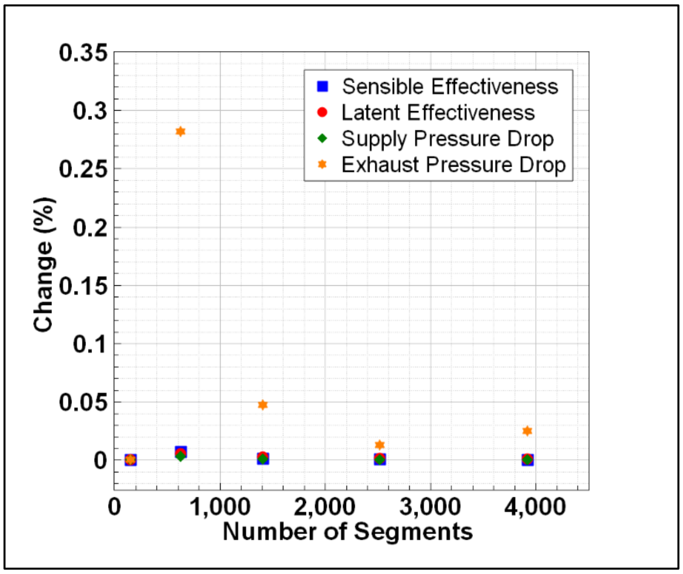

Figure 3.15: 2D model grid convergence study

There were two main factors limiting the number of segments used in this model. First, the rectangular duct friction factor function can only provide local friction factors for the developing region at distances greater than 10% of the hydraulic diameter. Second, the commercial version of Engineering Equation Solver (Klein, 2015) can solve no more than 6,000 simultaneous equations in a program or subprogram. Correlations are used to define the heat and mass transfer coefficients and the local friction factors. Thus, an increase in the number of segments does not significantly change the predicted effectiveness or pressure drop values as it might in solving the temperature, concentration, and velocity profiles in a CFD program. From 630 to 1,410 segments, the percent change in predicted performance metrics were all less than 0.05%. Since the computational time did not increase much with the addition of segments, close to the maximum allowable number of segments was used in this work. For the 2D quasi-counter flow model, this was 3,925 segments, 133×25 in the body and 300 segments in each header.

3.4 Heat Transfer Verification

In the resistance network model, the fluid flow field is assumed to be known and the mass transfer is assumed to be analogous to the heat transfer. This makes the accuracy of the heat transfer prediction all the more important. There are well established heat exchanger effectiveness relations available for comparison to verify the predicted sensible effectiveness is reliable. In Figure 3.16, the predicted effectiveness values for a counterflow heat exchanger are compared to an ε-NTU correlation for several C_r values. The maximum percent difference was 0.02%. This provides assurance the model is able to predict reasonable sensible effectiveness values.

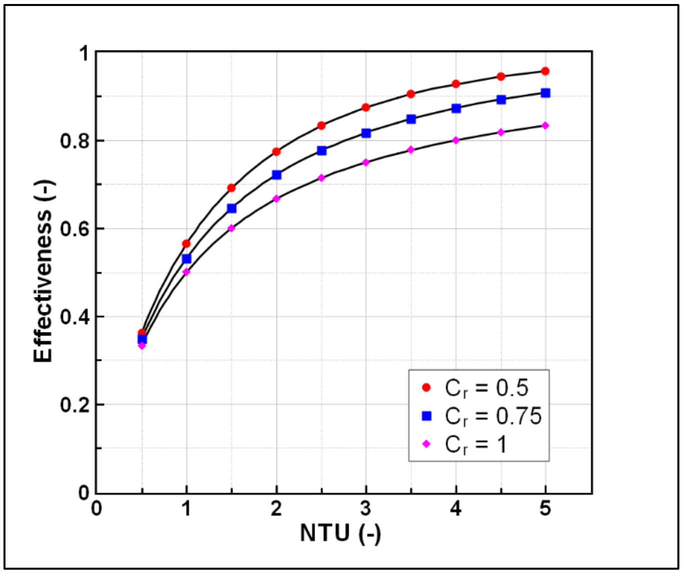

Figure 3.16: Counterflow ε-NTU correlation vs 1D model prediction

3.5 Resistance Network Approach Considerations

Comparing the predicted sensible and latent effectiveness values to the literature does show good predictive capability. However, there are considerations to take into account when implementing a network resistance approach for modeling effectiveness. In this section, the potential issues regarding cross flow correction factors, the relationship between effectiveness and the number of transfer units (NTU), and the inlet flow direction for quasi-counter ERVs will be discussed.

3.5.1 Cross Flow Correction Factors

The cross flow correction factors discussed in Section 3.1.1.1 approach unity as the number of segments and flow rates increase. As segment size decreases, calculation of the cross flow correction factors can cause computational issues. The calculated cross flow correction factors observed for both heat and mass transfer were seldom found to be less than 0.95 for conditions of interest in the present study. Therefore, these coefficients were assumed to be equal to unity for all studies. The effect of changing the cross flow coefficients was studied. The sensible and latent effectiveness values were predicted with F_{ht} and F_{mt} set equal to 0.9 and 1.0 at various flow rates. Then, the percent difference in effectiveness was calculated. The percent difference in predicted effectiveness using Zhang's (2010) quasi-counter and cross flow parameters was less than 2% and 5% respectively as shown in Figure 3.17.

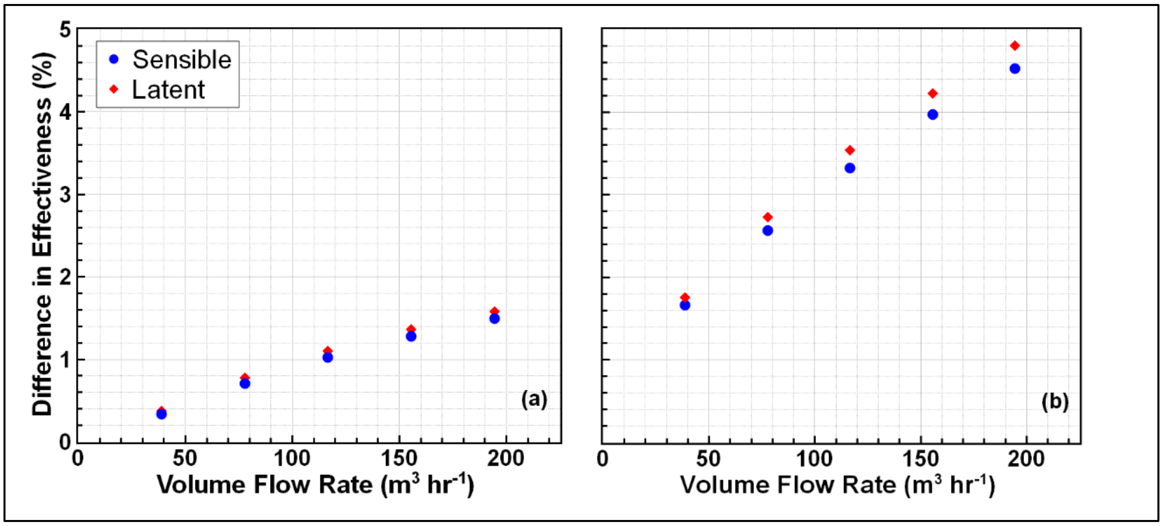

Figure 3.17: Effect of cross flow correction factor on predicted effectiveness at various flow rates for (a) quasi-counter flow and (b) cross flow configurations

In the same way, parameters from Al-Waked *et al.* (2015) were used to study the impact the cross flow correction coefficients have on variable membrane property ERV effectiveness predictions. The percent differences in effectiveness for the CA and MCA membranes were less than 5% and 3% respectively as shown in Figure 3.18.

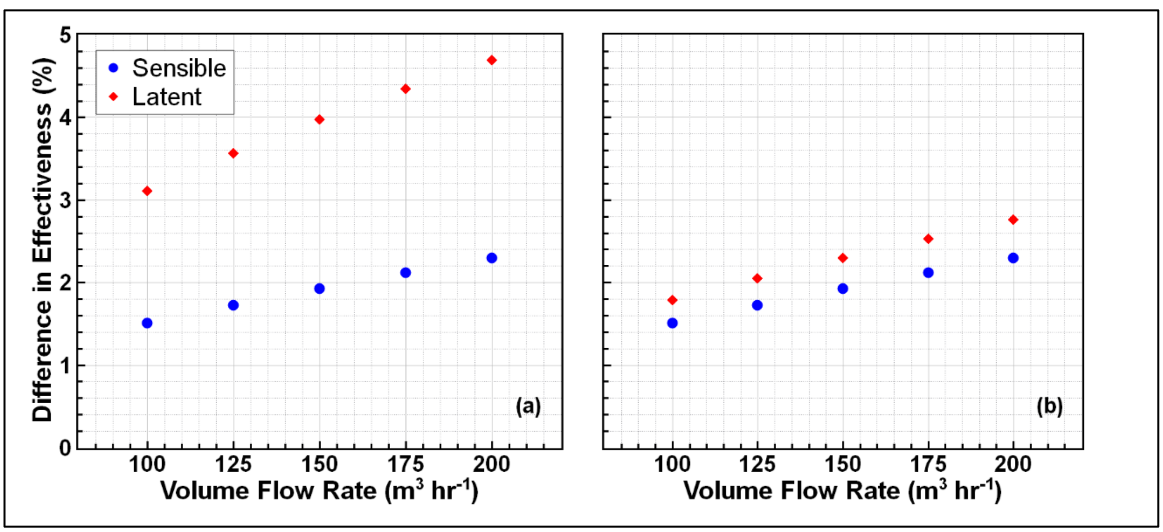

Figure 3.18: Effect of cross flow correction factor on effectiveness at various flow rates for (a) CA and (b) MCA membranes

3.5.2 Effectiveness Sensitivity to NTU

A recurring trend seen in the comparison of the resistance network models to the literature data is the increase in percent difference between predicted and literature effectiveness values with increase in flow rate. This phenomena is indicative of the insensitivity of effectiveness to the heat and mass transfer rate or NTU as the effectiveness approaches 100% as shown in Figure 3.19. This means an apparent small percent difference between predicted and literature effectiveness seen at a low flow rate (high effectiveness) may be a misrepresentation of the ability of the model to predict the heat and mass transfer in an ERV. Ideally, the NTU of the exchanger would be compared with the literature. However, the HVAC industry and the literature on the topic all consider effectiveness as the standard measure of ERV performance.

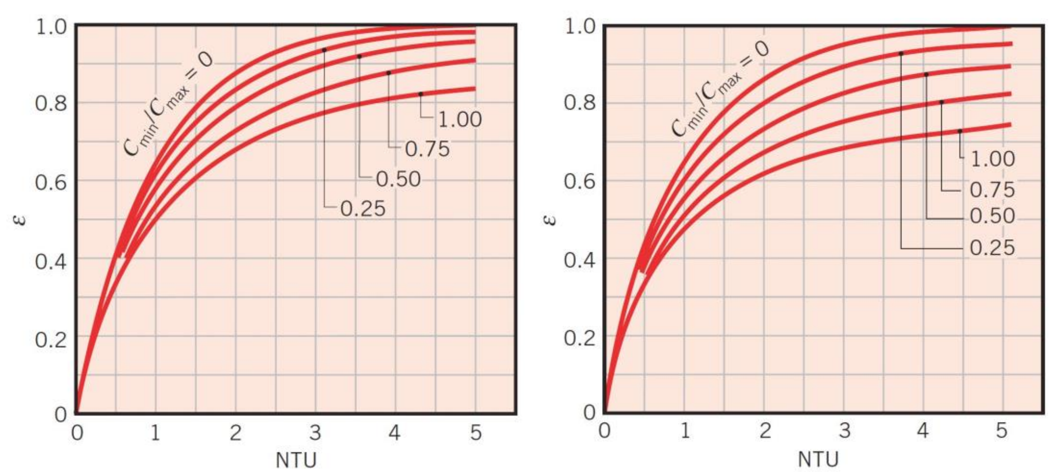

Figure 3.19: Effectiveness vs NTU for (a) counter and (b) cross flow exchangers (Incropera, DeWitt, Bergman, & Lavine, 2007)

3.5.3 Quasi-Counter Flow Inlet Direction

The overprediction in effectiveness of the quasi-counter flow configuration was particularly high compared to all other flow configurations for the 1D models as well as the 2D models (Figure 3.10 and Figure 3.11). Al-Waked, Nasif, Morrison, & Behnia (2013) provide some insight regarding this flow configuration and the impact of inlet flow direction. In Figure 3.20, they show the impact of flow direction on the sensible and latent effectiveness of a quasi-counter flow ERV.

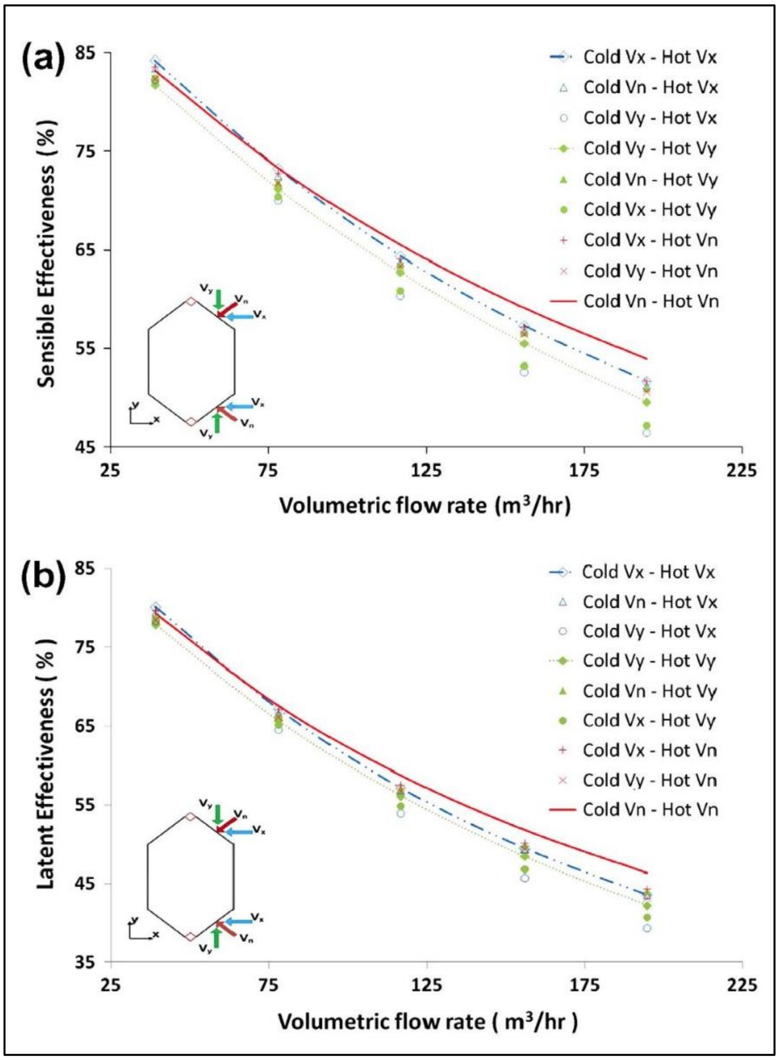

Figure 3.20: Effect of inlet flow direction on ERV (a) sensible and (b) latent effectiveness (Al-Waked *et al.*, 2013)

The V_y variable shown in Figure 3.20 represents the inlet flow direction assumed by Zhang (2010), Al-Waked *et al.* (2013), and Al-Waked *et al.* (2015) for both inlets. This flow direction is along the length of the exchanger. In the resistance network model, the V_n direction was assumed for both inlets. This flow direction is normal to the inlet. Figure 3.20 shows a greater predicted ERV performance with the inlet flow normal to the inlet of the ERV compared to the inlet flow along the length of the exchanger. This effect is more visible at the higher flow rates. A normal inlet flow direction was used in the resistance network model to simplify the flow paths in the channel. A minimum flow velocity is achieved at the inlet when the flow is normal to the inlet. While increases in velocity can improve the convective heat and mass transfer coefficients at the inlets, the improved resonance time with slower velocities at the inlets may provide greater heat and mass transfer overall for a given volume flow rate. The strip-fin internal support structure will guide the flow normal to the inlet. This makes the assumption of normal inlet flow more meaningful and may further explain discrepancies observed in Figure 3.10 and Figure 3.11.

3.6 Summary

A 1D and 2D resistance network approach to modeling the performance of several ERV flow configurations was described. Both resistance network models proved to be capable of predicting the sensible and latent effectiveness of ERVs of several flow configurations at a low computational cost. Prediction of pressure drop was not compared to literature data but is validated using experimental data in Chapter 5. Considering potential issues regarding cross flow, effectiveness vs NTU, and inlet flow direction can possibly explain differences in predicted and literature results. This modeling approach is of great value for the rapid design of an ERV discussed in Chapter 4.

Chapter 4: Model Application and Fabrication Challenges

With the model developed in Chapter 3, the performance of different ERV designs can be predicted. This chapter discusses the design of a full scale ERV and the design and fabrication of a prototype ERV using the models developed in Chapter 3. This chapter also presents an investigation to identify the design space possible with a new manufacturing technique, discussed in greater detail below. Thus, the designs introduced in this chapter satisfy both heat and mass transfer performance criteria, and can be fabricated using a new technique. The design targets for the ERV are as follows:

- AHRI Standard 90% sensible effectiveness
- AHRI Standard 83% latent effectiveness
- 300 Pa pressure drop
- 300 CFM flow rate of supply and exhaust streams
- Fits within a work envelope of 0.175 m × 0.7 m × 1.0 m

4.1 Fabrication Constraints

4.1.1 Membrane Properties

A 25 micron thick polymer membrane was specified for the construction of this ERV. This membrane has excellent selectivity and exceptionally low heat and mass transfer resistance. The membrane is also relatively inexpensive so as not to be a limiting factor for ERV cost. While the membrane is high performing, there are significant challenges in incorporating it into an ERV device due to its mechanical properties. The small thickness of the membrane means a layer will not support itself if the edges are supported as is possible with more ridged membranes (Li Zhi Zhang et al., 2008). In some cases, thin membranes can be corrugated or pleated to support the channels with triangular to sinusoidal passages (Gendebien, Bertagnolio, & Lemort, 2013; Li Zhi Zhang, 2008). The membrane under consideration does not have the ability to be pleated since folds and creases do not stay in place as they do with paper membranes. Furthermore, membrane deflection caused by channel-to-channel pressure variation can cause flow maldistribution, high pressure drop and premature failure of the device. This is especially the case for the most effective exchanger flow configuration, counter flow. As shown in Figure 4.1, the pressure across the membrane can cause deflection, decreasing the flow area of lower pressure channels and increase the air stream pressure drop. This in turn increases the pressure across the membrane and increases deflection. This unfortunate coupling of fluid flow and membrane deflection can be mitigated by an internal support structure.

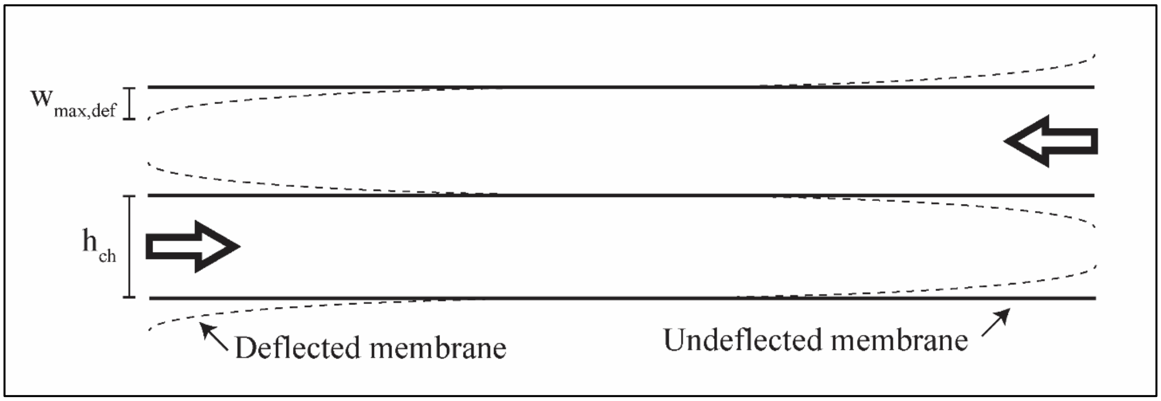

Figure 4.1: Schematic of deflection in counter flow channels without support structure

4.1.2 Internal Support Structure

Since the membrane cannot be pleated to provide support, a technique to integrate a support structure in parallel with the joining of adjacent membrane layers was proposed by the project team. The support structure is made of a moisture cure adhesive. This adhesive is dispensed onto the membrane using a computer controlled dispenser in a flow pattern. After this, another membrane is positioned on top of the adhesive and a small force is applied to ensure adequate adhesion. Then, the cycle is repeated with alternating reflected images of the flow pattern until the desired number of layers is created. A schematic of the dispensing processes is shown in Figure 4.2

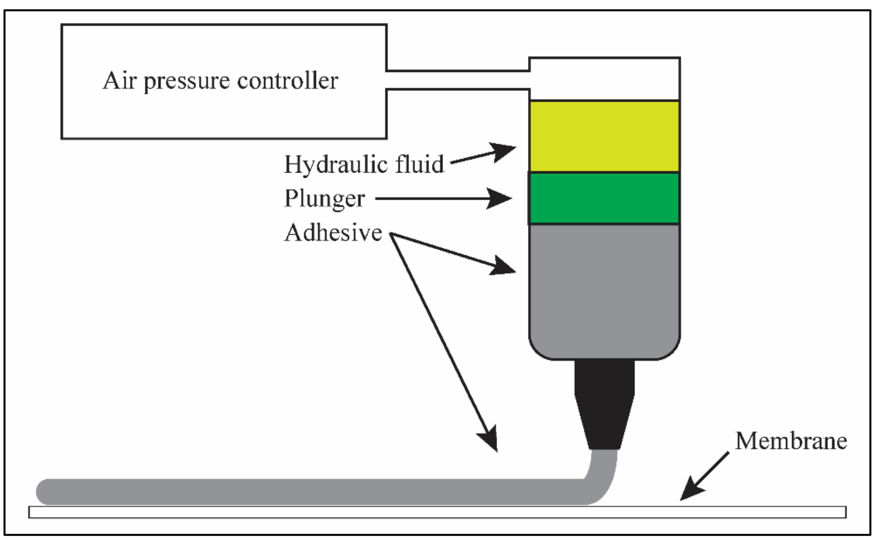

Figure 4.2: Adhesive dispense schematic

This dispensing process enables a more automated process, reducing manufacturing costs. By controlling how the aspect ratio, height, and bead-to-bead spacing, a single membrane layer can be separated into multiple parallel channels with varying hydraulic diameter. Thus, the heat and mass convective resistances as well as the pressure drop can be controlled with the dispensed pattern. The dispensed pattern can also be controlled to control flow distribution, and prevent leakage and mixing of airstreams. Examples of these patterns are shown in Figure 4.3 and Figure 4.4.

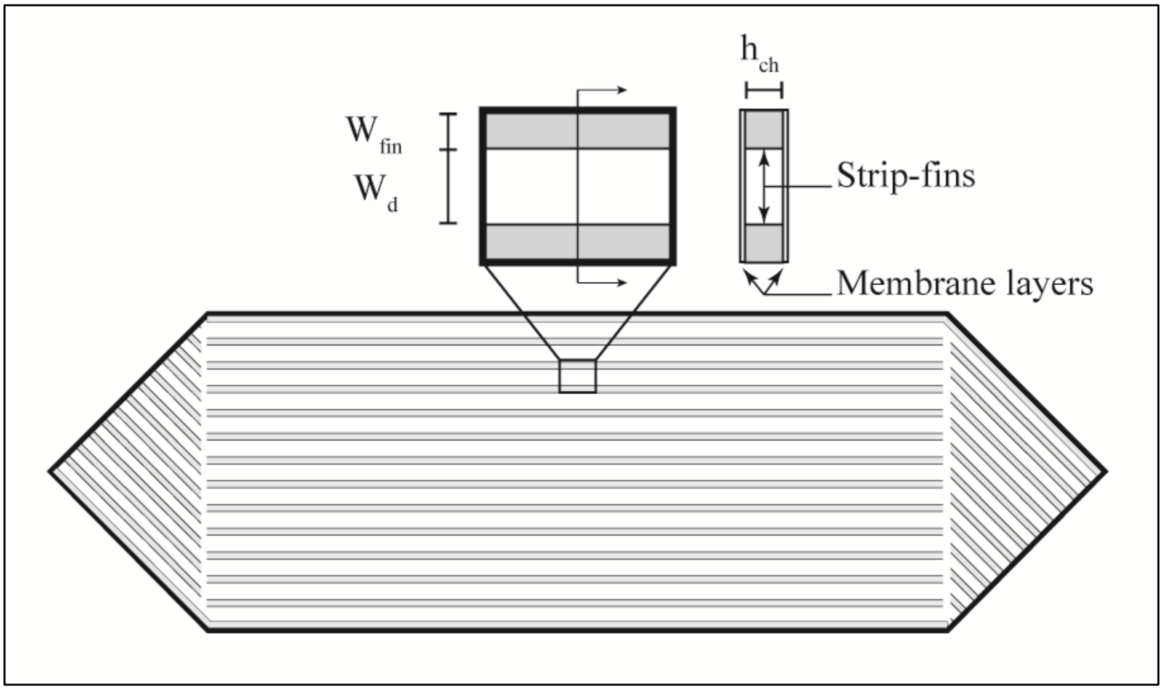

Figure 4.3: Strip-fin geometry

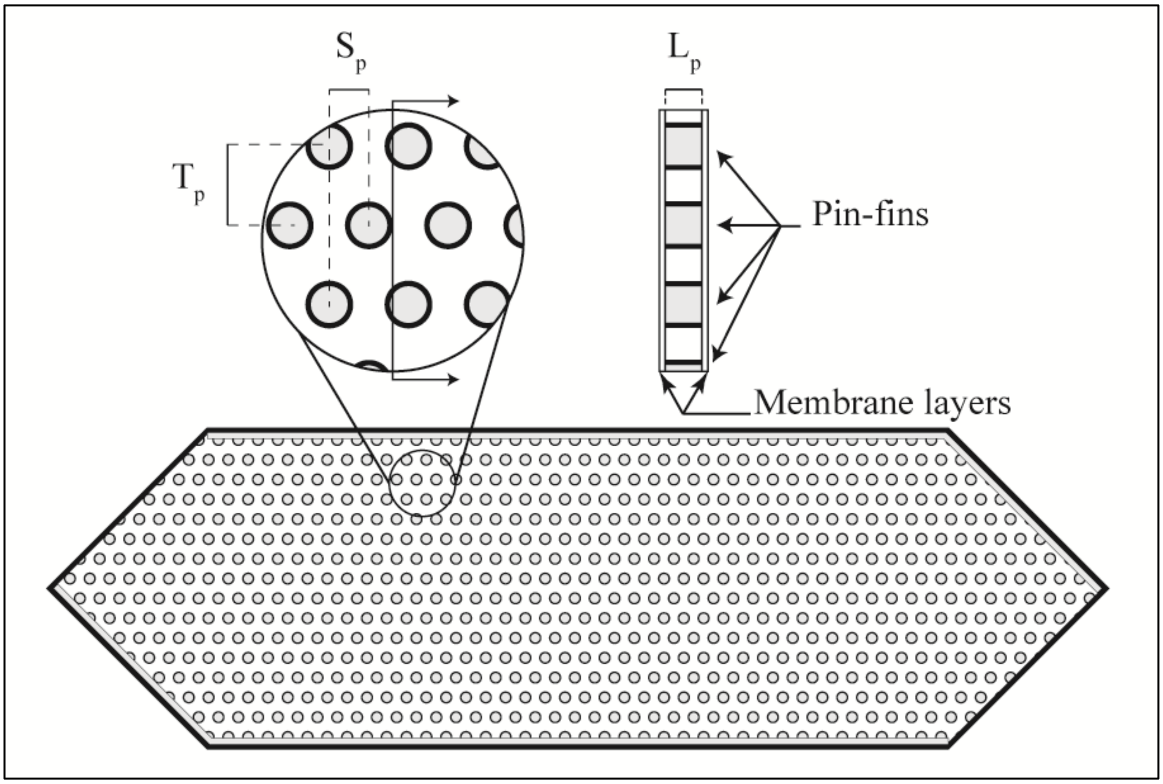

Figure 4.4: Pin-fin geometry

After a pattern was dispensed on a base membrane layer, the membrane layer to be bonded on top was held and placed by the bonding unit shown in Figure 4.5. The unit was composed of a vacuum chuck designed to hold the membrane during bonding and a linear motion system to place the membrane on the adhesive strip-fin pattern at a precise location.

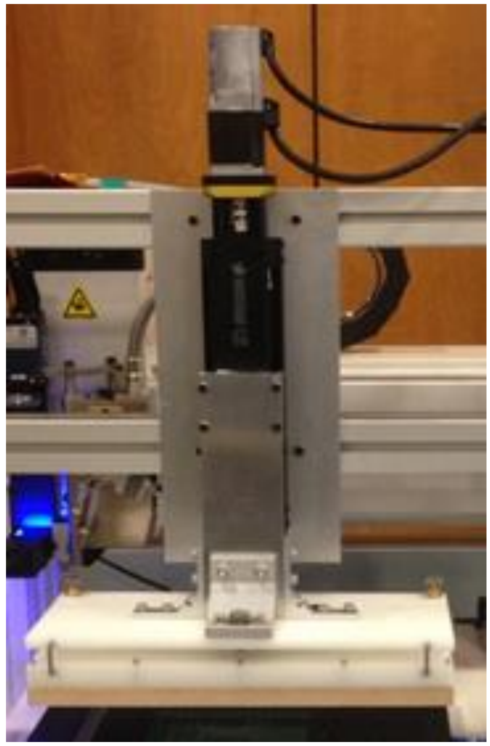

Figure 4.5: Membrane placement and bonding unit

4.2 Exchanger Design

4.2.1 Work Envelope and ERV Orientation

For the full-scale ERV, a quasi-counter flow configuration was selected for the combined benefits of simple flow routing similar to the cross flow configuration but increased performance due to the counter flow section in the middle of the ERV as discussed by Zhang (2010). The work envelope enabled two orientation options for the ERV. As shown in Figure 4.6a, a tall and narrow exchanger (ERV A) could be fabricated with the width of the channels as the smallest work envelope dimension. The other option is shown in Figure 4.6b (ERV B), where the height is set to the smallest work envelope dimension. ERV A and ERV B represent these geometries at the maximum allowable dimensions. Some general observations regarding the expected difference in performance and manufacturability of both of these devices can be made before any modeling is required.

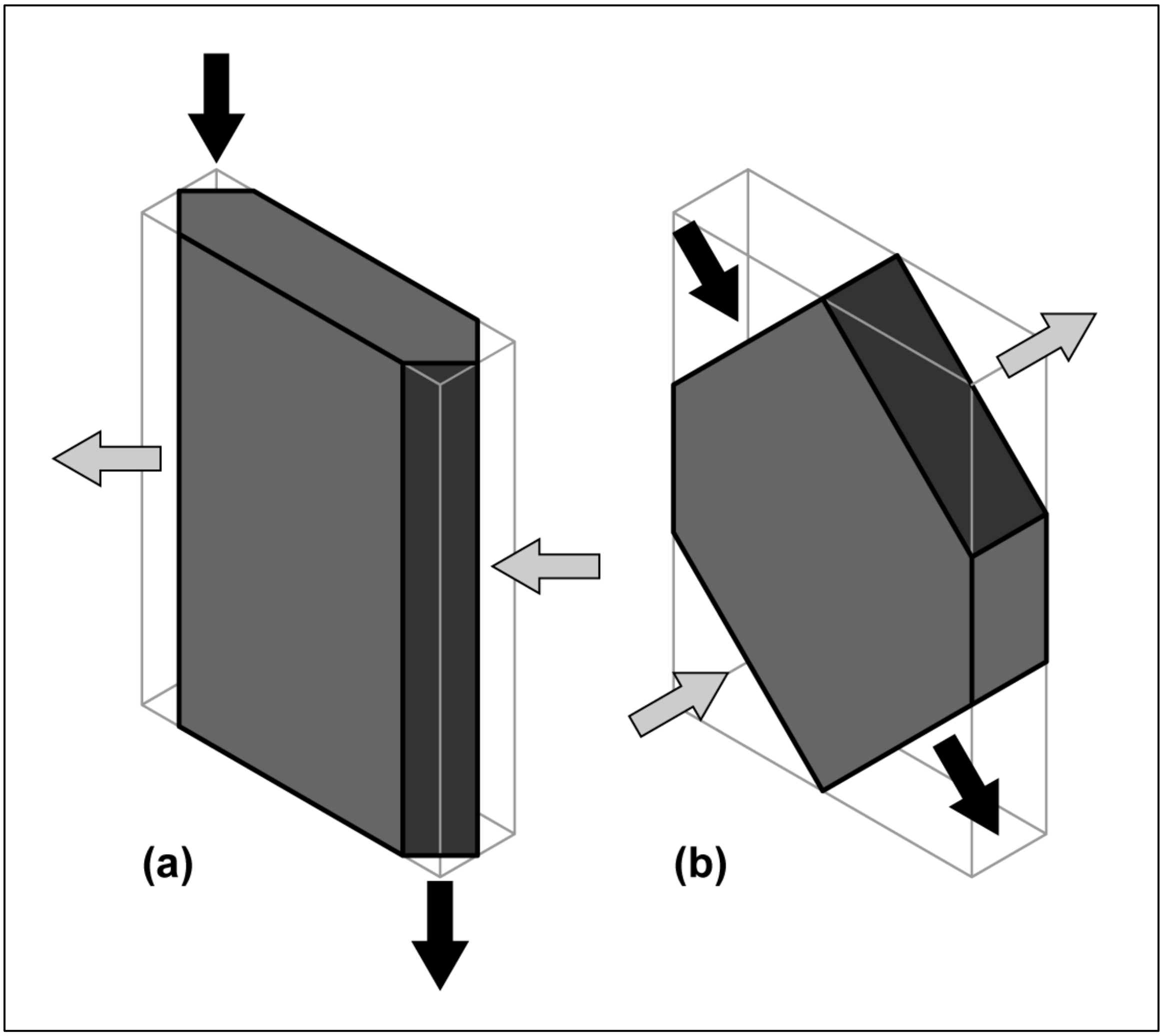

Figure 4.6: (a) Tall and narrow and (b) short and wide quasi-counter flow configuration options in working envelope

The largest differences in the fabrication of these two devices would differ with respect to the dispense area (footprint) and the number of channels to be bonded. The ERV A orientation has a footprint less than ¼ that of ERV B but requires over 4 times the number of channels for the same ERV volume and channel height. An increase in the number of required channel bonds can increase the fabrication time substantially. However, the large footprint of ERV B can increasing capital cost and dispense time per layer. A longer dispensing time between bonds requires a longer curing time for the adhesive. With the manufacturing cost constraints considered, the performance of both ERV orientations can be investigated.

First, ERV A uses 87.5% of the available work envelope volume while ERV B uses only 65%. As Zhang (2010) mentions, the counter flow region will provide more heat and mass transfer than the cross flow regions in the headers. The volume dedicated to counter flow channels in ERV A is 2.5 times that of ERV B. Finally, the inlet area of ERV A is over 40% larger than that of ERV B. The larger inlet area in ERV A reduces the bulk velocity, reducing the pressure drop in both the headers and the body by about a factor of two for a given length compared to ERV B assuming equal fluid properties and internal geometries. The greater use of work envelope space, the large proportion of the exchanger that is of a counter flow configuration, and the decrease in pressure drop per unit length make ERV A a much better candidate for further study.

4.2.2 Comparison of pin-fin vs strip-fin internal support structure

A parametric study of an ERV with the orientation of ERV A from the previous section was conducted with the 1D resistance network model to evaluate the merits of strip-fin and pin-fin internal support structure geometries shown in Figure 4.3 and Figure 4.4 respectively. An ERV is modeled with the dimensions and membrane properties shown in Table 4.1 with the AHRI rating conditions shown in Table 4.3. The dimensions of the pin-fin geometry shown in Table 4.2 were chosen such that the hydraulic diameter was equal to 2 mm, the same as the hydraulic diameter of the strip-fin design. The overall exchanger dimensions are displayed in Figure 4.7.

Table 4.1: Details of 1D model baseline design

Variable	Value	Unit	Variable	Value	Unit
L	750	mm	D_m	4.3×10^{-7}	$m^2\ s^{-1}$
W_{ch}	175	mm	δ	25	μm
H	1000	mm	AR_{st}	1	[-]
k_m	0.0765	$W\ m^{-1}\ K^{-1}$	AR_d	4	[-]

Table 4.2: ERV pin-fin dimensions

Variable	Value	Unit
L_p	1.25	mm
L_p/d	1.9	-
S_p/d	3.2	-
T_p/d	6.4	-

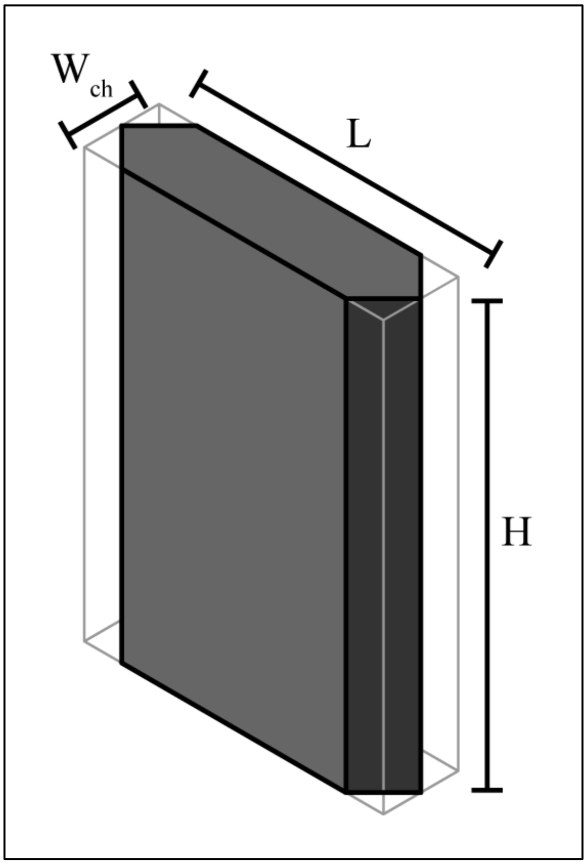

Figure 4.7: ERV overall dimensions

The face velocity and channel height were also equivalent for both designs. The difference of 50 mm overall length compared to the work envelope discussed at the beginning of this chapter was to allow for one inch of insulation at either end of the exchanger in the final design. Figure 4.8a shows a comparison of the sensible and latent effectiveness and pressure drop, while Figure 4.8b shows a comparison of the relative contribution of membrane and air-side resistance to heat and mass transfer for the pin-fin and strip-fin geometry.

Table 4.3: AHRI Rating Conditions

Air Stream		Heating	Cooling
Supply	Dry-bulb, °F	35	95
	Wet-bulb, °F	33	78
Exhaust	Dry-bulb, °F	70	75
	Wet-bulb, °F	58	63

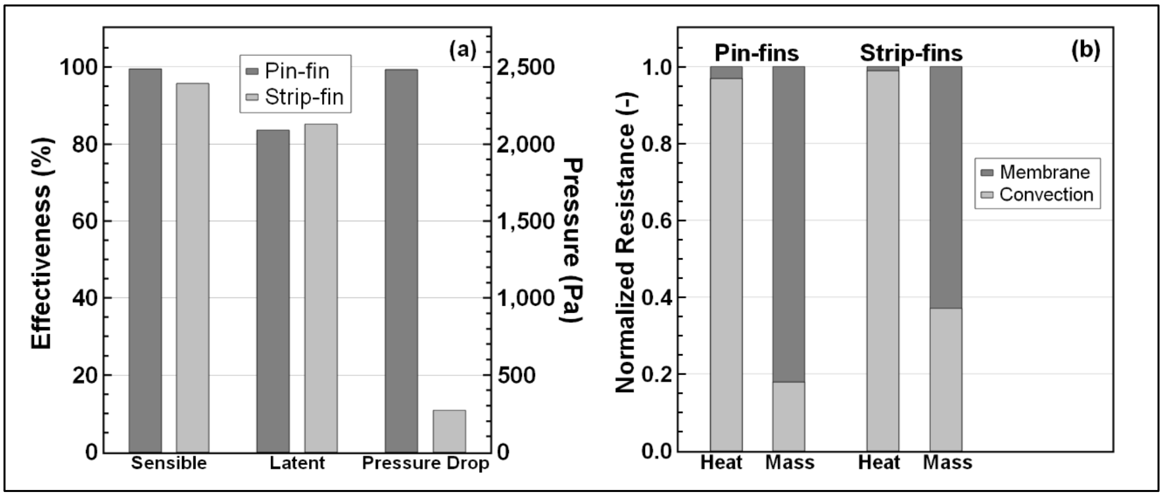

Figure 4.8: ERV (a) performance and (b) heat and mass transfer resistance comparisons for pin-fin and strip-fin geometries

Figure 4.8a shows slightly enhanced performance of the strip-fins for mass transfer while the pin-fin ERV provides enhanced heat transfer. The pin-fins show have much greater pressure drop, to the point that the flow would could likely not be maintained without excessive noise/power consumption/etc.

An increase in mass transfer performance for the pin-fins would be expected since there is (a) increase from 79.4% open area in the strip-fin ERV to 96.2% open area in the pin-fin ERV and (b) the pin-fin has smaller convective resistance than the strip-fin as shown in Figure 11b. However, in addition to increasing fan power requirements, the increased pressure drop of the pin-fin ERV negatively affects the local difference in vapor pressure across the membrane throughout the counterflow heat exchanger core. This in turn reduces the local driving potential for mass transfer in the pin-fin ERV, contributing to the observed performance.

In addition to unacceptable pressure drop performance, the fabrication of a pin-fin internal structure via adhesive dispensing is more difficult than dispensing solid beads to make strip-fins. The control required to properly stop and start dispensing is much more than to dispense continuously. Pin-fins require nearly exclusively start and stopping. Strip-fins, with substantially lower pressure drop for the same hydraulic diameter and a decrease in fabrication difficulty were chosen for further investigation.

4.2.3 Parametric Evaluation of the Strip-fin Geometry

To explore the tradeoffs between heat and mass transfer and pressure drop in a strip-fin ERV, the performance was predicted for the ERV with the fixed *overall* dimensions and membrane properties shown in Table 4.1, equivalent inlet conditions (Table 4.3), and varying channel hydraulic diameter calculated via Eq.(3.5) from Chapter 3. The results are shown in Figure 4.9.

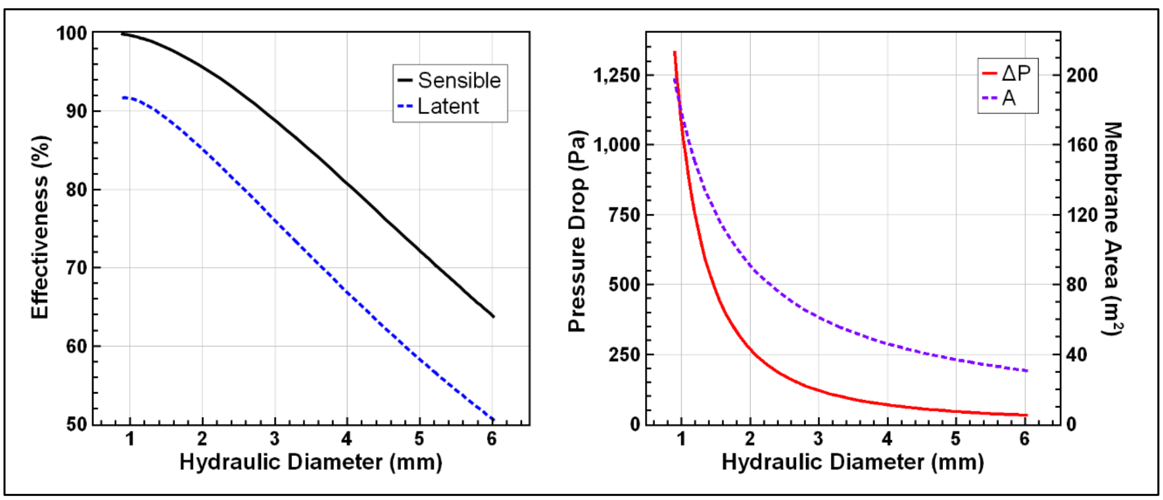

Figure 4.9: (a) Sensible and latent effectiveness (b) and pressure drop and required membrane area of strip-fin ERV at varied hydraulic diameter

Figure 4.9 shows a strip-fin hydraulic diameter of 2 mm satisfies the pressure drop (< 300 Pa), sensible effectiveness and latent effectiveness targets. A hydraulic diameter of 2 mm corresponds to a channel height of 1.25 mm, a strip-fin spacing of 5 mm, and 91.01 m^2 of membrane area.

Figure 4.9 also shows that as the strip-fin hydraulic diameter decreases, the sensible and latent effectiveness, pressure drop, and membrane area (since more membrane can fit in a fixed overall height) all increase. At the same time, since the face area is fixed and the membrane and strip-fin thickness is small, the change in maximum flow velocity in each channel is small. Thus, the change in Reynolds number (379 to 1148) and the related increase in pressure drop is primarily governed by the decreasing hydraulic diameter. The sensible and latent effectiveness increase is due to (a) the increased membrane area and (b) the increase in heat and mass transfer coefficient due to the smaller diffusion length characteristic of the smaller hydraulic diameter. This analysis led to a final study to establish a full scale design using the 1D model.

4.2.4 1D Model Full Scale ERV Design

While the results shown in Figure 4.9 at a hydraulic diameter of 2 mm do satisfy the performance targets, parametric studies can be used to refine the design. Any effort to reduce the number of channels and strip-fins required can reduce overdesign and reduce cost. In the next parametric study, channels will still be added but instead of fixing the overall ERV height, the maximum pressure drop is set equal to the maximum allowable (<= 300 Pa) and the channel height, the overall height, and effectiveness is solved for. This way, the pressure drop criteria is always satisfied and only the effectiveness targets must be found parametrically. A large parametric table is created with the goal of satisfying the effectiveness targets with the fewest number of channels. The number of strip-fins in the headers and the body are selected manually as well to provide duct widths of 4 mm or less. This span length was selected based on simply supported plate theory with an estimated maximum differential pressure across the membrane of 300 Pa near the inlets and outlets. Values from Table 4.4 were assumed for this analysis. The 10% allowable deflection, $\Delta h_{ch,allow}$, is assumed to be a small enough deflection to mitigate the deflection-pressure drop coupling and would not impact the geometric assumptions regarding heat and mass transfer coefficients.

Table 4.4: Membrane deflection assumptions

Variable	Value	Units
$\%\Delta h_{ch,allow}$	10	%
h_{ch}	1.25	mm
E	936	MPa
ν	0.42	-
δ	25	μm
α	1	-

A duct width of 3.57 mm satisfied the criteria in Table 4.4. The decision to use a 4 mm maximum duct width was based on the assumption of applied pre-stress in membrane during fabrication, reducing the deflection. The plate deflection model does not consider pre-stress. Table 4.5 reflects the final dimensions and performance results of the parametric study.

Table 4.5: 1D ERV model parametric study inputs and results

Input Variable	Value	Units	Output Variable	Value	Units
L	700	mm	ε_S	94.20	%
W	175	mm	ε_L	83.01	%
ΔP_e	300	Pa	ΔP_s	287.7	Pa
N	728	-	h_{ch}	1.26	mm
$N_{d,body}$	34	-	H	932	mm
$N_{d,header}$	24	-	$W_{d,body}$	3.85	mm
AR_{st}	1	-	$W_{d,header}$	3.85	mm
δ	25	μm			
D_m	4.3×10^{-7}	$m^2\ s^{-1}$			
k_m	0.0765	$W\ m^{-1}\ K^{-1}$			

An ERV characterized by the results shown in Table 4.5 theoretically satisfies the performance targets without using more membrane layers and strip-fins than required and fits within the desired work envelope.

4.2.5 1D and 2D Model Comparison

While the results of the 1D parametric study are valuable for rapid design generation and performance prediction, more can be learned about the effect of local heat and mass transfer with a 2D model. In particular, the non-uniform membrane mass transfer resistance model is best utilized in 2D since temperature and humidity vary along the length and width of the exchanger. The development of a 2D model also enables the ability to view the distribution of heat and mass transfer within a channel. Before incorporating the variable membrane resistance function, a comparison between the 1D and 2D model is made assuming all the same input parameters from Table 4.5. This provides confidence in both models in addition to the literature comparison studies in Chapter 3. Since the exhaust stream pressure drop is set equal to 300 Pa and the number of channels is 728 for both models, the channel height is solved to satisfy the pressure drop. This is why the channel height, overall height, and duct widths are not equal for both the 1D and 2D models (Table 4.6).

Table 4.6: Comparison of the 1D and 2D performance predictions

Output Variable	1D Value	2D Value	Units
ε_S	94.20	93.97	%
ε_L	83.01	82.94	%
ΔP_s	287.7	299.6	Pa
h_{ch}	1.26	1.23	mm
H	932	916	mm
$W_{d,body}$	3.85	3.88	mm
$W_{d,header}$	3.85	3.87	mm

The difference in both the sensible and latent effectiveness are negligible. The difference of 11.9 Pa in the fresh air stream pressure drop is most likely due to the use of inlet property values to calculate the pressure drop in the 2D model. In the 1D model, the segment pressure drop is calculated using the state properties at each segment. Differences in ERV dimensions are a direct results of the difference in pressure drop calculation.

4.2.6 Final Full Scale Design

Two updates to the model were important to establishing a final ERV design using the 2D model. First, the constant mass transfer resistance $R_{m,MT} = \delta/D_m$ was changed to a variable resistance which is a function of temperature and relative humidity. The details of this implementation are further discussed in Section 5.1.2. The second update is the deflection model described in Section 3.1.1.6. Instead of assuming an acceptable strip-fin spacing, the percent deflection in the header and the body is calculated and used as a guide to the number of required strip-fins. The inputs and results of the 2D parametric study are shown in Table 4.7.

Table 4.7: 2D ERV model parametric study inputs and results

Input Variable	Value	Units	Output Variable	Value	Units
L	700	mm	ε_S	94.71	%
W	175	mm	ε_L	83.01	%
ΔP_e	300	Pa	ΔP_s	299.6	Pa
N	704	-	h_{ch}	1.185	mm
$N_{d,body}$	24	-	H	852	mm
$N_{d,header}$	23	-	$W_{d,body}$	6.06	mm
AR_{st}	1	-	$W_{d,header}$	4.14	mm
δ	25	µm	$\Delta h_{ch,body}$	9.6	%
k_m	0.0765	$W\ m^{-1}\ K^{-1}$	$\Delta h_{ch,header}$	9.28	%

4.2.7 1D vs 2D Full Scale ERV Designs

The thin film deflection model predicts smaller deflections than the supported plate model under similar conditions. Therefore, fewer strip-fins are required and larger duct widths are possible while remaining under the desired 10% deflection maximum. Fewer strip-fins in the 2D model ERV design compared to the 1D model ERV design improves the open area ratio from 74.85% to 82.21%. The average membrane mass transfer resistance in the 1D model is 58.14 s m^{-1} vs the 63.13 s m^{-1} in the 2D model. The increased open area reduced the number of layers despite the increase in predicted average membrane mass transfer resistance. Another benefit of the reduced number of strip-fins is the reduction in overall size of the ERV. The overall height of the exchanger is reduced by 80 mm.

4.3 Prototype Exchanger Design and Fabrication

A prototype was designed and fabricated to better understand the new ERV manufacturing process, inform the network resistance model inputs, and validate the model results.

4.3.1 Preliminary Prototype Design

The design of the prototype ERV was most greatly influenced by the 1D model findings since the fabrication process was initiated before the development of a 2D model. The footprint of the dispensing (Figure 4.10) also played a large role in the selection of the prototype overall dimensions.

Figure 4.10: Dispensing unit

The footprint allowed for a nominal length of the prototype to be 250 mm. The width-to-length ratio of the full scale design was 0.25 so the prototype was given the same ratio making the nominal width 62.5 mm. The test loop was designed to flow between 0.5 and 1.5 CFM of air through both sides of the exchanger. The baseline flow rate was 1 CFM. The number of strip-fins was selected to maintain a duct width of less than 4 mm as was the case in the 1D model. For fabrication purposes, it was important the channel height closely resemble that determined in the 1D full scale analysis, 1.26 mm.

The final ERV design parameter to decide was the number of channels. From a modeling perspective, choosing the number of channels providing a bulk velocity in the channels similar to the velocities seen in the full scale analysis would be preferable. Similar velocities would provide similar convective heat and mass transfer coefficients to the full scale thus making the prototype results more representative of the predicted full scale performance. The bulk velocities observed in the full scale body and header regions model are 2.36 and 3.32 m s^{-1} respectively. This would require 8 total channels (4 for each stream) providing body and header bulk velocities of 2.03 and 2.94 m s^{-1} respectively for the prototype. However, from a manufacturing perspective, repeatability of the manufacturing technique is also very important. The project team decided 8 channels did not provide sufficient evidence of fabrication repeatability and the prototype would consist of 20 total channels. While this does greatly reduce the bulk velocity in the body and headers (0.81 and 1.17 m s^{-1}) the model has been validated against many flow rates as shown in Chapter 3. Additionally, using 20 channels does bring the predicted latent effectiveness above the targeted 83% from the 66.5% predicted for an 8 channel prototype. The preliminary prototype design parameters and performance predictions from the 1D model are shown in Table 4.8.

Table 4.8: Preliminary prototype design parameters and predicted performance

Input Variable	Value	Units	Output Variable	Value	Units
L	250	mm	ε_S	94.43	%
W	62.5	mm	ε_L	84.32	%
h_{ch}	1.26	mm	ΔP_s	35.5	Pa
N	20	-	ΔP_e	37.1	Pa
$N_{d,body}$	12	-	H	25.73	mm
$N_{d,header}$	9	-	$W_{d,body}$	3.84	mm
AR_{st}	1	-	$W_{d,header}$	3.51	mm
δ	25	µm			
D_m	4.3×10^{-7}	$m^2\ s^{-1}$			
k_m	0.0765	$W\ m^{-1}\ K^{-1}$			

4.3.2 Fabrication Process Challenges

While there are many benefits to the manufacturing process, there were several difficulties to overcome before fabricating a prototype ERV. Controlling the dispensing and bonding process to obtain repeatable desired adhesive dimensions can be challenging. The fabrication hurdles impacted the prototype design after the preliminary design was established. This section will discuss some of the challenges regarding fabrication of the prototype ERV.

The adhesive beads composing the strip-fins need to cover as little membrane area as possible while supporting the membrane at the desired channel height. The area covered by adhesive will transport no moisture and little heat since the strip-fins have low conductivity. The channel height must be large enough to keep within the allowable pressure drop. Adhesives that slump too much after dispense are not good for supporting the membrane. The strip-fins become very wide and short, reducing open membrane area and increasing pressure drop. While bonding the membrane on top of the adhesive pattern the adhesive lines are deformed such that they increase in width, covering more membrane area. One solution to this problem is printing 2 beads on top of each other or "double printing" shown in Figure 4.11. It was common for the start of the bead to be lacking in adhesive and the end to have too much. If the beads are printed on top of one another in counter directions, the ends can compensate for each other, making the overall height and shape of the bead more consistent along the length.

Figure 4.11: Double printed adhesive strips in a 5 channel sample

Double printing of beads provides taller channels while covering less membrane area than a larger single strip would. However, the dispensing time per channel approximately doubles, increasing manufacturing cost and working against the adhesive curing time. The adhesive curing time constrains the time taken to dispense the pattern and adhere the next membrane. If too much time is taken for dispensing, it may be an inadequate bond making the exchanger channels unsealed and less supported. While understanding the disadvantages of the double printing technique, it was decided this would produce the required dimensions and was used to fabricate the prototype exchanger.

The lack of flow control can also leave wisps of adhesive on the membrane as seen in Figure 4.12. This problem can be mitigated to some extent by cleaning the dispenser nozzle of any cured adhesive between long pauses and adjusting the dispense delay times.

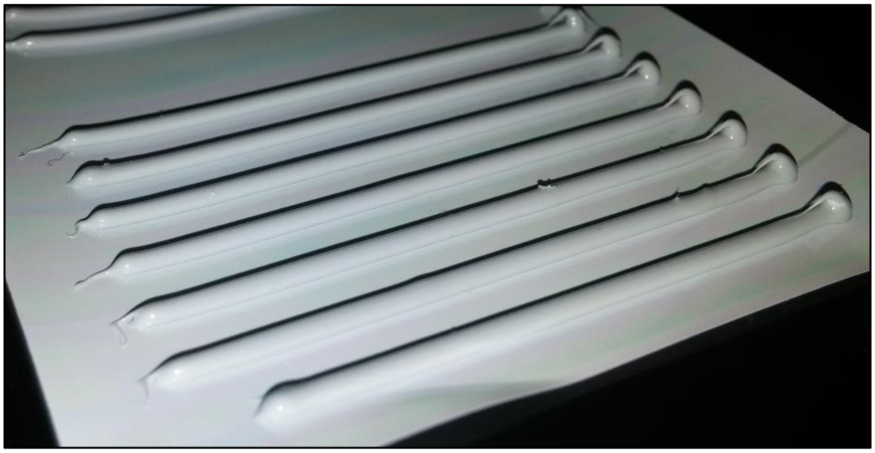

Figure 4.12: Sample dispense test – end issues

Backtracking also prevents adhesive from bonding in the intended transport area. At the end of a bead, the nozzle can move backwards for a short distance giving the adhesive a chance to detach from the nozzle and landing on the bead itself.

In some instances adhesive beads will not be straight throughout the bead length. This often is a dispense nozzle gap height issue. If the nozzle is too far from the membrane, the adhesive can curl as it exits the nozzle before contacting the membrane creating a ripple as shown in Figure 4.13. A lack of parallelism leading to variation in the gap height created ripples in certain adhesive beads while fabricating the prototype. The solutions to these fabrication challenges greatly impacted the design of the prototype ERV.

Figure 4.13: Sample dispense test – bead ripples and wisps

4.3.3 Final Prototype Design

The prototype design was modified to account for the fabrication difficulties mentioned in the previous section. Other changes were made for the purposes of easier installation of the prototype into the testing apparatus. First, because of a tendency for adhesive beads to ripple due to an unsolved parallelism issue, a 4 mm margin was created around the edges of the outside adhesive beads. The number of strip-fins in both the body and headers were thus reduced from 13 and 10 to 12 and 9 respectively. This kept the duct widths from becoming too small. Installing the prototype into a test apparatus required the fabrication of sealed ducting at the inlets and outlets of the exchanger. Tabs were constructed by incorporating them in the dispense pattern. These tabs could then be adhered to the ducting. A schematic of the final prototype support structure design is shown in Figure 4.14. The parameters and predicted performance values per the 1D model are listed in Table 4.9.

Figure 4.14: Final prototype strip-fin internal support dispense pattern design

Table 4.9: Final prototype design parameters and predicted performance using 1D model

Input Variable	Value	Units	Output Variable	Value	Units
L	250	mm	ε_S	93.02	%
W	62.5	mm	ε_L	81.37	%
h_{ch}	1.26	mm	ΔP_s	40.27	Pa
N	20	-	ΔP_e	41.95	Pa
$N_{d,body}$	11	-	H	25.73	mm
$N_{d,header}$	8	-	$W_{d,body}$	3.58	mm
AR_{st}	1	-	$W_{d,header}$	3.40	mm
δ	25	μm			
D_m	4.3×10^{-7}	$m^2\ s^{-1}$			
k_m	0.0765	$W\ m^{-1}\ K^{-1}$			
W_{marg}	4	mm			

In Figure 4.15, the final channel is fabricated on the prototype ERV. Figure 4.16 shows the prototype immediately after fabrication.

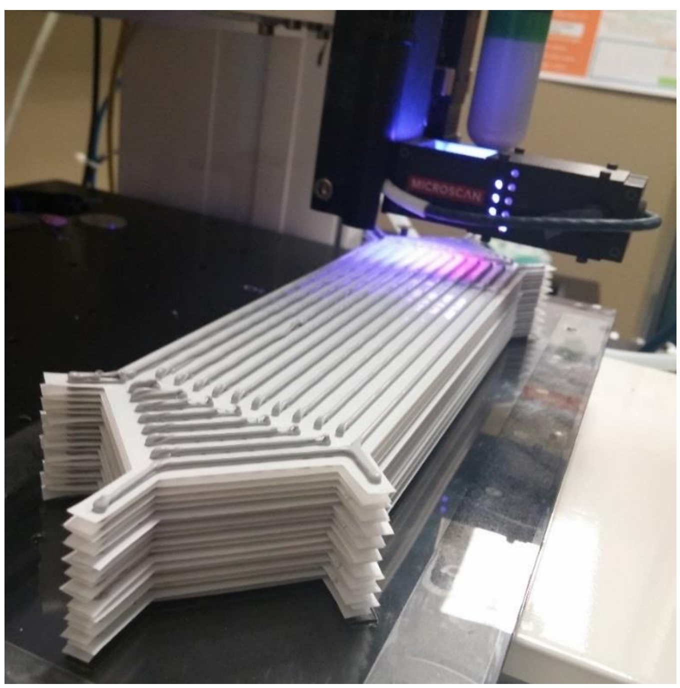

Figure 4.15: Final stages of prototype fabrication

Figure 4.16: Prototype

4.4 Summary

The 1D model was used to generate a preliminary design for a prototype ERV with a proportional footprint. Several fabrication challenges were overcome to fabricate the prototype ERV. This ERV demonstrated the viability of an advanced manufacturing technique and a prototype with which to perform performance measurements on. The measurements can be used to further validate the models as discussed in Chapter 5.

Chapter 5: Model Evaluation

In this chapter, results of the developed 1D and 2D resistance network heat and mass transfer and pressure drop models will be evaluated. Investigations into several ERV design aspects will be conducted parametrically. First data from the prototype ERV will be compared to the model results. These experiments were conducted at Oregon State University by Chuankai Song under the direction of Dr. Hailei Wang. The second section will consider how uncertainty in specific model inputs can affect the predicted performance. The third section will briefly compare the 1D and 2D model results for the same model inputs. The fourth section will discuss the effects of membrane diffusivity and hydraulic diameter on the performance using parametric studies conducted with the 1D model. In the fifth section, the 2D model will be use to predict ERV performance in different climates in the United States. Finally, the 2D model will be used for a more detailed look into the heat and mass transfer through the membrane as it changes along the channel length and width.

5.1 Comparison of Experimental Data and Predicted Performance

The prototype ERV design specified in Chapter 4 was tested experimentally at the six testing conditions shown in Table 5.1. These conditions were chosen in an effort to evaluate the performance at different flowrates and supply stream relative humidity.

Table 5.1: Prototype ERV test conditions

Test	$\dot{V}_s$ (L min^{-1})	$\dot{V}_e$ (L min^{-1})	T_{si} (°C)	T_{ei} (°C)	φ_{si} (%)	φ_{ei} (%)
1	28.35	28.3	35.33	25.18	59.1	41.72
2	20.97	21.225	35.04	24.98	58.84	41.37
3	35.39	35.375	35.2	25.04	59.16	41.19
4	14.01	14.15	35.17	25.07	58.98	41.11
5	28.39	28.3	35.22	25.15	69.9	41.9
6	28.27	28.3	35.25	25.14	49.97	41.25

5.1.1 Prototype Pressure Drop

The dimensional parameters used for the prototype model are shown in Table 5.2. The measured pressure drop data are provided in Table 2. These measured values are compared to the pressure drop predicted by both the 1D and 2D models as shown in Figure 5.1. The 1D pressure drop model is particularly accurate in predicting the supply stream pressure drop (Figure 5.1a) with an AAD of 3.1%. However, the AAD is 13% for the exhaust air pressure drop. While percentage difference is high, the largest absolute difference in predicted and measured pressure drop is less than 4 Pa and the uncertainty is 1.49 Pa. This is the total uncertainty including the design stage uncertainty of the differential pressure sensor and data acquisition system as well as the random uncertainty. Further details regarding the experimental data collection, sensor calibrations, and uncertainty calculations are included in the work done by Chuankai Song at Oregon State University (Song, 2017).

Table 5.2: Prototype ERV dimensions

Variable	Value	Units	Variable	Value	Units
L	250	mm	H	31.76	mm
W	62.5	mm	$W_{d,body}$	3.98	mm
h_{ch}	1.562	mm	$W_{d,header}$	3.77	mm
N	20	-	δ	25	μm
$N_{d,body}$	11	-	k_m	0.0765	$W\ m^{-1}\ K^{-1}$
$N_{d,header}$	8	-	W_{marg}	4	mm
AR_{st}	1	-			

For the 2D model, the AAD for the supply and exhaust pressure drop values are 10.36% and 1.66% respectively. A primary difference between the 1D and 2D models is that property values for air were determined at inlet fluid states in the 2D model, rather than local properties. However, as Figure 5.1 shows, all 2D predicted values for the exhaust air stream were within experimental uncertainty, suggesting this is a reasonable assumption.

Table 5.3: Measured experimental pressure drop

Test	ΔP_s (Pa)	ΔP_e (Pa)	Test	ΔP_s (Pa)	ΔP_e (Pa)
1	29.47	26.4	4	14.5	12.6
2	21.49	20.1	5	30.84	26.4
3	36.97	34.4	6	29.27	26.4

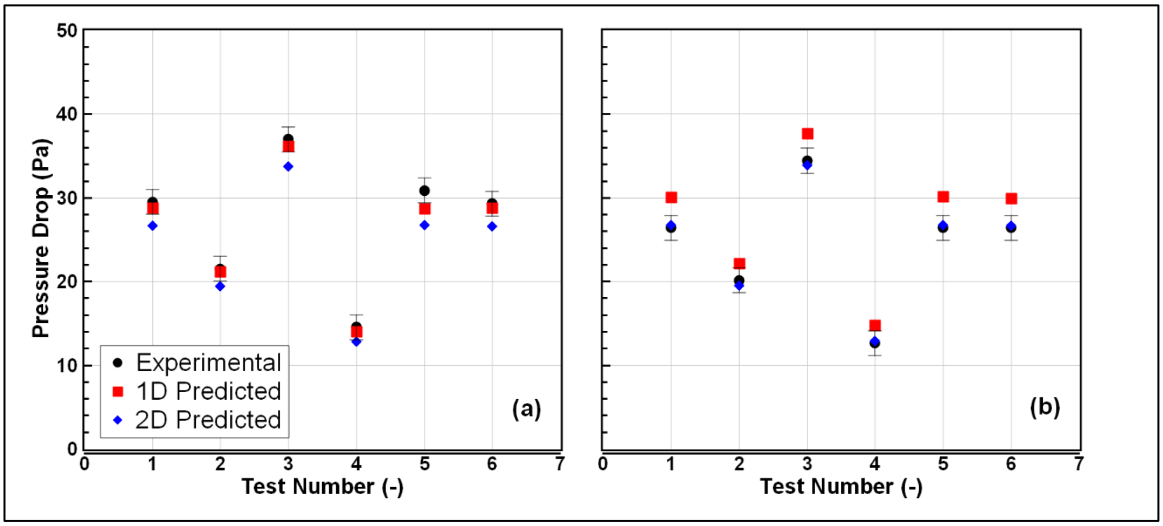

Figure 5.1: (a) Supply and (b) exhaust air stream experimental and predicted prototype ERV pressure drop

It is worth noting the uncertainty of the channel height was not incorporated in either the 1D or 2D prototype model since it was difficult to characterize without many fabrication tests or destructive testing of the prototype. Variation in this parameter can change the pressure drop prediction significantly.

5.1.2 Prototype Effectiveness

The 2D model is capable of incorporating a local membrane mass transfer resistance value that is a function of temperature and relative humidity. Membrane mass transfer resistance ($R_{m,MT}$) values at three temperatures and six humidity ratios for the membrane used in the prototype ERV were provided by the vendor. Only two of the temperatures were applicable for the current study. A computationally efficient way to incorporate this data was to apply a quartic polynomial function of membrane mass transfer as a function of the supply side membrane surface humidity (Eq.(5.1)) for both given temperatures and linearly interpolate using the supply side membrane surface temperature.

$$R_{m,MT} = a_0 + a_1\phi_{sw} + a_2\phi_{sw}^2 + a_3\phi_{sw}^3 + a_4\phi_{sw}^4 \tag{5.1}$$

The measured prototype effectiveness values are provided in Table 5.4. In Figure 5.2, the measured sensible and latent effectiveness are compared to that predicted by the 1D and 2D resistance network models. As is the case for the pressure drop measurements, the total uncertainty is comprised of the design stage uncertainty and the random uncertainty. Included in the design stage uncertainty is the uncertainty of each temperature and humidity sensor as well as the volumetric flow meters. Further detail of the experimental data is included in the work of Song (2017). The AAD of the sensible effectiveness for the 1D and 2D models were 5.86% and 6.16% respectively. The sensible effectiveness was generally underpredicted by both models. This may partially be due to the conservative assumption that the adhesive strip-fins are non-conducting, and that the area under the strip-fin does not contribute to the heat transfer area. In reality, the adhesive strip-fins will add some heat transfer area even though the adhesive conductivity may be small compared to conventional metal heat exchanger fins.

Table 5.4: Measured experimental effectiveness

Test	ε_S (%)	ε_L (%)	Test	ε_S (%)	ε_L (%)
1	97.71	24.43	4	97.78	33.45
2	97.56	27.83	5	86.33	27.09
3	95.23	23.29	6	99.81	24.35

The very large differences in predicted and measured latent effectiveness seen in Figure 5.2b (AAD for 1D and 2D models are 206% and 196% respectively) can most probably be attributed to a problem in the manufacturing process. After the fabrication of the prototype ERV, it was found the adhesive curing process may have increased the membrane mass transfer resistance by filling many of the membrane pores with residual material from the adhesive. This was confirmed by visual inspection by the membrane vendor to be a possible cause. However, the exact percentage of membrane area blocked could not be quantified in the experimental study.

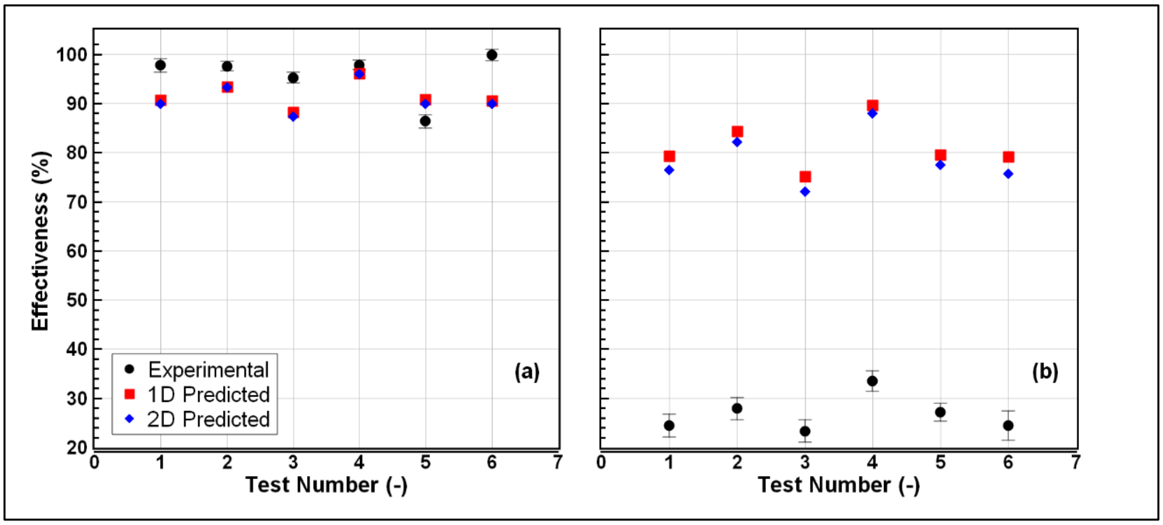

Figure 5.2: (a) Sensible and (b) latent experimental and predicted prototype ERV effectiveness

The model was used to attempt to predict what percentage of membrane area was blocked for mass transfer. The latent effectiveness was predicted again assuming 10% of the membrane was available for mass transfer and is shown in Figure 5.3. It is assumed the open and covered number of membrane pores is consistent and uniform throughout the entire ERV for all test conditions. The AAD of the latent effectiveness is 8.46% for the adjusted membrane area. Since the general trend of both the experimental and predicted effectiveness values agree, the assumption the predicted membrane diffusivity was affected during fabrication appears to be valid.

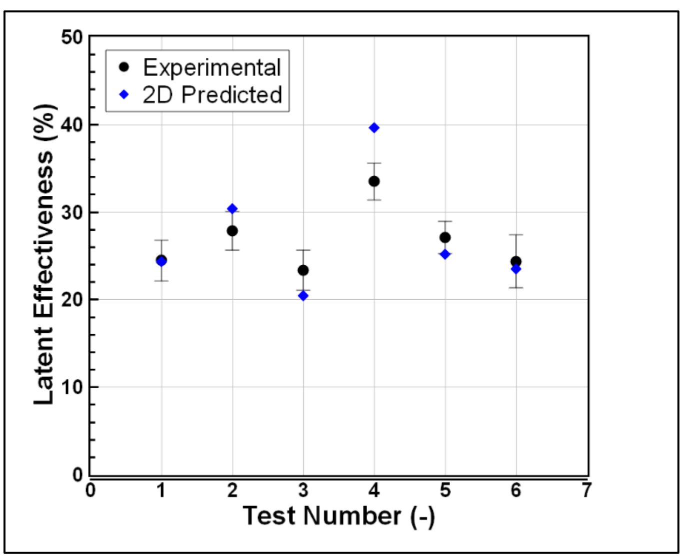

Figure 5.3: Predicted and experimental latent effectiveness – adjusted open membrane area

The uncertainty of the channel height was not incorporated in this study but could have a large impact on the predicted effectiveness. The channel height along with other model input parameters will be evaluated more generally in terms of their contribution to the total uncertainty of the predicted effectiveness in the following section.

5.2 Model Uncertainty

The resistance network model is only as accurate as the underlying inputs for dimensions, membrane properties, and heat and mass transfer correlations. To assess the relative importance of different model inputs, the 1D model for the quasi-counterflow case was evaluated at different air volumetric flow rates with uncertainties assigned to model inputs as shown in Table 5.5. Conservative uncertainty for membrane diffusivity and calculated Nusselt number were chosen, while uncertainties in dimensions and inlet conditions were consistent with what might be expected from an experimental setup.

Table 5.5: Assumed uncertainty of model input parameters

Model Input	Uncertainty
Nusselt Number (calculated)	±25%
h_{ch}	±0.5 mm (±12.5%)
D_m	±20%
ω	±2%
T_{inlet} (dry bulb)	±1°C

The resulting effect of the uncertainty of all parameters in Table 5.5 on sensible and latent effectiveness as a function of flow rate is shown in Figure 5.4 compared with the quasi-counterflow data of Zhang (2010). The average percent uncertainty for all flow rates was ±6.2% for sensible effectiveness and ±5.5% for latent effectiveness. Figure 5.5 shows the relative contribution of the uncertainty of each input parameter to the overall uncertainty at three different volumetric flow rates.

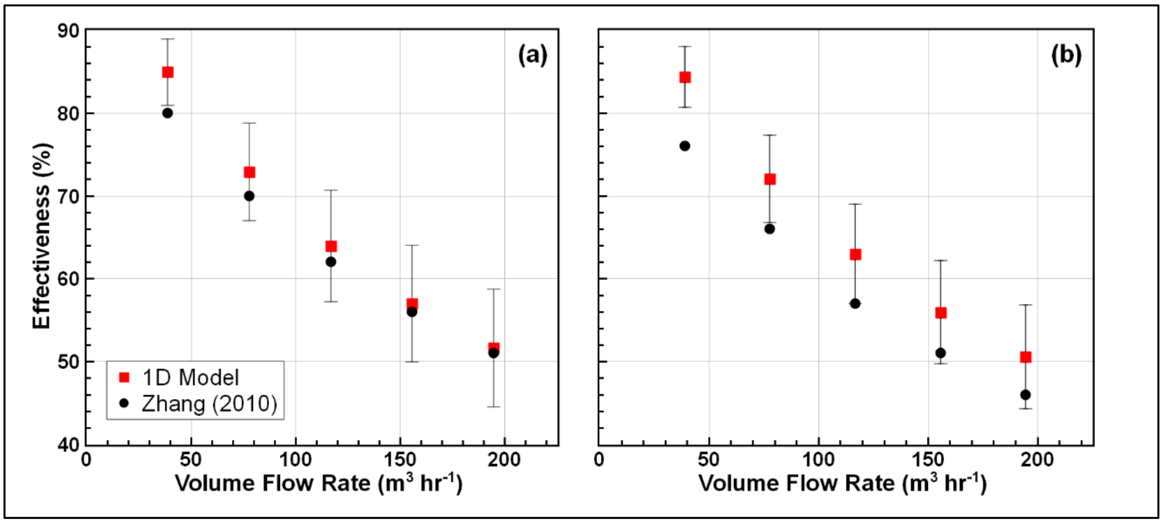

Figure 5.4: 1D quasi-counterflow (a) sensible and (b) latent effectiveness at various flow rates with model uncertainty

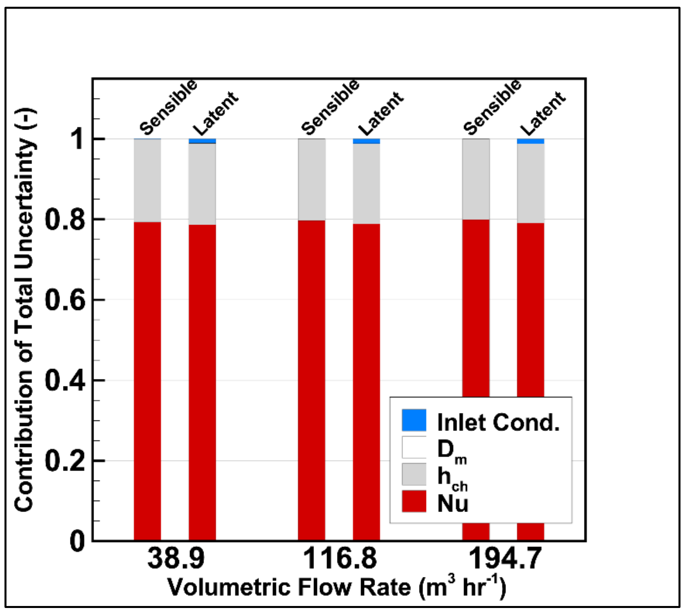

Figure 5.5: Relative contribution of model input parameters to overall uncertainty

As expected, the relatively conservative uncertainty of ±25% in the Nusselt number correlation is the greatest contributor to uncertainty. This was followed by the contribution of geometric uncertainty in channel height. For the latent effectiveness, there was some contribution of the uncertainty in the inlet conditions (dry bulb temperature and humidity ratio), but little effect of a ±20% uncertainty in the membrane effective diffusivity. This shows the convective resistance dominates the heat and mass transfer process in this system architecture. The uncertainties assigned in Table 5.5 represent conservative values and illustrate the impact of underlying inputs on the predictive performance of the heat and mass exchanger model. Despite this, the simpler network model offers reasonable overall agreement with the more complicated CFD analysis, suggesting it can be used as a lower cost and rapid first design and optimization tool.

5.3 Parametric Evaluation of Full Scale ERV Performance

Using the 1D model, the relative contribution of the air-side convective and membrane resistances were evaluated as a function of strip-fin hydraulic diameter (with inlet conditions shown in Table 5.6 and fixed overall ERV dimensions and membrane properties from Table 5.7). The results are shown in Figure 5.6. The conductive heat transfer resistance contributed by the membrane was negligible compared to the convective resistance for all channel heights evaluated, while diffusive resistance due to the membrane dominated the total mass transfer resistance at small channel heights. The membrane resistance became more comparable to the convective mass transfer resistance as channel height increased. At the selected hydraulic diameter of 2 mm, the air-side accounts for 37% of the mass transfer resistance. Therefore, as membrane technology improves, the heat and mass transfer resistances in the air-side will increasingly become the limiting factors in membrane based ERVs if channel sizes are not properly designed.

Table 5.6: AHRI rating conditions

Air Stream		Heating	Cooling
Supply	Dry-bulb, °F	35	95
	Wet-bulb, °F	33	78
Exhaust	Dry-bulb, °F	70	75
	Wet-bulb, °F	58	63

Table 5.7: ERV design parameters

Variable	Value	Unit	Variable	Value	Unit
L	750	mm	D_m	4.3×10^{-7}	$m^2\ s^{-1}$
W_{ch}	175	mm	δ	25	μm
H	1000	mm	AR_{st}	1	-
k_m	0.0765	$W\ m^{-1}\ K^{-1}$	AR_d	4	-

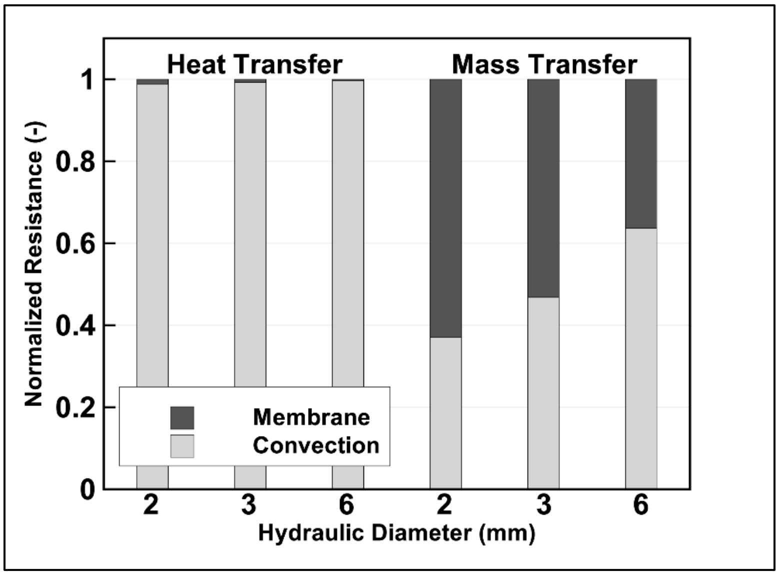

Figure 5.6: Heat and mass transfer resistance of ERV at several hydraulic diameters

Literature values for effective diffusivity can vary by orders of magnitude depending on membrane material, construction techniques, and selectivity for other species (Metz *et al.* 2005; Yang *et al.* 2015). For the ERV design parameters in Table 5.7, with a hydraulic diameter of 2 mm, the latent effectiveness of the ERV and the relative contribution of air-side and membrane resistance to mass transfer is compiled in Figure 5.7 for effective diffusivities from 10^{-9} to 10^{-4} $m^2\ s^{-1}$ and the inlet conditions shown in Table 5.6. The range of diffusivities were chosen to be similar to those evaluated by Yaici *et al.* (2013).

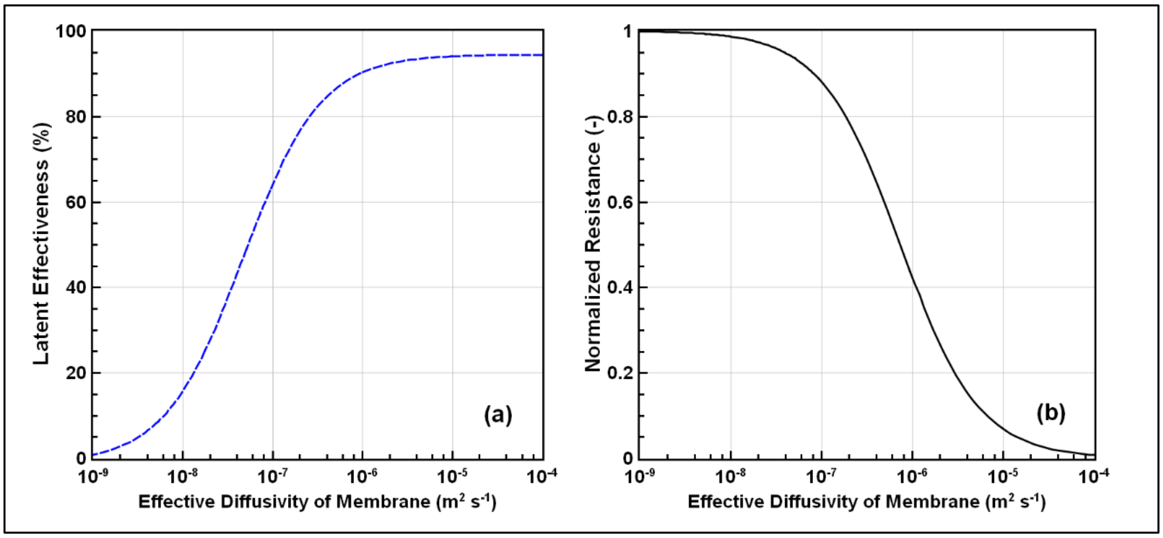

Figure 5.7: (a) Latent effectiveness and (b) normalized mass transfer resistance contribution of membrane for different diffusivities.

The latent effectiveness for the exchanger is shown in Figure 8a. The effectiveness increases from 90.2% to 94.4% for membrane diffusivities ranging from 10^{-6} to 10^{-4} $m^2\ s^{-1}$. This suggests high convective resistances prevent highly permeable membranes from significantly improving ERV performance. The membrane accounts for 42.5% of the total mass transfer resistance at 10^{-6} $m^2\ s^{-1}$ and 0.73% at 10^{-4} $m^2\ s^{-1}$. The steep decline in resistance contributed by the membrane as the diffusivity increases further suggests the important role of convective mass transfer in improving the effectiveness of ERVs.

5.4 Comparison of 1D and 2D Models

While the 1D model does predict ERV performance quite well, the 2D model includes spatially varying temperatures and humidity as well as more accurate membrane mass transfer inputs. It is important to investigate the difference in predicted performance outside of the literature comparison studies seen in Chapter 3 to see the assess the utility of using a more complicated model. Both the 1D and 2D resistance network models were used to predict the performance of the final full scale ERV design (Table 5.8) based on the 2D model results.

Table 5.8: Full scale design parameters based on 2D model

Variable	Value	Unit	Variable	Value	Unit
W	175	mm	N	704	-
L	700	mm	$N_{d,body}$	24	-
H	852	mm	$N_{d,headr}$	23	-
h_{ch}	1.185	mm	AR_{st}	1	-
$W_{d,body}$	6.06	mm	δ	25	µm
$W_{d,header}$	4.14	mm			

The 2D model predicted a slightly lower sensible and latent effectiveness, of 0.36 and 1.18 percentage points difference respectively. This behavior is reversed from what was seen in Section 3.2.2 where the 2D model predicted higher effectiveness than the 1D model. The main difference here is the difference in membrane resistance. The comparison made in Section 3.2.2 used a constant membrane resistance for both models. In this study, the 2D model incorporates the variable resistance function (Eq.(5.1)) while the 1D model remains the same. The pressure drop predicted by the 2D model is 0.22% and 4.44% higher for the supply and exhaust respectively. In Section 5.1.1, the pressure drop predicted by the 1D model was higher than that of the 2D model. The reverse is seen in Figure 5.8.

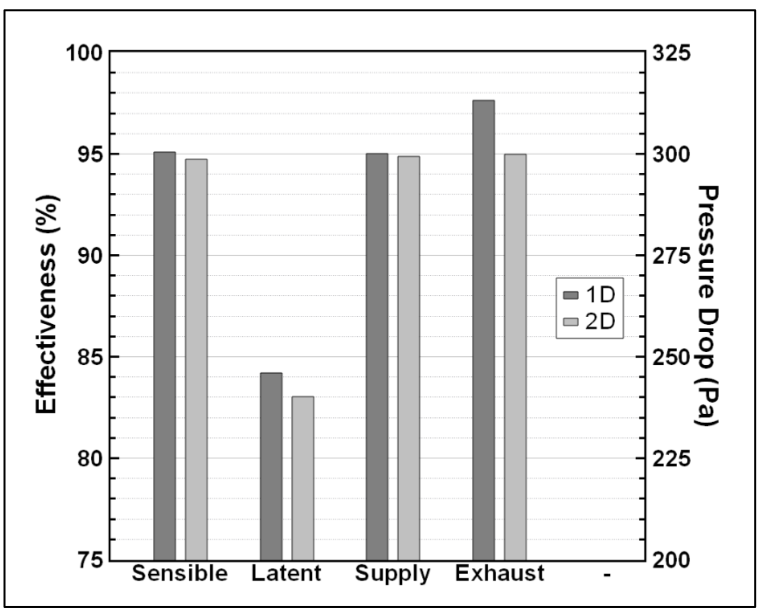

Figure 5.8: 1D and 2D performance predictions of full scale ERV design

This may have to do with the fluid property assumptions made in the 2D model. The bulk velocity in the headers and body of the 2D full scale ERV model are 3.56 m s^{-1} and 2.36 m s^{-1} respectively while the bulk velocity in the headers and body for the 2D prototype ERV model at test case 1 are 1.37 m s^{-1} and 0.85 m s^{-1}. This large difference in velocity may contribute to the apparent inconsistency in the predicted pressure drop in the two models. The effect of assuming inlet fluid properties in the 2D model may be larger in the full scale ERV since the pressure drop is proportional to the velocity squared. The differences in pressure drop are not large enough to undermine the benefits of a 2D model able to utilize variable membrane property data.

5.5 Full Scale ERV Effectiveness in Various Climates

The performance targets of the ERV design must be considered at more than the AHRI rating conditions in Table 7. The device must perform in various climates to be a marketable product. The exhaust (indoor) conditions were held constant at the AHRI rating conditions of $T_{e,db}$ = 75 °F and $T_{e,wb}$ = 63 °F corresponding to $T_{e,db}$ = 23.9 °C and ω_e = 9.53 g kg^{-1}. The supply conditions were set to the values corresponding to the locations specified in Table 5.9 from the 2017 ASHRAE Handbook (ASHRAE, 2017). These dry-bulb temperature and humidity ratio values correspond to annual dehumidification design conditions in which there is a 0.4% annual cumulative frequency of occurrence. This handbook also provides condition values at 1% and 2% annual cumulative frequency of occurrence. A 0.4% annual cumulative frequency of occurrence will provide more extreme humidity conditions than that of the 1% or 2% values. For dehumidification design, these condition values correspond to peak humidity ratios when dehumidification loads are high. The resulting sensible and latent effectiveness for each climate calculated using the 2D model are shown in Figure 5.9.

Table 5.9: ASHRAE dehumidification design conditions in several U.S. cities

Location	T_{db} (°C)	ω (g kg^{-1})	Location	T_{db} (°C)	ω (g kg^{-1})
Juneau, AK	16.3	10	Honolulu, HI	27.2	18.7
Missoula, MT	20.2	11.7	Atlanta, GA	27.3	19.3
Portland, OR	24	12.4	Miami, FL	28.6	21.1
Pittsburgh, PA	26.5	17.8			

The ERV was predicted to perform consistently over various climates considering the maximum difference in sensible and latent effectiveness between any two climates is 1.34% and 4.34% respectively. The latent effectiveness predicted for the conditions in Juneau, AK is particularly high. This may be because the both the indoor and outdoor humidities are so close in magnitude, the denominator of the latent effectiveness equation becomes small, increasing the latent effectiveness. The conditions corresponding to both Juneau, AK and Missoula, MT are such that the supply air is being heated and dehumidified by the exhaust air. For all other locations, the supply air is cooled and dehumidified by the exhaust air. This shows a particularly versatility of the ERV device. One component can be used in many locations and seasons to reduce the energy required to ventilate a building. Many more traditional HVAC components are built for only one or one combination of heating, cooling, dehumidification, and humidification. The ERV has potential to provide any combination of these. Of course, if the outside air conditions are preferred to the inside air conditions, the ERV could be bypassed.

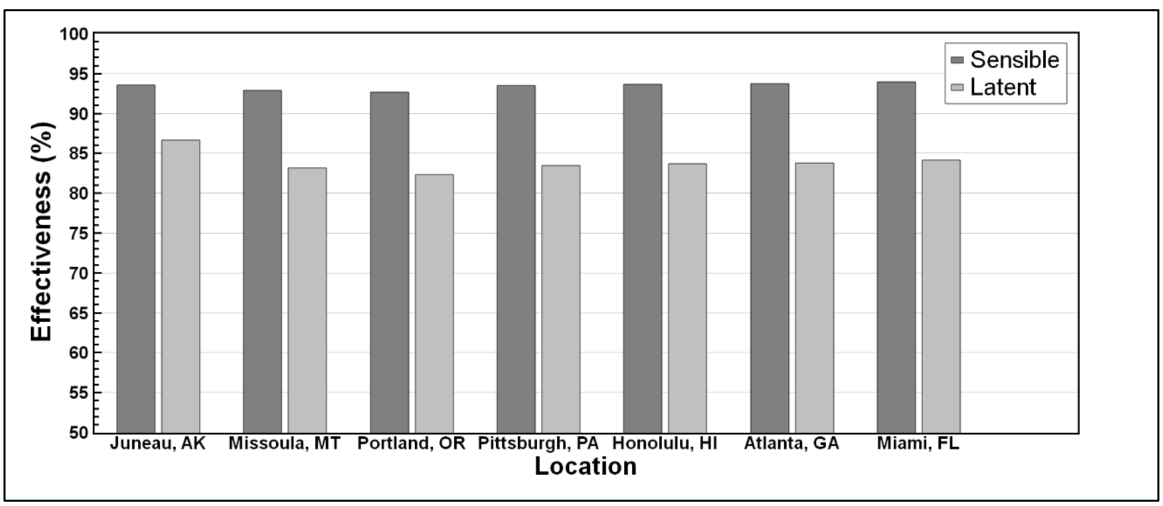

Figure 5.9: Sensible and latent effectiveness of ERV in several locations

5.6 Heat and Mass Transfer Across ERV Membrane Surface

The 2D resistance network model provides spatial heat and mass transfer data across a membrane surface. This data can inform decisions regarding internal support structure and flow path design for further ERV design improvement. To show the potential impact of the inlet conditions on heat and mass transfer, two sets of inlet conditions were used. First the AHRI rating conditions were used. Then inlet conditions with a larger difference in relative humidity were used. The inlet conditions are shown in Table 5.10.

Table 5.10: AHRI and new inlet conditions

Conditions	Air Stream	T_{db} (°F)	T_{wb} (°F)	φ (%)	ω (g kg^{-1})
AHRI Rating Conditions	Supply	95	78	47.27	16.77
	Exhaust	75	63	51.59	9.53
New Inlet Conditions	Supply	95	88	75.92	27.38
	Exhaust	75	55	25.31	4.64

According to the membrane resistance property data received from the vendor, the membrane resistance reduces with an increase in relative humidity at the membrane surface. The membrane resistance across a membrane layer is shown in Figure 5.11. The inlet and outlet routing is shown in Figure 5.10. Since the relative humidity is lower at the supply inlet for the AHRI rating conditions, the membrane resistance is higher in the left header even though the absolute humidity is higher at this inlet. When the relative humidity is changed by applying the new inlet conditions, the area of highest membrane resistance switches to the right header, where a relative humidity of 25.31% is entering the exchanger.

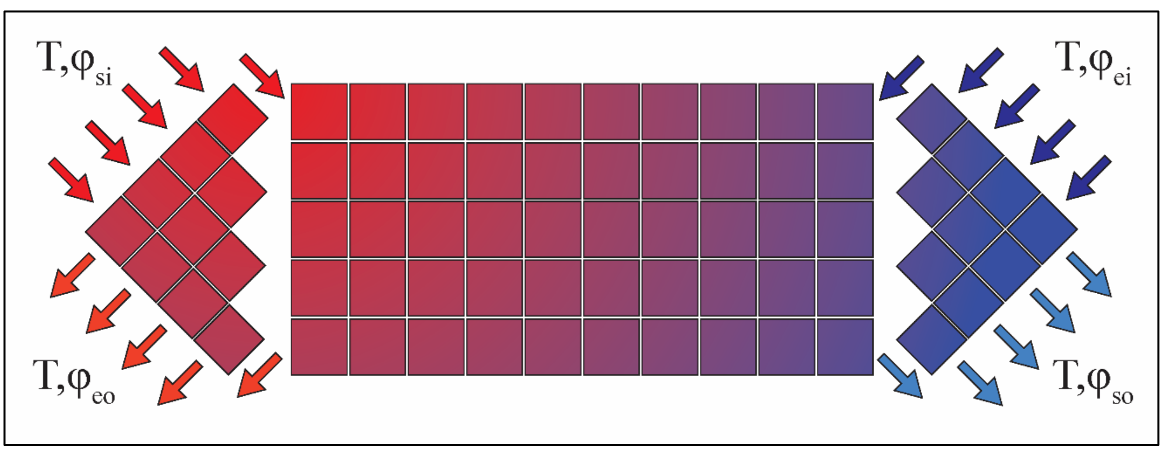

Figure 5.10: Model inlet and outlet schematic

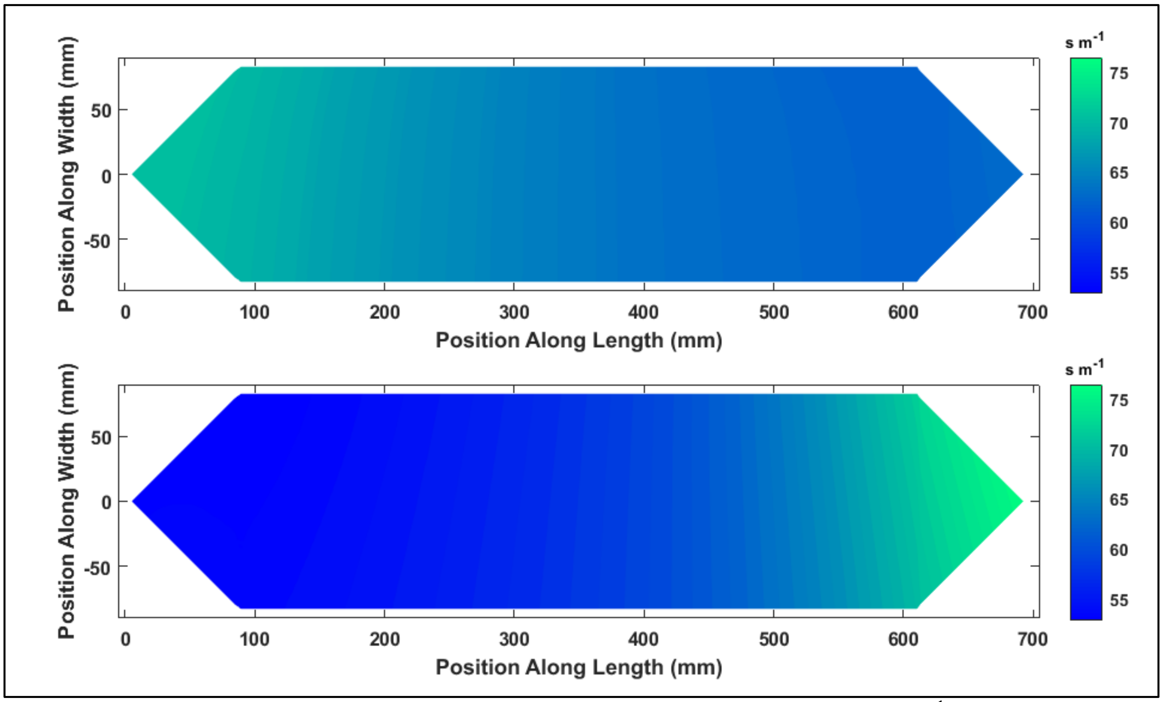

Figure 5.11: Contours of membrane mass transfer resistance $R_{m,MT}$, (s m^{-1}) using (top) AHRI rating conditions and (bottom) new inlet conditions

The heat flux is shown in Figure 5.12. Since the temperature at the inlets is the same between both sets of inlet conditions, both contour plots look very similar. Any increase in heat flux is due to the increase in heat capacity due to the larger proportion of water in the new supply air inlet condition.

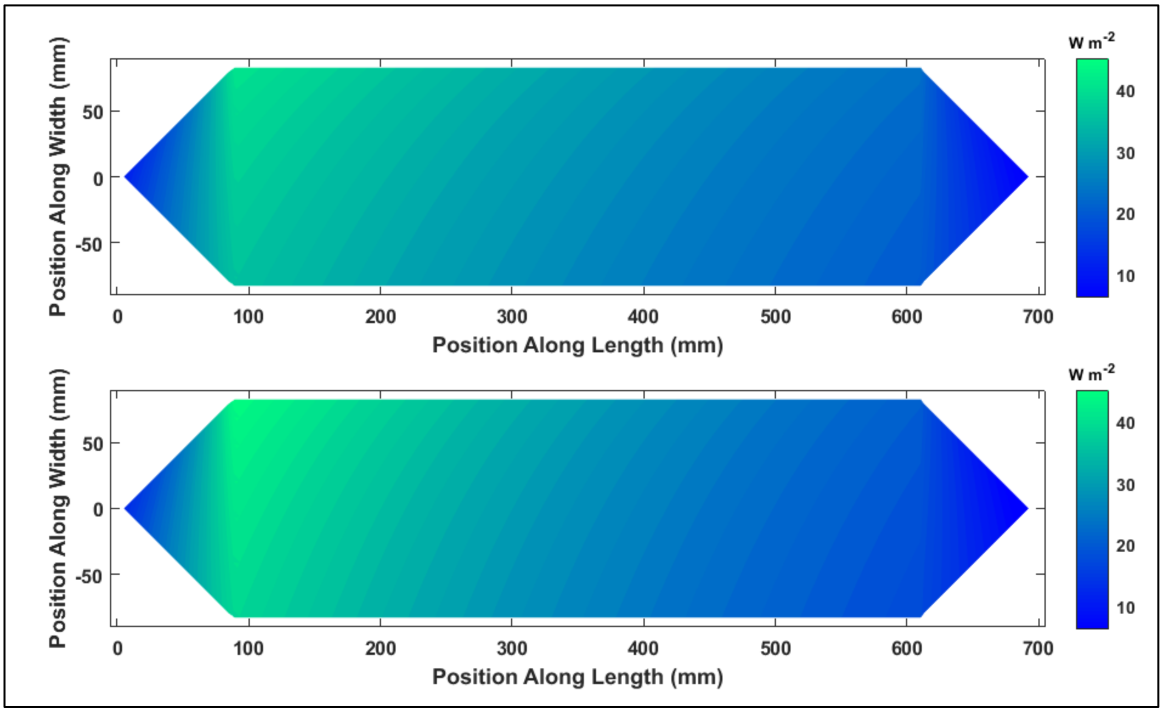

Figure 5.12: Contours of heat flux, q" (W m^{-2}) through membrane using (top) AHRI rating conditions and (bottom) new inlet conditions

The mass flux is shown in Figure 5.13. The impact of the new inlet conditions is very apparent. The maximum mass flux for the new inlet conditions is 3.72 times greater than that of the AHRI rating conditions. For both the heat and mass transfer, the most transport occurs in the entry of the left end of the body, near the supply air inlet. It is typical for the largest driving temperature difference, therefore the largest flux, in a counter flow exchanger to be near the hot side inlet. The least transport is seen at the very tip of the right header. This is intuitive since the cross flow regions are expected to be less effective than the counterflow region. Also, near the outlet, the driving temperature or concentration difference is very small.

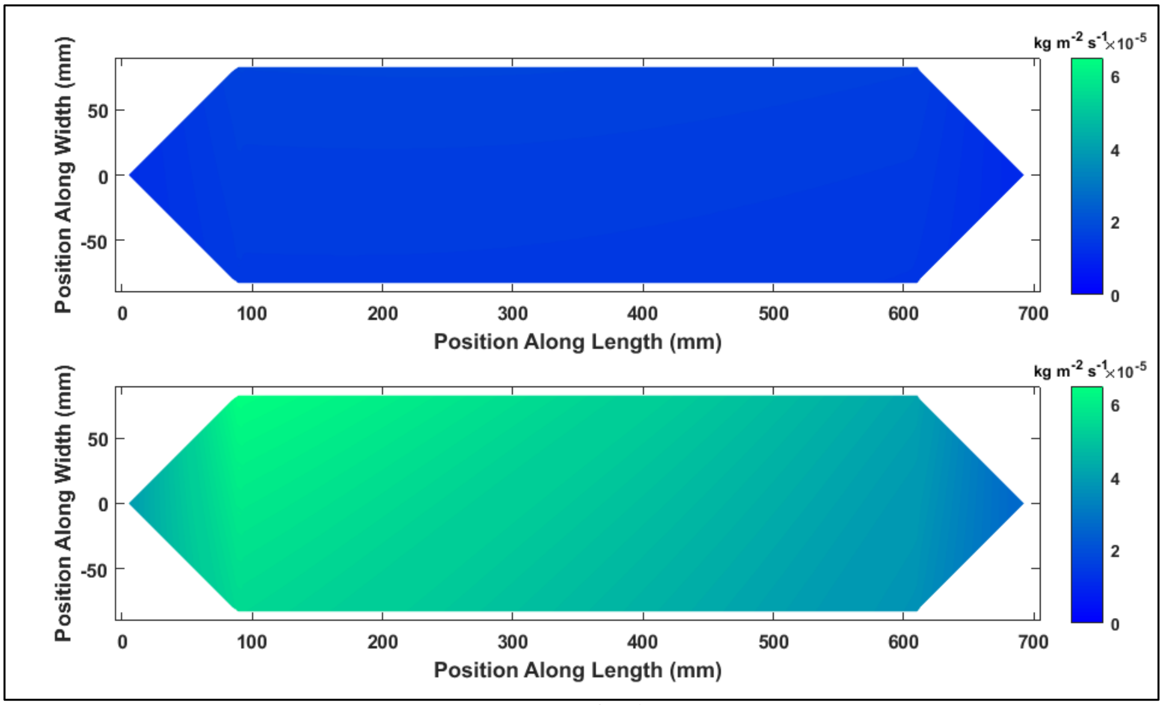

Figure 5.13: Contours of mass flux, m” (kg m^{-2} s^{-1}) through membrane using (top) AHRI rating conditions and (bottom) new inlet conditions

5.7 Summary

The ability to conduct numerous computationally cheap parametric studies to study various aspects of ERV technology was demonstrated in this chapter. Both the 1D and 2D resistance network models are very useful for preliminary ERV design assuming the membrane properties and ERV geometric parameters are well defined.

Chapter 6: Conclusions and Future Work

6.1 Conclusions

In the current study, segmented 1D and 2D resistance network models were developed to predict the sensible and latent effectiveness as well as pressure drop of an ERV. Model predictions were compared to data from the literature. A full scale ERV was designed using the model. The designed ERV was capable of satisfying the performance targets while fitting within the specified work envelope. The model was also used to design a prototype ERV fabricated at the ATAMI facility. The prototype performance was tested under various inlet conditions and air flow rates. The measured data was compared to the predicted performance values from the model. Various parametric studies were conducted to evaluate the effects of several ERV parameters on performance including the channel hydraulic diameter, the membrane diffusivity, uncertainty of inputs, and climate conditions.

The predictive capability of the resistance network models was good when compared to the literature with the majority of predicted effectiveness values within 10% of the literature values. The prototype ERV fabrication proved the manufacturing method to be viable. The pressure drop predicted by the model was generally in good agreement. The sensible effectiveness was generally underpredicted due to the assumption that the strip-fins do not provide additional heat transfer area. The latent effectiveness was greatly overpredicted by the model due to a suspected negative consequence of the specific adhesive used on the membrane mass transfer properties. Assuming 90% of the membrane area did not allow the transport of mass provided much better agreement with an AAD of 8.46%. The various parametric studies conducted showed the versatility of the model and the ability to evaluate several aspects of ERV performance. The hydraulic diameter was shown to significantly reduce contribution of the convective mass transfer resistance as it was reduced. The effectiveness was shown to be relatively insensitive to deviations in the membrane diffusion coefficient. The uncertainty in effectiveness can be most heavily attributed to flow direction and Nusselt number calculation. The climate conditions did not seem to drastically effect the sensible or latent effectiveness.

The analysis conducted to evaluate the merits of strip-fins and pin-fins showed pin-fins to have a much higher pressure drop for the same hydraulic diameter. While this is a relevant metric, an economic perspective is of greater value when considering different support structure viability. During the fabrication of the prototype, the beginning and ends of dispensed features were the most time consuming to produce. This implies a greater manufacturing cost with an increased number of support features. It was also seen through parametric studies that more channels were required as more membrane area was covered by the adhesive used to fabricate the internal support structures. This creates an additional cost to manufacturing. With these two economic considerations in mind, reducing the number of features and increasing the open area would reduce the manufacturing cost.

This model methodology has great value when considering the rapid design of an ERV. As membrane and manufacturing technology progress it is important to quickly predict the performance and ultimately the economic viability of a new ERV technology.

6.2 Recommendations and Future Work

The developed model has proven useful with the ability to quickly predict the performance of an ERV. However, there is room for improvement in the range of applicability. More internal support structures could be incorporated with a larger variety of Nusselt number and friction factor data available. Experimental or CFD data in the applicable range could be used for this. A broader evaluation of internal structures may lead to less membrane coverage and greater effectiveness while still maintaining membrane channel support. Since manufacturing cost plays a key role in the design of the internal support structure, it would be beneficial to better characterize the cost of different internal support structures before evaluating the associated performance.

The work envelope should be considered with regard to pressure drop and flow distribution. The flow routing could severely impact how well the ERV performs. Most literature assumes perfectly distributed flow to each channel as was done in this study. An investigation into this assumption would be very valuable when predicting ERV pressure drop.

Pressure drop could also benefit from a measuring technique enabling more insight into the deflection inside the ERV. Understanding the required amount of support is critical in reducing overall cost of the device. The fluid structure interaction involved in this device could be modeled numerically to give better insight into the required structural reinforcement of the device.

Bibliography

AHRI. (2013). *AHRI Standard 1060 (I-P)-2013 Standard for Performance Rating of Air-to-Air Exchangers for Energy Recovery Ventilation Equipment*. Arlington, VA, USA.

Al-Waked, R., Nasif, M. S., Morrison, G., & Behnia, M. (2013). CFD simulation of air to air enthalpy heat exchanger. *Energy Conversion and Management*, *74*, 377–385. http://doi.org/10.1016/j.enconman.2013.05.038

Al-Waked, R., Nasif, M. S., Morrison, G., & Behnia, M. (2015). CFD simulation of air to air enthalpy heat exchanger: Variable membrane moisture resistance. *Applied Thermal Engineering*, *84*, 301–309. http://doi.org/10.1016/j.applthermaleng.2015.03.067

ASHRAE. (2008). Air-to-Air Energy Recovery Equipment (pp. 25.1–25.25). Atlanta, GA, USA: ASHRAE.

ASHRAE. (2016). *ANSI/ASHRAE Standard 62.1-2016 Ventilation for Acceptable Indoor Air Quality*. Atlanta, GA.

ASHRAE. (2017). *2017 ASHRAE Handbook - Fundamentals*. ASHRAE.

Boresi, A. P. (Arthur P., & Schmidt, R. J. (Richard J. (2003). *Advanced mechanics of materials*. John Wiley & Sons.

Chilton, T. H., & Colburn, A. P. (1934). Mass transfer (absorption) coefficients prediction from data on heat transfer and fluid friction. *Industrial and Engineering Chemistry*, *26*(11), 1183–1187.

EIA. (2016). 2012 Commercial Buildings Energy Consumption Survey: Energy Usage Summary.

Gendebien, S., Bertagnolio, S., & Lemort, V. (2013). Investigation on a ventilation heat recovery exchanger: Modeling and experimental validation in dry and partially wet conditions. *Energy and Buildings*, *62*, 176–189. http://doi.org/10.1016/j.enbuild.2013.02.025

Huizing, R., Mérida, W., & Ko, F. (2014). Impregnated electrospun nanofibrous membranes for water vapour transport applications. *Journal of Membrane Science*, *461*, 146–160. http://doi.org/10.1016/j.memsci.2014.03.019

Incropera, F. P., DeWitt, D. P., Bergman, T. L., & Lavine, A. S. (2007). heat and mass transfer - Incropera 6e. *Fundamentals of Heat and Mass Transfer*. http://doi.org/10.1016/j.applthermaleng.2011.03.022

Kakaç, S. (Sadık), Shah, R. K., & Aung, W. (1987). *Handbook of single-phase convective heat transfer*. Wiley.

Kistler, K. R., & Cussler, E. L. (2002). Membrane Modules for Building Ventilation. *Chemical Engineering Research and Design*, *80*(1), 53–64. http://doi.org/10.1205/026387602753393367

Klein, S. A. (2015). Engineering Equation Solver. Madison, WI: F-Chart Software.

Koester, S., Klasen, a, Lölsberg, J., & Wessling, M. (2016). Spacer enhanced heat and mass transfer in membrane-based enthalpy exchangers. *Journal of Membrane Science*, (2). http://doi.org/http://dx.doi.org/10.1016/j.memsci.2016.06.002

Larson, M. D., Simonson, C. J., Besant, R. W., & Gibson, P. W. (2007). The elastic and moisture transfer properties of polyethylene and polypropylene membranes for use in liquid-to-air energy exchangers. *Journal of Membrane Science*, *302*(1-2), 136–149. http://doi.org/10.1016/j.memsci.2007.06.050

Lee, E.-J., Lee, J.-P., Sim, H.-M., & Kim, N.-H. (2012). Modeling and Verification of Heat and Moisture Transfer in an Enthalpy Exchanger Made of Paper Membrane. *International Journal of Air-Conditioning and Refrigeration*, *20*(03), 1250015. http://doi.org/10.1142/S2010132512500150

Mardiana-Idayu, A., & Riffat, S. B. (2012). Review on heat recovery technologies for building applications. *Renewable and Sustainable Energy Reviews*. Elsevier Ltd. http://doi.org/10.1016/j.rser.2011.09.026

Metz, S. J., Van De Ven, W. J. C., Potreck, J., Mulder, M. H. V, & Wessling, M. (2005). Transport of water vapor and inert gas mixtures through highly selective and highly permeable polymer membranes. *Journal of Membrane Science*, *251*(1-2), 29–41. http://doi.org/10.1016/j.memsci.2004.08.036

Min, J., & Su, M. (2010a). Performance analysis of a membrane-based energy recovery ventilator: Effects of membrane spacing and thickness on the ventilator performance. *Applied Thermal Engineering*, *30*(8-9), 991–997. http://doi.org/10.1016/j.applthermaleng.2010.01.010

Min, J., & Su, M. (2010b). Performance analysis of a membrane-based enthalpy exchanger: Effects of the membrane properties on the exchanger performance. *Journal of Membrane Science*, *348*(1-2), 376–382. http://doi.org/10.1016/j.memsci.2009.11.032

Min, J., & Su, M. (2011). Performance analysis of a membrane-based energy recovery ventilator: Effects of outdoor air state. *Applied Thermal Engineering*, *31*(17-18), 4036–4043. http://doi.org/10.1016/j.applthermaleng.2011.08.006

Nasif, M., Al-Waked, R., Morrison, G., & Behnia, M. (2010). Membrane heat exchanger in HVAC energy recovery systems, systems energy analysis. *Energy and Buildings*, *42*(10), 1833–1840. http://doi.org/10.1016/j.enbuild.2010.05.020

Nasif, M. S., Al-Waked, R., Behnia, M., & Morrison, G. (2012). Modeling of Air to Air Enthalpy Heat Exchanger. *Heat Transfer Engineering*, *33*(12), 377–385. http://doi.org/10.1080/01457632.2012659616

Nellis, G., & Klein, S. A. (2009). *Heat transfer*. Cambridge University Press. Retrieved from https://books.google.com/books/about/Heat_Transfer.html?id=D4FFiD6hZ94C

Niu, J. L., & Zhang, L. Z. (2001). Membrane-based Enthalpy Exchanger: Material considerations and clarification of moisture resistance. *Journal of Membrane Science*, *189*(2), 179–191. http://doi.org/10.1016/S0376-7388(00)00680-3

Shah, R. K., & London, A. L. (1978a). Chapter VII – Rectangular Ducts. *Laminar Flow Forced Convection in Ducts*, 196–222. http://doi.org/10.1016/B978-0-12-020051-1.50012-7

Shah, R. K., & London, A. L. (1978b). *Laminar Flow Forced Convection in Ducts*. *Laminar Flow Forced Convection in Ducts*. http://doi.org/10.1016/B978-0-12-020051-1.50022-X

Short, B. E., Raad, P. E., & Price, D. C. (2002). Performance of pin fin cast aluminum coldwalls, Part 2: Colburn j-factor correlations. *Journal of Thermophysics and Heat Transfer*, *16*(3), 397–403. http://doi.org/10.2514/2.6693

Short, B. E., Raad, P. E., & Price, D. C. (2002). Performance of Pin Fin Cast Alumium Coldwalls Part 2-Colburn j-Factor Correlations. *Journal of Thermophysics and Heat Transfer*, *16*(3), 397–403.

Simonson, C. J., & Besant, R. W. (1999). Energy wheel effectiveness: part I-development of dimensionless groups. *International Journal of Heat and Mass Transfer*, (42), 2161–2170. Retrieved from https://ac.els-cdn.com/S0017931098003251/1-s2.0-S0017931098003251-main.pdf?_tid=5fa67a0e-b5f0-11e7-8cb5-00000aab0f01&acdnat=1508543146_15af0a157bff2e1eabcfdb080a195eb5

Song, C. (2017). Experimental Evaluation of ERV Performance. Corvallis.

Woods, J. (2014). Membrane processes for heating, ventilation, and air conditioning. *Renewable and Sustainable Energy Reviews*, *33*, 290–304. http://doi.org/10.1016/j.rser.2014.01.092

Woods, J., & Kozubal, E. (2013). Heat transfer and pressure drop in spacer-filled channels for membrane energy recovery ventilators. *Applied Thermal Engineering*, *50*(1), 868–876. http://doi.org/10.1016/j.applthermaleng.2012.06.052

Xiang, Y., Chen, X., & Vlassak, J. J. (2005). Plane-strain Bulge Test for Thin Film. *Journal of Materials Research*, *20*(9), 2360–2370.

Yaïci, W., Ghorab, M., & Entchev, E. (2013). Numerical analysis of heat and energy recovery ventilators performance based on CFD for detailed design. *Applied Thermal Engineering*, *51*(1-2), 770–780. http://doi.org/10.1016/j.applthermaleng.2012.10.003

Yang, B., Yuan, W., Gao, F., & Guo, B. (2015). A review of membrane-based air dehumidification. *Indoor and Built Environment*, *24*(1), 11–26. http://doi.org/10.1177/1420326X13500294

Zhang, L. Z. (2005). Convective mass transport in cross-corrugated membrane exchangers. *Journal of Membrane Science*, *260*(1-2), 75–83. http://doi.org/10.1016/j.memsci.2005.03.029

Zhang, L. Z. (2006). Energy performance of independent air dehumidification systems with energy recovery measures. *Energy*, *31*, 1228–1242. http://doi.org/10.1016/j.energy.2005.05.027

Zhang, L. Z. (2008). Heat and mass transfer in plate-fin sinusoidal passages with vapor-permeable wall materials. *International Journal of Heat and Mass Transfer*, *51*(3-4), 618–629. http://doi.org/10.1016/j.ijheatmasstransfer.2007.04.050

Zhang, L. Z. (2010). Heat and mass transfer in a quasi-counter flow membrane-based total heat exchanger. *International Journal of Heat and Mass Transfer*, *53*(23-24), 5499–5508. http://doi.org/10.1016/j.ijheatmasstransfer.2010.07.009

Zhang, L. Z., & Jiang, Y. (1999). Heat and mass transfer in a membrane-based energy recovery ventilator. *Journal of Membrane Science*, *163*(1), 29–38. http://doi.org/10.1016/S0376-7388(99)00150-7

Zhang, L. Z., Liang, C. H., & Pei, L. X. (2008). Heat and moisture transfer in application scale parallel-plates enthalpy exchangers with novel membrane materials. *Journal of Membrane Science*, *325*(2), 672–682. http://doi.org/10.1016/j.memsci.2008.08.041

Zhang, L. Z., & Niu, J. L. (2002). Effectiveness Correlations for Heat and Moisture Transfer Processes in an Enthalpy Exchanger With Membrane Cores. *Journal of Heat Transfer*, *124*(5), 922. http://doi.org/10.1115/1.1469524

Zhang, L. Z., Zhu, D. S., Deng, X. H., & Hua, B. (2005). Thermodynamic modeling of a novel air dehumidification system. *Energy and Buildings*, *37*(3), 279–286. http://doi.org/10.1016/j.enbuild.2004.06.019

Zhang, Y., Jiang, Y., Zhang, L. Z., Deng, Y., & Jin, Z. (2000). Analysis of thermal performance and energy savings of membrane based heat recovery ventilator. *Energy*, *25*(6), 515–527. http://doi.org/10.1016/S0360-5442(99)00087-0

APPENDIX

Appendix A: Quasi-Counter Flow ERV Model Code

```
$UnitSystem SI K Pa J mass rad

$constant n_w# = 25 [-]; $constant n_l# = 133 [-]

"Log Mean Temperature Difference"
Function lmtd(High_1,Low_1,High_2,low_2)
{use this to calculate log mean average}
If (High_2 = low_2)  Then{use simple average to avoid divide by 0 in LN
operand}
   lmtd = ((High_1-Low_1) + (High_2-low_2))/2
Else
   If ((High_1-Low_1)/(High_2-low_2) <= 0) OR ((High_1-Low_1)/(High_2-
low_2) = 1) Then
   {use simple average to avoid LN of negative # or divide by LN(1)}
   lmtd = ((High_1-Low_1) + (High_2-low_2))/2
   Else{use Log Mean average}
   lmtd:=((High_1-Low_1)-(High_2-low_2))/ln((High_1-Low_1)/(High_2-
low_2))
   Endif
Endif
End

"Log Mean Concentration Difference"
Function lmcd(High_1,Low_1,High_2,low_2)
{use this to calculate log mean average}
If (High_2 = low_2)  Then{use simple average to avoid divide by 0 in LN
operand}
   lmcd = ((High_1-Low_1) + (High_2-low_2))/2
Else
   If ((High_1-Low_1)/(High_2-low_2) <= 0) OR ((High_1-Low_1)/(High_2-
low_2) = 1) Then
   {use simple average to avoid LN of negative # or divide by LN(1)}
   lmcd = ((High_1-Low_1) + (High_2-low_2))/2
   Else{use Log Mean average}
   lmcd:=((High_1-Low_1)-(High_2-low_2))/ln((High_1-Low_1)/(High_2-
low_2))
   Endif
Endif
End

"Locations of segment centers for contour plots"
Procedure xandyloc(i,j,HoB:a)
$common marg, w_bead, w_s_phdr, w_pbdy, w_s_pbdy, l_pbdy, l_nom,
l_s_pbdy

a = 1
if(Hob = 1) Then {header situation}

x_h1 = marg + w_bead + (-w_s_phdr/2)+(j*w_s_phdr)
y_h1 = -(marg + w_bead + (-w_s_phdr/2)+(i*w_s_phdr))

If (i < n_w#+1-j) Then
x_hdr = (x_h1*sqrt(2) - y_h1*sqrt(2))/2
```

```
y_hdr = (y_h1*sqrt(2) + x_h1*sqrt(2))/2

lookup('x_comb',i,J) = x_hdr
lookup('y_comb',i,J) = y_hdr

Else
If (i > n_w#+1-j) Then
x_hdr = (x_h1*sqrt(2) - y_h1*sqrt(2))/2 + l_pbdy - (sqrt(2)*w_s_phdr/2)
y_hdr = (y_h1*sqrt(2) + x_h1*sqrt(2))/2
rhdr_col = j+n_l#-1
lookup('x_comb',i,RHDR_COL) = x_hdr
lookup('y_comb',i,RHDR_COL) = y_hdr
Else
a = 2

Endif
Endif

Else {body situation}

col = j+n_w#-i
lookup('x_comb',I,COL) = (l_nom/2)-(l_pbdy/2)-(l_s_pbdy/2)+l_s_pbdy*j

ri_w = n_w#+1 - i
ycol = j + i -1
lookup('y_comb',ri_w,YCOL) = (-w_s_pbdy/2) + (i*w_s_pbdy) - (w_pbdy/2)

Endif

End

"Save a value for contour plots"
Procedure lkuptbl(i,j,Val,tn$,HoB:a)

a = 1
if(Hob = 1) Then {header situation}

If (i < n_w#+1-j) Then

lookup(tn$,i,J) = Val

Else
If (i > n_w#+1-j) Then

rhdr_col = j+n_l#-1

lookup(tn$,i,RHDR_COL) = Val

Else
a = 2

Endif
Endif

Else {body situation}
```

```
col = j+n_w#-i
lookup(tn$,i,COL) = Val

Endif

End

"Find the pressure drop across a header and body segment"
Procedure dp(i:DELTAP_fhdr,DELTAP_ehdr,DELTAP_fbdy,DELTAP_ebdy)
$common
w_s_chdr,w_d_hdr,w_d_bdy,Re_fhdr,Re_ehdr,Pr_f,Pr_e,D_h_hdr,h_ch,w_chdr,
l_s_cbdy,Re_fbdy,Re_ebdy,D_h_bdy,rho_f,rho_e,u_hdr_f,u_hdr_e,u_bdy_f,u_
bdy_e

L_hdr = i*w_s_chdr - (w_s_chdr/2)
Call ductflow_n_local(Re_fhdr, Pr_f, L_hdr/D_h_hdr, h_ch/w_d_hdr, 0:
Nu#_T_fhdr, Nu#_H_fhdr, f_fhdr)
Call ductflow_n_local(Re_ehdr, Pr_e, L_hdr/D_h_hdr, h_ch/w_d_hdr, 0:
Nu#_T_ehdr, Nu#_H_ehdr, f_ehdr)

DELTAP_fhdr = f_fhdr*rho_f*(u_hdr_f^2)*w_s_chdr/(2*D_h_hdr)
DELTAP_ehdr = f_ehdr*rho_e*(u_hdr_e^2)*w_s_chdr/(2*D_h_hdr)

L_bdy = i*l_s_cbdy - (l_s_cbdy/2)
Call ductflow_n_local(Re_fbdy, Pr_f, L_bdy/D_h_bdy, h_ch/w_d_bdy, 0:
Nu#_T_fbdy, Nu#_H_fbdy, f_fbdy)
Call ductflow_n_local(Re_ebdy, Pr_e, L_bdy/D_h_bdy, h_ch/w_d_bdy, 0:
Nu#_T_ebdy, Nu#_H_ebdy, f_ebdy)

DELTAP_fbdy = f_fbdy*rho_f*(u_bdy_f^2)*l_s_cbdy/(2*D_h_bdy)
DELTAP_ebdy = f_ebdy*rho_e*(u_bdy_e^2)*l_s_cbdy/(2*D_h_bdy)

End

"Find the inputs for sensible and latent effectiveness"
Procedure effectiveness(t_fo,omega_fo:C_s_fo,C_min_s,C_l_fo,C_min_l)
$common m_dot_fa,m_dot_ea,t_fin,t_ein,omega_fin,omega_ein

c_p_fo = cp(Air,T = t_fo)
C_s_fo = m_dot_fa*c_p_fo
c_p_ei = cp(Air,T = t_ein)
C_s_ei = m_dot_ea*c_p_ei

h_fg_fo = enthalpy_vaporization(Water,T = t_fo)
C_l_fo = m_dot_fa*h_fg_fo
h_fg_ei = enthalpy_vaporization(Water,T = t_ein)
C_l_ei = m_dot_ea*h_fg_ei

IF(C_s_fo < C_s_ei) Then C_min_s = C_s_fo Else C_min_s = C_s_ei
IF(C_l_fo < C_l_ei) Then C_min_l = C_l_fo Else C_min_l = C_l_ei

End
```

```
"Find the supply and exhaust enthalpies and absolute humidities of a
header segment using conservation of mass and energy"
Subprogram hdr(i,j,lfi,lei,
i_fi,i_ei,omega_fi,omega_ei:i_fo,i_eo,omega_fo,omega_eo)
$arrays off
$common m_dot_fa, m_dot_ea, D_h_hdr, a_m_hdr, a_m_hdrmt, a_m_hdrht,
k_m, d_m, del, t_m_h, t_m_l, cl[0..4], ch[0..4], c_da, Nusselt_hdr,
p_bar_f, p_bar_e

Call xandyloc(i,j,1:a1)

t_fin = temperature(AirH2O, h=i_fi, w=omega_fi, P=p_bar_f)
t_fo = temperature(AirH2O, h=i_fo, w=omega_fo, P=p_bar_f)
t_ein = temperature(AirH2O, h=i_ei, w=omega_ei, P=p_bar_e)
t_eo = temperature(AirH2O, h=i_eo, w=omega_eo, P=p_bar_e)
t_bar_f = average(t_fin,t_fo)
t_bar_e = average(t_ein,t_eo)
omega_bar_f = average(omega_fi,omega_fo)
omega_bar_e = average(omega_ei,omega_eo)

c_fi = relhum(AirH2O, T = t_fin, w = omega_fi, P =
p_bar_f)*p_sat(Water,T = t_fin)/(R#*t_fin)
c_fo = relhum(AirH2O, T = t_fo, w = omega_fo, P =
p_bar_f)*p_sat(Water,T = t_fo)/(R#*t_fo)
c_ei = relhum(AirH2O, T = t_ein, w = omega_ei, P =
p_bar_e)*p_sat(Water,T = t_ein)/(R#*t_ein)
c_eo = relhum(AirH2O, T = t_eo, w = omega_eo, P =
p_bar_e)*p_sat(Water,T = t_eo)/(R#*t_eo)
c_bar_f = average(c_fi,c_fo)

"Assume cross flow in headers is negligible"
f_ht = 1
f_mt = 1

k_af = conductivity(AirH2O,T=t_bar_f,w=omega_bar_f,P=p_bar_f)
k_ae = conductivity(AirH2O,T=t_bar_e,w=omega_bar_e,P=p_bar_e)
d_af = c_da*(t_bar_f^2.072); d_ae = c_da*(t_bar_e^2.072)
rho_f = density(AirH2O,T = t_bar_f, w = omega_bar_f, P = p_bar_f)
rho_e = density(AirH2O,T = t_bar_e, w = omega_bar_e, P = p_bar_e)
alpha_f = thermaldiffusivity(AirH2O, T = t_bar_f, w = omega_bar_f, P =
p_bar_f)
alpha_e = thermaldiffusivity(AirH2O, T = t_bar_e, w = omega_bar_e, P =
p_bar_e)
c_p_f = cp(AirH2O, T = t_bar_f, w = omega_bar_f, P = p_bar_f)
c_p_e = cp(AirH2O, T = t_bar_e, w = omega_bar_e, P = p_bar_e)

h_f = Nusselt_hdr*k_af/D_h_hdr; h_e = Nusselt_hdr*k_ae/D_h_hdr
t_w_f = t_bar_f - (q_dot/(a_m_hdrht*h_f))
t_w_e = t_bar_e + (q_dot/(a_m_hdrht*h_f))
t_bar_w = average(t_w_f,t_w_e)
u = ((1/h_f) + (del/k_m) + (1/h_e))^(-1)
q_dot = f_ht*u*a_m_hdrht*lmtd(t_fin,t_eo,t_fo,t_ein)
q_dprime = q_dot/a_m_hdr

Call lkuptbl(i,j,q_dprime,'q_comb',1:a2)
```

```
beta_f = (h_f/(rho_f*c_p_f))*(d_af/alpha_f)^(2/3); beta_e =
(h_e/(rho_e*c_p_e))*(d_ae/alpha_e)^(2/3)
phi_w_f = (c_bar_f -
(m_dot_v/(molarmass('water')*beta_f*a_m_hdrmt)))*t_w_f*R#/p_sat(Water,T
= t_w_f)
r_m_mt = ((cl[4]*(phi_w_f^4) + cl[3]*(phi_w_f^3) + cl[2]*(phi_w_f^2) +
cl[1]*phi_w_f + cl[0])*(t_m_h - t_w_f) + (ch[4]*(phi_w_f^4) +
ch[3]*(phi_w_f^3) + ch[2]*(phi_w_f^2) + ch[1]*phi_w_f + ch[0])*(t_w_f -
t_m_l))/(t_m_h - t_m_l)

Call lkuptbl(i,j,r_m_mt,'r_m_mt',1:a3)

k = ((1/beta_f) + r_m_mt + (1/beta_e))^(-1)
m_dot_v = f_mt*molarmass('water')*k*a_m_hdrmt*lmcd(c_fi,c_eo,c_fo,c_ei)
m_dprime = m_dot_v/a_m_hdr

Call lkuptbl(i,j,m_dprime,'m_comb',1:a4)

i_v = enthalpy(Water, T = t_bar_w, x = 1)

   "Mass Balance"
   m_dot_v = m_dot_fa*(omega_fi - omega_fo)
   m_dot_v = m_dot_ea*(omega_eo - omega_ei)

   "Energy Balance"
   0 = m_dot_fa*(i_fi - i_fo) - m_dot_v*i_v - q_dot
   0 = m_dot_ea*(i_ei - i_eo) + m_dot_v*i_v + q_dot

End

"Find the supply and exhaust enthalpies and absolute humidities of a
row of body segments along the body length using conservation of mass
and energy"
Subprogram
body(i_w,i_fin,i_ein,omega_fin,omega_ein{,Nu#_f[1..n_l#],Nu#_e[1..n_l#]
}:i_fout,i_eout,omega_fout,omega_eout,r_bar_m_mt)
$common m_dot_fa, m_dot_ea,c_da, D_h_bdy, del, k_m, d_m, t_m_h, t_m_l,
cl[0..4], ch[0..4], c_da, a_m_bdy, a_m_bdymt, a_m_bdyht, Nusselt_bdy,
p_fin, p_ein, p_bar_f, p_bar_e

$arrays off
i_fo[0] = i_fin
omega_fo[0] = omega_fin
t_fo[0] = temperature(AirH2O, h=i_fo[0], w=omega_fo[0], P=p_fin)
c_fo[0] = relhum(AirH2O, T = t_fo[0], w = omega_fo[0], P =
p_fin)*p_sat(Water,T = t_fo[0])/(R#*t_fo[0])

i_eo[n_l#+1] = i_ein
omega_eo[n_l#+1] = omega_ein
t_eo[n_l#+1] = temperature(AirH2O, h=i_eo[n_l#+1], w=omega_eo[n_l#+1],
P=p_ein)
c_eo[n_l#+1] =
relhum(AirH2O,T=t_eo[n_l#+1],w=omega_eo[n_l#+1],P=p_ein)*p_sat(Water,T
= t_eo[n_l#+1])/(R#*t_eo[n_l#+1])
```

```
i_fout = i_fo[n_l#]
omega_fout = omega_fo[n_l#]
i_eout = i_eo[1]
omega_eout = omega_eo[1]

r_bar_m_mt = average(r_m_mt[1..n_l#])

Duplicate i = 1,n_l#

Call xandyloc(i_w,i,0:a1[i])

t_fo[i] = temperature(AirH2O, h=i_fo[i], w=omega_fo[i], P=p_bar_f)
t_eo[i] = temperature(AirH2O, h=i_eo[i], w=omega_eo[i], P=p_bar_e)

c_fo[i] = relhum(AirH2O, T = t_fo[i], w = omega_fo[i], P =
p_bar_f)*p_sat(Water,T = t_fo[i])/(R#*t_fo[i])
c_eo[i] = relhum(AirH2O, T = t_eo[i], w = omega_eo[i], P =
p_bar_e)*p_sat(Water,T = t_eo[i])/(R#*t_eo[i])

k_af[i] = conductivity(AirH2O,T=t_fo[i-1],w=omega_fo[i-1],P=p_bar_f)
k_ae[i] = conductivity(AirH2O,T=t_eo[i+1],w=omega_eo[i+1],P=p_bar_e)
d_af[i] = c_da*(t_fo[i-1]^2.072); d_ae[i] = c_da*(t_eo[i+1]^2.072)
rho_f[i] = density(AirH2O,T = t_fo[i-1], w = omega_fo[i-1], P =
p_bar_f)
rho_e[i] = density(AirH2O,T = t_eo[i+1], w = omega_eo[i+1], P =
p_bar_e)
alpha_f[i] = thermaldiffusivity(AirH2O, T = t_fo[i-1], w = omega_fo[i-
1], P = p_bar_f)
alpha_e[i] = thermaldiffusivity(AirH2O, T = t_eo[i+1], w =
omega_eo[i+1], P = p_bar_e)
c_p_f[i] = cp(AirH2O, T = t_fo[i-1], w = omega_fo[i-1], P = p_bar_f)
c_p_e[i] = cp(AirH2O, T = t_eo[i+1], w = omega_eo[i+1], P = p_bar_e)

h_f[i] = Nusselt_bdy*k_af[i]/D_h_bdy; h_e[i] =
Nusselt_bdy*k_ae[i]/D_h_bdy
t_w_f[i] = t_fo[i-1] - (q_dot[i]/(a_m_bdyht*h_f[i]))
u[i] = ((1/h_f[i]) + (del/k_m) + (1/h_e[i]))^(-1)
q_dot[i] = u[i]*a_m_bdyht*lmtd(t_fo[i-1],t_eo[i],t_fo[i],t_eo[i+1])
q_dprime[i] = q_dot[i]/a_m_bdy

Call lkuptbl(i_w,i,q_dprime[i],'q_comb',0:a2[i])

beta_f[i] = (h_f[i]/(rho_f[i]*c_p_f[i]))*(d_af[i]/alpha_f[i])^(2/3)
beta_e[i] = (h_e[i]/(rho_e[i]*c_p_e[i]))*(d_ae[i]/alpha_e[i])^(2/3)
phi_w_f[i] = (c_fo[i-1]-
(m_dot_v[i]/(molarmass('water')*beta_f[i]*a_m_bdymt)))*t_w_f[i]*R#/p_sa
t(Water,T = t_w_f[i])
r_m_mt[i] = ((cl[4]*(phi_w_f[i]^4) + cl[3]*(phi_w_f[i]^3) +
cl[2]*(phi_w_f[i]^2) + cl[1]*phi_w_f[i] + cl[0])*(t_m_h - t_w_f[i]) +
(ch[4]*(phi_w_f[i]^4) + ch[3]*(phi_w_f[i]^3) + ch[2]*(phi_w_f[i]^2) +
ch[1]*phi_w_f[i] + ch[0])*(t_w_f[i] - t_m_l))/(t_m_h - t_m_l)

Call lkuptbl(i_w,i,r_m_mt[i],'r_m_mt',0:a3[i])
```

```
k[i] = ((1/beta_f[i]) + r_m_mt[i] + (1/beta_e[i]))^(-1)
m_dot_v[i] = molarmass('water')*k[i]*a_m_bdymt*lmcd(c_fo[i-
1],c_eo[i],c_fo[i],c_eo[i+1])
m_dprime[i] = m_dot_v[i]/a_m_bdy

Call lkuptbl(i_w,i,m_dprime[i],'m_comb',0:a4[i])

i_v[i] = enthalpy(Water, T = t_w_f[i], x = 1)

"Mass Balance"
m_dot_v[i] = m_dot_fa*(omega_fo[i-1] - omega_fo[i])
m_dot_v[i] = m_dot_ea*(omega_eo[i] - omega_eo[i+1])

"Energy Balance"
0 = m_dot_fa*(i_fo[i-1] - i_fo[i]) - m_dot_v[i]*i_v[i] - q_dot[i]
0 = m_dot_ea*(i_eo[i+1] - i_eo[i]) + m_dot_v[i]*i_v[i] + q_dot[i]

End
End

"Gryphon Membrane and Air Properties"
del = 25e-6 [m]; k_m = 0.0765 [W/m-K]; d_m = 4.3e-7 [m^2/s]; d_a =
2.82e-5 [m^2/s]
t_m_h = 308.15 [K]; t_m_l = 298.15 [K]; c_da = 1.87e-10 [m^2/s-K^2.072]

cl[4] = -880.65 [s/m]; cl[3] =  2075.9 [s/m]; cl[2] = -1714.1 [s/m];
cl[1] =  526.6  [s/m]; cl[0] = 27.109 [s/m]
ch[4] =  80.631 [s/m]; ch[3] = -94.507 [s/m]; ch[2] = -5.8746 [s/m];
ch[1] = -24.743 [s/m]; ch[0] = 89.52  [s/m]

"ERV dimensions and parameters"
n_ch = 352 [-]
n_d_bdy = 24 [-]
n_d_hdr = 23
h_ch = 1.185*convert(mm,m)
n_ch_nom = 2*n_ch
w_nom = 175*convert(mm,m)
marg = 0 [m]
r_bw2h = 1 [-]
w_bead = r_bw2h*h_ch
l_nom = 0.7 [m]
h_nom = 2*n_ch*(h_ch+del)+del
w_hdr = w_nom/sqrt(2)

"Deflection modeling at header outlet and body end"
c_1 = 0.8+0.062*nu_m
c_2 = 3.393 [-]
E_m1 = 650e6 [Pa]
E_m2 = 1222e6 [Pa]
E_m = average(E_m1,E_m2)
nu_m = 0.42
sigma_0 = 0 [Pa]
a_d_hdr = w_d_hdr/2
DELTAP_e = (c_1*E_m*del*(DELTAh_ch_hdr^3)/((1-nu_m)*(a_d_hdr^4))) +
(c_2*sigma_0*del*DELTAh_ch_hdr/(a_d_hdr^2))
```

```
h_%def_hdr = (2*DELTAh_ch_hdr/h_ch)*convert(-,%)

a_d_bdy = w_d_bdy/2
DELTAP_e - sum(DELTAP_ebdy[1..n_l#]) =
(c_1*E_m*del*(DELTAh_ch_bdy^3)/((1-nu_m)*(a_d_bdy^4))) +
(c_2*sigma_0*del*DELTAh_ch_bdy/(a_d_bdy^2))
h_%def_bdy = (2*DELTAh_ch_bdy/h_ch)*convert(-,%)

"Volume flow rate of air"
V_dot_cfm = 300 [cfm]

"Inlet Conditions"
t_finF = 95 [F]; t_einF = 75 [F]
t_finFb = 78 [F];t_einFb = 63 [F]

"Ratio of unaffected open area for heat and mass transfer"
r_mta = 1 [-]
r_hta = 1 [-]
"Plot Dimensions"
"Body"
w_pbdy = w_nom - 2*marg - 2*w_bead
w_s_pbdy = w_pbdy/n_w#
l_pbdy = l_nom - w_nom
l_s_pbdy = l_pbdy/n_l#

"Header"
"Nominal"
w_phdr = w_pbdy/sqrt(2)
w_s_phdr = w_phdr/n_w#
"Corrected"
w_s_chdr = (w_hdr-2*marg-(n_d_hdr+1)*w_bead)/n_w#
w_chdr = w_s_chdr*(n_w# - 1)

"Body"
w_cbdy = w_nom-2*marg-(n_d_bdy +1)*w_bead
w_s_cbdy = w_cbdy/n_w#
l_cbdy = (l_nom-w_nom)+((w_s_chdr^2)/w_s_cbdy)
l_s_cbdy = l_cbdy/n_l#

"Nusselt number"
w_d_hdr = (w_hdr-((n_d_hdr+1)*w_bead))/n_d_hdr
w_d_bdy = (w_nom-((n_d_bdy+1)*w_bead))/n_d_bdy
Nusselt_hdr = interpolate('Nu S&L','Nu#_T','Aspect',Aspect =
h_ch/w_d_hdr)
Nusselt_bdy = interpolate('Nu S&L','Nu#_T','Aspect',Aspect =
h_ch/w_d_bdy)

"Membrane area calculations"
a_m_hdr = 2*(w_s_chdr^2)
a_m_hdrmt = a_m_hdr*r_mta
a_m_hdrht = a_m_hdr*r_hta
a_m_bdy = 2*w_s_cbdy*l_s_cbdy
a_m_bdymt = a_m_bdy*r_mta
a_m_bdyht = a_m_bdy*r_hta
a_ch_chdr = h_ch*w_d_hdr
```

```
a_ch_cbdy = h_ch*w_d_bdy

"Flow rates in channels, ducts, and segments"
V_dot_t = V_dot_cfm*convert(cfm,m^3/s)
V_dot_ch = V_dot_t/n_ch
V_dot_s = V_dot_ch/n_w#
V_dot_dbdy = V_dot_ch/n_d_bdy
V_dot_dhdr = V_dot_ch/n_d_hdr

"Inlet conditions, converted units, enthalpy"
t_fin = converttemp(F,K,t_finF); t_ein = converttemp(F,K,t_einF)
t_finb = converttemp(F,K,t_finFb); t_einb = converttemp(F,K,t_einFb)
omega_fin = humrat(AirH2O, T=t_fin, B=t_finb, P=p_fin)
omega_ein = humrat(AirH2O, T=t_ein, B=t_einb, P=p_ein)
i_fin = enthalpy(AirH2O, T = t_fin, b = t_finb, P = p_fin)
i_ein = enthalpy(AirH2O, T = t_ein, b = t_einb, P = p_ein)

"Average Property Values"
t_bar = average(t_fin,t_ein)
omega_bar = average(omega_fin,omega_ein)
p_bar_f = average(p_fin,Po#)
p_bar_e = average(p_ein,Po#)
p_bar = average(p_bar_f,p_bar_e)

rho_bar = density(AirH2O, T = t_bar, w = omega_bar, P = p_bar)
rho_f = density(AirH2O, T = t_fin, w = omega_fin, P = p_bar_f)
rho_e = density(AirH2O, T = t_ein, w = omega_ein, P = p_bar_e)

Pr_f = prandtl(AirH2O, T = t_bar, w = omega_bar, P = p_bar_f)
Pr_e = prandtl(AirH2O, T = t_bar, w = omega_bar, P = p_bar_e)

mu_f = viscosity(AirH2O, T=t_bar, w=omega_bar, P=p_bar_f)
mu_e = viscosity(AirH2O, T=t_bar, w=omega_bar, P=p_bar_e)
m_dot_fa = V_dot_s*rho_f/(omega_fin + 1); m_dot_ea =
V_dot_s*rho_e/(omega_ein + 1)

"Header Pressure Drop Values"
m_dot_fa_dhdr = V_dot_dhdr*rho_f/(omega_fin + 1);m_dot_ea_dhdr =
V_dot_dhdr*rho_e/(omega_ein + 1)
D_h_hdr = 4*a_ch_chdr/(2*h_ch + 2*w_d_hdr)
u_hdr_f = m_dot_fa_dhdr*(omega_fin + 1)/(rho_f*h_ch*w_d_hdr)
u_hdr_e = m_dot_ea_dhdr*(omega_ein + 1)/(rho_e*h_ch*w_d_hdr)
Re_fhdr = rho_f*u_hdr_f*D_h_hdr/mu_f; Re_ehdr =
rho_e*u_hdr_e*D_h_hdr/mu_e

"Body Pressure Drop Values"
m_dot_fa_dbdy = V_dot_dbdy*rho_f/(omega_fin + 1); m_dot_ea_dbdy =
V_dot_dbdy*rho_e/(omega_ein + 1)
D_h_bdy = 4*a_ch_cbdy/(2*h_ch + 2*w_d_bdy)
u_bdy_f = m_dot_fa_dbdy*(omega_fin + 1)/(rho_f*h_ch*w_d_bdy)
u_bdy_e = m_dot_ea_dbdy*(omega_ein + 1)/(rho_e*h_ch*w_d_bdy)
Re_fbdy = rho_f*u_bdy_f*D_h_bdy/mu_f; Re_ebdy =
rho_e*u_bdy_e*D_h_bdy/mu_e

"Pressure drop"
```

```
Duplicate i = 1,n_l#
Call dp(i:DELTAP_fhdr[i],DELTAP_ehdr[i],DELTAP_fbdy[i],DELTAP_ebdy[i])
End

"Inlets"
Duplicate i = 1,n_w#-1
i_f[0,i] = i_fin
omega_f[0,i] = omega_fin
End

Duplicate i = 2,n_w#
i_e[i,n_w#+1] = i_ein
omega_e[i,n_w#+1] = omega_ein
End

"Left"
Duplicate i = 1,n_w#-1
  Duplicate j = 1,n_w#-i
  call hdr(i,j,i,n_w#+1-i-j,i_f[i-1,j],i_e[i,j+1],omega_f[i-
1,j],omega_e[i,j+1]:i_f[i,j],i_e[i,j],omega_f[i,j],omega_e[i,j])
  End
End

"Right"
Duplicate i = 2,n_w#
b1[i] = n_w#-i+2
  Duplicate j = b1[i],n_w#
  call hdr(i,j,i+j-n_w#-1,n_w#+1-j,i_f[i-1,j],i_e[i,j+1],omega_f[i-
1,j],omega_e[i,j+1]:i_f[i,j],i_e[i,j],omega_f[i,j],omega_e[i,j])
  End
End

"Body"
Duplicate k = 1,n_w#-1
i_f[k,n_w#-k] = i_fin_bdy[k+1]
omega_f[k,n_w#-k] = omega_fin_bdy[k+1]
End
i_fin_bdy[1] = i_fin
omega_fin_bdy[1] = omega_fin

Duplicate k = 2,n_w#
i_e[k,n_w#+2-k] = i_ein_bdy[k]
omega_e[k,n_w#+2-k] = omega_ein_bdy[k]
End
i_ein_bdy[1] = i_ein
omega_ein_bdy[1] = omega_ein

Duplicate k = 1,n_w#
Call body(k,i_fin_bdy[k], i_ein_bdy[k], omega_fin_bdy[k],
omega_ein_bdy[k]: i_fout_bdy[k], i_eout_bdy[k], omega_fout_bdy[k],
omega_eout_bdy[k],r_bdy_m_mt[k])
End

Duplicate k = 1,n_w#-1
i_fout_bdy[k] = i_f[k,n_w#+1-k]
```

```
omega_fout_bdy[k] = omega_f[k,n_w#+1-k]

i_eout_bdy[k] = i_e[k,n_w#+1-k]
omega_eout_bdy[k] = omega_e[k,n_w#+1-k]
End

"Outlets"
i_fout_bdy[n_w#] = i_fout[n_w#]
omega_fout_bdy[n_w#] = omega_fout[n_w#]

i_eout_bdy[n_w#] = i_eout[n_w#]
omega_eout_bdy[n_w#] = omega_eout[n_w#]

Duplicate k = 2,n_w#
i_f[n_w#,k] = i_fout[k-1]
omega_f[n_w#,k] = omega_fout[k-1]
End

Duplicate k = 1,n_w#-1
i_e[k,1] = i_eout[k]
omega_e[k,1] = omega_eout[k]
End

"Average mass transfer resistance"
r_bar_bdy_m_mt = average(r_bdy_m_mt[1..n_w#])
Duplicate i = 1,n_w#
r_bar_hdrc_m_mt[i] = avglookup('r_m_mt',i)
End
r_bar_hdr_m_mt = average(r_bar_hdrc_m_mt[1..n_w#])
r_bar_m_mt = ((w_hdr^2)/a_m_layer_nom)*r_bar_hdr_m_mt +
((l_pbdy*w_nom)/a_m_layer_nom)*r_bar_bdy_m_mt

"Mass flow rate of dry air through channel"
m_dot_fa_ch = V_dot_ch*rho_f/(omega_fin + 1)
m_dot_ea_ch = V_dot_ch*rho_e/(omega_ein + 1)

"Average outlet enthalpy, absolute humidity values, and temperatures"
i_bar_fout = average(i_fout[1..n_w#])
i_bar_eout = average(i_eout[1..n_w#])
omega_bar_fout = average(omega_fout[1..n_w#])
omega_bar_eout = average(omega_eout[1..n_w#])
t_bar_fout = temperature(AirH2O,h = i_bar_fout, w = omega_bar_fout, P =
Po#)
t_bar_eout = temperature(AirH2O,h = i_bar_eout, w = omega_bar_eout, P =
Po#)

"Sensible and latent effectiveness"
Call
effectiveness(t_bar_fout,omega_bar_fout:C_s_fo,C_min_s,C_l_fo,C_min_l)
epsilon_S = (C_s_fo*(t_fin-t_bar_fout)/(C_min_s*(t_fin-
t_ein)))*convert(-,%)
epsilon_L = (C_l_fo*(omega_fin-omega_bar_fout)/(C_min_l*(omega_fin-
omega_ein)))*convert(-,%)

"Pressure drop across ERV for supply and exhaust"
```

```
DELTAP_f = sum(DELTAP_fhdr[1..n_w#]) + sum(DELTAP_fbdy[1..n_l#])
DELTAP_e = sum(DELTAP_ehdr[1..n_w#]) + sum(DELTAP_ebdy[1..n_l#])
p_fin = DELTAP_f + Po#
p_ein = DELTAP_e + Po#

"Supply and exhaust outlet mass flow rates"
m_dot_fo = m_dot_fa*(omega_bar_fout + 1)
m_dot_eo = m_dot_ea*(omega_bar_eout + 1)

"Supply and exhaust inlet mass flow rates"
m_dot_fin = rho_f*V_dot_s
m_dot_ein = rho_e*V_dot_s

"Open area ratio"
a_m_layer_nom = (w_hdr^2) + l_pbdy*w_nom
a_m_layer = a_m_layer_nom - w_bead*l_pbdy*(n_d_bdy+1) -
w_bead*w_hdr*(n_d_hdr+1)
R_mAU = (a_m_layer/a_m_layer_nom)*convert(-,%)
```